UNIVERSITY OF SOUTHAMPTON
FACULTY OF ENGINEERING AND PHYSICAL SCIENCES
Optoelectronics Research Centre

Tantalum Pentoxide Integrated Photonic Devices

by

Amy Sen Kay Tong

Thesis for the degree of Doctor of Philosophy

March 2019

UNIVERITY OF SOUTHAMPTON

ABSTRACT

FACULTY OF ENGINEERING AND PHYSICAL SCIENCES

Optoelectronics Research Centre

Thesis for the degree of Doctor of Philosophy

TANTALUM PENTOXIDE INTEGRATED PHOTONIC DEVICES

by Amy Sen Kay Tong

This thesis investigates tantalum pentoxide (Ta_2O_5) as a material for realising integrated photonic devices on a silicon platform, as a basis for realising photonics integrated circuits with multiple functionalities on a single monolithic chip. In particular, achieving gain and lasing, and electro-optic functionalities were studied. To further investigate the integration of these functionalities onto a silicon platform, a grating-assisted coupler was explored.

Ta_2O_5 thin films were deposited on oxidised silicon wafer using RF sputtering and waveguides were realised using lithography and ion beam milling. An optimisation of the etching process to reduce waveguide sidewall roughness was performed.

Thulium-doped Ta_2O_5 was investigated to provide gain and lasing at around 2 μm by pumping at around 790 nm. With a thulium-doping concentration of $9x10^{20}$ ions/cm^3, the highest peak photoluminescence power and lifetime was achieved with sample annealed at 650 °C for 12 hours. The excited-state lifetime of this sample was 477 ± 40 μs. Emission centred around 1.85 μm and a high emission cross-section of $2.99x10^{-20}$ cm^2 was attained. The absorption cross-section were $8.05x10^{-21}$ cm^2 at 792 nm and $1.09x10^{-20}$ cm^2 at a wavelength of 1756 nm.

Second-order nonlinearity was achieved in Ta_2O_5 by thermal poling, 0.46 and 0.34 pm/V was achieved with sodium-doped and undoped Ta_2O_5 respectively. The effect of sodium-doping and annealing on the induced second-order nonlinearity was studied.

A grating-assisted coupler was designed and fabricated to couple between 750 by 750 nm Ta_2O_5 and a 400 by 250 nm Si channel waveguides. Simulations show that a grating period of 2.361 μm was required for coupling to occur.

The results show that tantalum pentoxide is a promising medium for realising integrated lasers and amplifiers, electro-optic applications on a silicon platform.

Table of Contents

Table of Contents v
List of Figures ix
List of Tables xi
Nomenclature xiii
Declaration of Authorship xv
Acknowledgement xvii
Chapter 1 Introduction 1
1.1 Thesis Structure 2
1.1.1 List of Publications 3
Chapter 2 Tantalum Pentoxide Waveguide Design and Fabrication 5
2.1 Introduction 5
2.2 Fabrication 6
2.2.1 Deposition 6
2.2.2 Annealing 7
2.2.3 Lithography 7
2.2.4 Etching 8
2.2.5 Resist Removal 10
2.2.6 Cladding 10
2.2.7 Lapping and Polishing 10
2.3 Conclusion 11
Chapter 3 Gain and Lasing near 2 μm in Thulium-doped Tantalum Pentoxide 13
3.1 Introduction 13
3.1.1 Thulium-doped CMOS-compatible Materials 14
3.2 Fabrication 16
3.2.1 Deposition 17
3.2.2 Annealing 17
3.3 Characterisation 17
3.3.1 Refractive Index, Surface Roughness and Loss Measurements 17
3.3.2 Excited-state Lifetime and Photoluminescence Measurements 18
3.3.3 PL and Lifetime Dependence on Annealing Temperature and Duration 21
3.3.4 PL and Lifetime Dependence on Thulium Concentration 22
3.4 Spectroscopic Measurements of Tm:Ta_2O_5 23
3.4.1 Emission Spectrum Measurements 23
3.4.2 Tm:Ta_2O_5 Rib Waveguide Fabrication 26
3.4.3 Absorption Spectrum and Cross-section 27
3.5 Tm:Ta_2O_5 Waveguide Lasers 29
3.5.1 Laser Operation 30
3.5.2 Pump Launch Efficiency 31

3.5.3 Lasing from Polished End-Facets 32
3.5.4 Lasing with Mirrors 34
3.6 Conclusion 35
Chapter 4 Second-order Nonlinearity in Tantalum Pentoxide 37
4.1 Introduction 37
4.1.1 Second-order Nonlinearity Materials 39
4.1.2 Thermal Poling 40
4.2 Fabrication 41
4.2.1 Cleaning Process 42
4.2.2 Sputtering 42
4.2.3 Annealing 42
4.3 Characterisation 43
4.3.1 Thickness Measurements 43
4.3.2 Refractive Index Measurements 43
4.3.3 Crystallinity 44
4.4 Thermal Poling 45
4.4.1 Thermal Poling Process 45
4.4.2 Depth Distribution of Second-order Nonlinearity Layer 45
4.4.3 Second-order Nonlinearity in Ta_2O_5 48
4.5 Impedance Spectroscopy 51
4.5.1 Electrical Characterisation using Impedance Spectroscopy 51
4.5.2 Electrochemical Impedance Spectroscopy 54
4.5.3 Resistivity of Thin Film 55
4.6 Discussion 57
4.7 Conclusion 59
Chapter 5 Multilayer Grating-assisted Coupler between Silicon-on-Insulator and Tantalum Pentoxide Waveguides 61
5.1 Introduction 61
5.1.1 Grating-assisted Coupler Theory 62
5.2 Grating-assisted Coupler Design and Simulation 62
5.2.1 Waveguides Cross-section 63
5.2.2 Grating Period 65
5.2.3 Grating-assisted Coupler Propagation along Waveguide Length 67
5.2.4 Grating Position 68
5.3 Device Fabrication 69
5.3.1 E-beam Mask Design 71
5.3.2 E-beam Lithography of Alignment Marks, Si Gratings and Waveguides 73
5.3.3 Etching of Alignment Marks, Si Gratings and Waveguides 73
5.3.4 Deposition and Annealing of SiO_2 Gap 73
5.3.5 Deposition and Annealing of Ta_2O_5 73

5.3.6 E-beam Lithography of Ta_2O_5 Waveguides....73
5.3.7 Etching of Ta_2O_5 Waveguides....73
5.3.8 Deposition and Annealing of SiO_2 Cladding Layer....74
5.3.9 Polishing....74
5.4 Fabrication Evaluation....74
5.5 Experimental Characterisation....76
5.6 Conclusion....77
Chapter 6 Conclusion and Future Work....79
5.7 Future Work....81
5.7.1 Multilayer Tm:Ta_2O_5 Ring Resonator Laser....81
5.7.2 Integrated Electro-optic Device in Ta_2O_5....82
References....83

List of Figures

Figure 1: Waveguide geometries a)slab waveguide, b)channel waveguide, c)rib waveguide and d)buried channel waveguide 5
Figure 2: SEM cross-section image of waveguide on sample a)I1, b)I2 and c) I3 9
Figure 3: SEM cross-section of RIE-etched waveguide 10
Figure 4: Energy level diagram for Tm^{3+} ions with the common pump transitions and laser transitions 15
Figure 5: Refractive index and surface roughness of Tm:Ta_2O_5 annealed at 500, 550, 600 and 650 °C for 2 hours 18
Figure 6: Characterisation setup for lifetime measurements 19
Figure 7: Photoluminescence decay for sample annealed at 650 °C for 12 hrs 20
Figure 8: Normalised fluorescence intensity at different pump wavelengths at room temperature 20
Figure 9: a) Excited-state lifetime and b) photoluminescence peak power for samples annealed at 500, 550, 600, 650 °C for 2 and 12 hours 21
Figure 10: Excited-state lifetime measurement for samples annealed at 650 °C for 12, 48 and 96 hours 22
Figure 11: Peak photoluminescence intensity and lifetime for 1, 2 and 3 wt% Tm:Ta_2O_5, annealed for 12 hrs 23
Figure 12: Characterisation apparatus for photoluminescence lifetime measurements 24
Figure 13: Emission spectrum of Tm:Ta_2O_5 when pumped at 775, 780, 795 and 800 nm 24
Figure 14: Emission spectrum of Tm:Ta_2O_5 with pump wavelength of 795 nm taken with Thorlabs OSA203C OSA 25
Figure 15: Emission cross-section of Tm:Ta_2O_5 annealed at 650 °C for 12 hours 26
Figure 16: Tm:Ta_2O_5 rib waveguide dimensions 27
Figure 17: Setup for absorption spectrum measurement 27
Figure 18: Absorption cross-section spectrum of Tm:Ta_2O_5 29
Figure 19: Mode profiles of 3 μm wide Tm:Ta_2O_5 rib waveguide at a) 795 nm and b) 1866 nm, and camera image of output from 3 μm wide Tm:Ta_2O_5 rib waveguide at 795 nm 30
Figure 20: Setup for waveguide laser characterisation 33
Figure 21: Lasing spectrum showing lasing peaks at 1238 and 1858 nm, at incident pump power of 170 mW at 795 nm pump wavelength 33
Figure 22: Setup to characterise waveguide laser with mirror at output end-facet 34
Figure 23: a) Lasing spectrum with incident pump power of 220 mW and b) incident pump power vs output power 35
Figure 24: Mechanism of thermal poling 41
Figure 25: Dispersion curves of refractive indices of annealed and unannealed Na-doped Ta_2O_5 films and annealed and unannealed undoped Ta_2O_5 films, obtained by ellipsometry 43
Figure 26: XRD diffraction pattern of unannealed and annealed a) Ta_2O_5 and b) Na:Ta_2O_5 thin films 44
Figure 27: Monitored applied electric field (V) and current (i) through thermal poling process 45
Figure 28: Micro-SHG experimental setup 46
Figure 29: SHG profiles, of Na:Ta_2O_5 amorphous thin films on borosilicate substrate poled at 1.3 kV and 2.0 kV 47
Figure 30: XPS depth profile measurement of 4 μm annealed Na:Ta_2O_5, poled at 1.3 kV and zoomed-in Na concentration (insert), dotted lines mark the film/substrate interface 48
Figure 31: Time dependence of the SHG intensity of thermally poled annealed and unannealed Na-doped and undoped Ta_2O_5 layers on borosilicate glass substrate 50

Figure 32: Complex impedance plane 51
Figure 33: Frequency response from impedance spectroscopy of a parallel RC circuit represented as a) Nyquist plot and b) bode plots 53
Figure 34: Equivalent circuit model of sputtered Ta_2O_5 film reported by Duggan et al. [123], where R_e is the electrodes resistance, C_d is the double layer capacitance, R_i is the ionic resistance and C_g is the geometric capacitance between electrodes..... 53
Figure 35: Setup for impedance measurement..... 54
Figure 36: Fitting of impedance data of Borofloat 33 substrate (blue line) with an equivalent circuit model (red line)..... 55
Figure 37: Nyquist plot of Borofloat 33 substrate, unannealed and annealed Na:Ta_2O_5 on Borofloat 33 substrate at 300 °C, with manual fitting of semicircles 56
Figure 38: a) Grating-assisted coupler b) phase-matching condition 62
Figure 39: Schematic of grating-assisted coupler a)cross-section and b)along the waveguide propagation 63
Figure 40: Cross-section of simulated waveguides a) Ta_2O_5 and b) Si..... 64
Figure 41: Cross-section simulation of a a) Ta_2O_5 channel waveguide and b) Si channel waveguide and its equivalent slab waveguide c) Ta_2O_5 slab waveguide and d) Si slab waveguide in TE polarisation 65
Figure 42: Grating period varying with waveguide separation..... 66
Figure 43: Cross-sectional model of grating-assisted coupler a) compound mode in Ta_2O_5 and b) compound mode in Si waveguides 67
Figure 44: Power exchange between Si and Ta_2O_5 waveguide..... 68
Figure 45: Position of grating in grating-assisted coupler at the bottom of top waveguide.... 68
Figure 46: Power exchange with gratings underneath the Ta_2O_5 waveguide 69
Figure 47: Grating-assisted coupler process flow..... 70
Figure 48: Grating-assisted coupler mask design 72
Figure 49: Grating-assisted coupler cross-section at a) coupling region, b)end-facet with no tapered waveguides, and c) end-facet with tapered Si waveguide..... 72
Figure 50: Microscope image of 750 x 750 nm Ta_2O_5 waveguide after IBM milling..... 74
Figure 51: Cross-section of grating-assisted coupler after fabrication 75
Figure 52: Power exchange between Si and Ta_2O_5 waveguide with waveguide dimensions after IBM at operating wavelength of 1.6 μm..... 76
Figure 53: Apparatus for characterising grating-assisted coupler..... 77
Figure 54: Initial characterisation of grating-assisted coupler with a HeNe input from a Ta_2O_5 77
Figure 55: Multilayer Tm:Ta_2O_5 ring resonator laser configuration..... 82

List of Tables

Table 1: Deposition conditions for Ta_2O_5 films 6
Table 2: Ion-beam milling parameter for etching sputtered Ta_2O_5 8
Table 3: Different beam currents and beam accelerator voltages tested 9
Table 4: Sputtering conditions for SiO_2 10
Table 5: Refractive indices of Ta_2O_5 films at the Maker fringe wavelengths 44
Table 6: Electrode area (A) and film or substrate thickness (l) for Borofloat 33 substrate and Na-doped and undoped Ta_2O_5 56
Table 7: Resistivity (Ωm) extracted from impedance measurements of 4 µm unannealed and annealed Na-doped Ta_2O_5 layers, and unannealed and annealed undoped Ta_2O_5 layers performed at 200 and 300 °C 57

Nomenclature

SOI	Silicon-on-insulator
CMOS	Complementary metal oxide semiconductor
Si	Silicon
IR	Infrared
Tm	Thulium
Na	Sodium
RF	Radio frequency
Ar	Argon
RIE	Reactive ion etching
IBM	Ion beam milling
OSA	Optical spectrum analyser
HMO	Heavy metal oxide
SHG	Second harmonic generation
UV	Ultraviolet
DC	Direct current
XRD	X-ray powder diffraction
ITO	Indium tin oxide
NLO	Nonlinear optics
EDX	Energy-dispersive x-ray
XPS	X-ray photoelectron spectroscopy
AC	Alternating current
FFT	Fast Fourier transform
EIS	Electrochemical impedance spectroscopy
EFISH	Electric field induced second harmonic generation
TE	Transverse electric
ICP	Inductively-coupled plasma
CCD	Charge-coupled device

Declaration of Authorship

I, Amy Sen Kay Tong, declare that this thesis entitled “Tantalum Pentoxide Integrated Photonic Devices” and the work presented in it are my own and has been generated by me as the result of my own original research.

I confirm that:

1. This work was done wholly or mainly while in candidature for a research degree at this University;
2. Where any part of this thesis has previously been submitted for a degree or any other qualification at this University or any other institution, this has been clearly stated;
3. Where I have consulted the published work of others, this is always clearly attributed;
4. Where I have quoted from the work of others, the source is always given. With the exception of such quotations, this thesis is entirely my own work;
5. I have acknowledged all main sources of help;
6. Where the thesis is based on work done by myself jointly with others, I have made clear exactly what was done by others and what I have contributed myself;
7. None of this work has been published before submission

Signature:		Date:	

Acknowledgement

This thesis would not have been possible without the help, support and guidance of many people. Firstly, I wish to express my sincere gratitude to my supervisor, Prof. James Wilkinson, for his continuous guidance and support throughout my PhD. Thank you for giving me this interesting project.

I would also like to thank my co-supervisor Prof. Michalis Zervas who has provide me guidance throughout this PhD especially with understanding my results. I would also like to show my gratitude to Dr. Senthil Ganapathy who have provided enormous help with any problems ranging from the lab equipment to fabrication to any problems with I may have with my results. A word of thanks to Dr Jacob Mackenzie in his help with the laser experimental setup and understanding the theory.

I would like to thank all (present and previous) members of the Integrated Photonic Devices group, Vinita Mittal, Colin Mitchell, Shahab Bakhtiari, Jon Butement, Dave Rowe, Ping Hua, Mohd Narizee, Zilong Wang, who have provided great help and support throughout my PhD. My sincere thanks to Armen Aghajani, who provided me help throughout the time he was here and coming back especially to help with the lasing experiments. Many thanks also to Neil Sessions for all the help and support with any fabrication issues within the cleanroom.

I am extremely grateful to my parents and sister who have encouraged and supported throughout my PhD. A final special thank you to Nicholas who has provided endless emotional and physical support for the past 4 years.

All the work in this thesis have been supported by the UK Engineering and Physical Sciences Research Council (EPSRC) program grant, Silicon Photonics for Future Systems (EP/L00044X/1).

Dedicated to my family

Chapter 1 Introduction

Photonic integrated circuits are devices which integrate multiple optical functionalities in a single monolithic chip fabricated by process developed for microelectronics. As in integrated electronics, functionalities such as gain, all-optical and electro-optic switching, feedback and frequency filtering are needed to realise a full range of circuit capability. There are three main material platforms for photonic integrated circuits, silicon photonics, dielectrics and III-V semiconductors. In particular, silicon-on-insulator (SOI) waveguide technology offers high performance with standard wafer processing, for mass-market applications [1]. These provides a route to highly functional low-cost optoelectronic and all-optical devices, and are a field of rapid commercial growth.

Silicon photonics has gained attention as a platform for applications such as telecommunications, high-performance computing and sensing [1]. It allows the integration of many components, realised by existing complementary metal-oxide semiconductor (CMOS) technology, onto the same platform. However there are a few challenges of silicon as a photonic material. Silicon (Si) is an indirect bandgap material and therefore an inefficient light emitter. However there are two main methods reported to achieve light emission on a silicon platform, integration of III-V semiconductor lasers and rare-earth doped lasers. Silicon also does not exhibit any inherent electro-optic effect required for realising effective modulators, which are an important component in an optical communication system. To address this, development of functionalities on other materials to incorporate with silicon have been investigated.

Thin film dielectric waveguides exploit existing silicon process technology and complement SOI waveguides in providing these functions on a multilayer silicon photonic circuits or all-dielectric circuits [2] for applications from short reach interconnects to long haul telecommunications, and sensing and defence applications in the mid-infrared (mid-IR) wavelengths. To allow for integration with silicon photonics platform, any material used has to be compatible with CMOS fabrication technology. Silicon nitride (Si_3N_4), aluminium oxide (Al_2O_3) and tantalum pentoxide (Ta_2O_5) are the three leading candidates for integration of dielectric waveguides on silicon, due to their silicon process compatibility and high refractive index, leading to potential for compact devices.

Ta_2O_5 is a high-permittivity dielectric material ideal for optical integrated devices and waveguides. It is a promising material for integration with silicon photonic devices as it is CMOS compatible and has been used in the microelectronics industry for gate dielectric [3]. High third-order nonlinearity ($\chi^{(3)}$) without two-photon absorption has been exploited in Si_3N_4 and Ta_2O_5 waveguides [4, 5]. Ta_2O_5 has a high nonlinear

refractive index of $72.3x10^{-20}$ m^2/W at 800 nm [5], which is around 30 times larger than that of silica, $2.36x10^{-20}$ m^2/W [6], and around 10 times larger than that of Si_3N_4, $9x10^{-16}$ m^2/W [7]. Compared with Si_3N_4, Ta_2O_5 is also better for hosting rare-earth ions which have been previously demonstrated with ytterbium [8], erbium [9] and neodymium [10] to realise waveguide lasers. Although there have been reports of gain or lasing in Al_2O_3 with rare-earth doping like ytterbium [11], erbium [12] and thulium [13], the refractive index of Ta_2O_5 (~2.1 at λ~1.55 μm) is higher than that of Al_2O_3 (~1.7 at λ~1.55 μm). It gives a high index contrast between the waveguide core and silica cladding giving a better mode confinement and higher guided optical intensity in the waveguide allowing the realisation of tight bends and compact devices. The large operation wavelength range up to 8 μm [14]. Extremely low loss waveguides have recently been reported in Ta_2O_5, of 3 dB/m [15]. Ta_2O_5 a competitive candidate among the three dielectric materials compatible with silicon. This thesis explores tantalum pentoxide as a dielectric material to realise monolithic integrated devices, in particular light source, electro-optic devices and multilayer coupler, to complement existing silicon photonics technology.

This thesis investigates Ta_2O_5 as a potential material for realising laser sources and electro-optic devices for integration with silicon photonics. The Ta_2O_5 waveguides are fabricated using CMOS-compatible fabrication process, RF sputtering, annealing, lithography, etching, resist removal and lapping and polishing. To ensure smooth waveguide sidewall roughness to realise low loss devices, the etching process is optimised. Ta_2O_5 doped with thulium-ions is investigated for the first time as a gain material to realise integrated laser sources at around 2 μm. The emission and absorption cross-section and lifetime are established allowing the calculation of gain and laser threshold. A first demonstration of inducing second-order nonlinearity in Ta_2O_5 by thermal poling is also described. This allows the realisation of electro-optic functionalities. The nonlinearity of thermally-poled Ta_2O_5 is determined, however, an issue with the instability is found. The samples are characterised electrically to understand this instability. To incorporate these functionalities onto a silicon platform, a grating-assisted coupler has been designed and fabricated to couple between a silicon and Ta_2O_5 waveguide layer. This allows the coupling of lasing from thulium-doped Ta_2O_5 or provide gain in SOI circuit.

1.1 Thesis Structure

This section outlines the work covered in each chapter of this thesis.

Chapter 2 provides an overview of the fabrication steps for Ta_2O_5 rib and channel waveguides on oxidised Si wafer, starting from lithography, etching to polishing of the end-facets. The specific fabrication process will be detailed in its respective chapter.

Chapter 3 describes the investigation of using thulium-doped tantalum pentoxide ($Tm:Ta_2O_5$) as a potential gain medium. The study of the spectroscopic properties of $Tm:Ta_2O_5$, such as excited-state lifetime, emission and absorption cross-section, is presented. $Tm:Ta_2O_5$ waveguide laser was realised and its lasing characteristics will be reported.

Chapter 4 demonstrates the induction of second-order nonlinearity in Ta_2O_5 by thermal poling. Optical and electrical characterisation, and the thermal poling process of the thin film are described. The study of annealing and doping with sodium (Na) ions on the second-order nonlinearity intensity and stability will be discussed.

Chapter 5 investigates using grating-assisted coupler to couple between a silicon and Ta_2O_5 waveguide layer. Simulations of the device was used to determine the grating period required. The fabrication of the grating-assisted coupler is also detailed in this chapter.

Chapter 6 summarises all the chapters of the thesis and suggest future endeavours to integrate the Ta_2O_5 devices together on silicon platform.

1.1.1 List of Publications

This section lists the publications linked with this thesis and also outreach publications during this PhD.

Conference Papers

1. **A. S. K. Tong**, C. J. Mitchell, J. I. Mackenzie and J. S. Wilkinson, "Photoluminescence Of Tm-doped Ta_2O_5 Waveguides," poster presentation at Conference on Lasers and Electro-Optics Pacific Rim (CLEO-PR), Singapore, August 2017. (Awarded 3rd Place Best Poster Prize)

Journal Articles

1. **A. S. K. Tong**, F. Bondu, G. S. Murugan, J. S. Wilkinson and M. Dussauze, "Effect of Sodium Addition and Thermal Annealing on Second-order Optical Nonlinearity in Thermally Poled Amorphous Ta_2O_5 Thin Films", *J. of Appl. Physics*, vol. 125, no. 1, p. 015104, 2019.
2. A. Raza, S. Clemmen, P. Wuytens, M. de Goede,, **A. S. K. Tong**, N. Le Thomas, A. Skirtach, S. M. Garcia Blanco, S. Honkanen, J. S. Wilkinson and R. Baets, "High Index Contrast Photonic Platforms for On-chip Raman Spectroscopy", Optics Lett., October 2018 (Submitted)

3. **A. S. K. Tong**, C. J. Mitchell, J. I. Mackenzie, A. Aghajani, G. S. Murugan and Wilkinson J. S., “Spectroscopy and Lasing of Thulium-doped Tantalum Pentoxide Waveguides” Optics Material Exp.. (In preparation)

Other Conference and Journal Article

1. N. H. L. Wong, **A. S. K. Tong** and M. T. Posner, “Modular and Extensible Lesson on Optical Fibre Communication for Youths”, IOP Physics Education, December 2018. (Accepted)
2. N. H. L. Wong, **A. S. K. Tong**, M. T. Posner and A. Ravagli, “Modular and Extensible Lesson on Fibre Optics for Youths”, Proc. Vol. 10452, 14th Conference on Education and Training in Optics and Photonics: ETOP 2017, Hangzhou, China, August 2017.

Chapter 2 Tantalum Pentoxide Waveguide Design and Fabrication

2.1 Introduction

Waveguides confine and guide light in devices and photonic integrated circuits. The waveguide geometry is dependent of the application and size of device. There are four main waveguide geometries, slab waveguide, channel waveguide, rib waveguide and buried channel waveguide. They are shown in Figure 1.

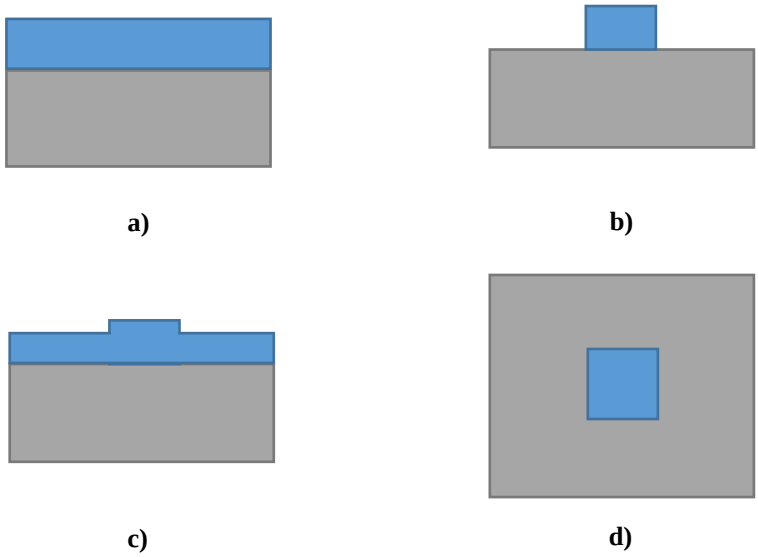

Figure 1: Waveguide geometries a)slab waveguide, b)channel waveguide, c)rib waveguide and d)buried channel waveguide

Slab waveguides (Figure 1a)) are waveguides which do not require any etching methods to realise the waveguide. The mode is confined only in the vertical dimension and has no lateral confinement. They are useful for applications such as sensing where a large area of evanescent field on the waveguide surface can be achieved. However this infinite spatial range is not suitable for most other applications. The other three configurations provide both vertical and lateral mode confinement. Channel waveguides (Figure 1b)) are fully etched waveguides. It provides good mode confinement as its three edges are surrounded by a lower index material. Therefore it is suitable for realising compact devices. Unlike the channel waveguide, rib waveguides (Figure 1c)) are partially etched. It provides a larger mode cross-section dimensions which can improve the input and output coupling efficiency with a fibre and fabricated using conventional lithography. Same as a channel waveguide but surrounded with cladding of the same refractive index all around the waveguide, buried channel waveguide (Figure 1d)) is useful for applications requiring a circular mode

profile. In this thesis, Ta_2O_5 integrated devices were realised with slab waveguides, channel waveguides or rib waveguides. The specific design and fabrication parameters will be detailed in their respective device chapters.

2.2 Fabrication

Ta_2O_5 waveguides were fabricated using CMOS compatible process on 4" silicon wafers with 2.5 μm thermal oxide. This allows the integration with a silicon platform. Various Ta_2O_5 waveguide configurations have been investigated in this thesis and specific fabrication parameters will be described in more detail in their respective sections. The fabrication steps of Ta_2O_5 waveguides, which will be detailed in the sections below, are as follows:

1. Deposition of Ta_2O_5 layer with RF sputtering
2. Annealing Ta_2O_5 layer
3. Lithography to pattern the resist layer
4. Ion-beam milling to realise the waveguides
5. Removal of resist layer
6. Annealing Ta_2O_5 layer
7. Overcladding by sputtering a layer of SiO_2
8. Annealing of overcladding layer
9. Lapping and polishing to achieve optical quality end-facets

2.2.1 Deposition

There are several chemical vapour deposition (CVD) or physical vapour deposition methods reported for depositing Ta_2O_5 thin films, such as e-beam evaporation [16], atomic layer deposition [17], and ion-assisted deposition [18]. Sputtering is a common method for thin film deposition in the semiconductor industry with its advantages of a uniform film over large area and good adhesion [19]. The radio frequency (RF) field is induced by a magnetron, ionising the inserted argon gas molecules, creating a plasma. The argon ions are accelerated towards the negatively charged Ta_2O_5 target causing atoms to be removed from the target. These atoms then fall onto the wafer depositing a thin film on the substrate.

Table 1: Deposition conditions for Ta_2O_5 films

Argon (Ar)	20 sccm
Oxygen (O_2)	5 sccm
RF power	300 W
Pressure	10 mTorr
Temperature	200 °C

Deposition of the Ta_2O_5 films was performed using Oxford Instruments Plasmalab System 400 sputtering system, under the conditions listed in Table 1. These parameters were found to be the optimal conditions to give the lowest loss erbium-doped Ta_2O_5 slab waveguides using this sputtering system [20]. As an initial test to determine the

deposition rate, a test deposition was performed on a microscope slide. Kapton tape was stuck on parts of the microscope slide before deposition, and was removed after the deposition. The difference in thickness between the surface of the film and microscope slide was then measured using the stylus profilometer, which was used to calculate the deposition rate. From the known deposition time and measured thickness of film, the deposition rate was calculated to be 3.33 nm/min.

2.2.2 Annealing

Annealing is performed after the deposition of the films in a Severn (STS) 1200 °C tube furnace. Due to the onset of crystallisation for Ta_2O_5 occurs around 650 to 700 °C [21, 22], the Ta_2O_5 samples are annealed at 600 °C for 2 hours, in an oxygen atmosphere, O_2 flow of 2 l/min, and heating up at 2 °C/min and cooling down at 1 °C/min. This helps relieve any stress built up in the films as well as to replenish the oxygen, and improve the stoichiometry, which has been depleted during the sputtering process. The samples are annealed again after the etching step described in 2.2.4 to replenish any oxygen which might have been loss during etching.

2.2.3 Lithography

Lithography is a widely used technique to pattern a sample. Two methods of lithography were used to pattern the resist layer depending on width of waveguides. Conventional photolithography has a resolution limit of approximately 1 μm, therefore for 750 nm wide waveguides, e-beam lithography was used. For both methods, a mask or design of the waveguide pattern is required. For the 750 nm wide waveguides, the e-beam waveguide design was created in L-edit and converted into a GDS file which will be used in the controlling software for the e-beam lithography. For the photolithography mask, a chromium mask with waveguides varying from 1.5 to 5 μm was already available.

2.2.3.1 E-beam Lithography

A 900 nm layer of electron-sensitive negative resist (ZEP-520A) was spin-coated on top of the Ta_2O_5 followed by a layer of conductive polymer (e-spacer) which prevents a build-up of charge. A focussed electron beam scans across the layer of electron-sensitive ZEP negative resist. The pattern of the mask is exposed on the resist. After the exposure, the e-spacer layer is first removed by water. The resist was then developed using ZED-N50 developer. The samples were written with the help of Dr Ali Khokhar.

2.2.3.2 Photolithography

The wider waveguides are patterned using conventional photolithography. S1813 photoresist was spin-coated on sample at 5000 rpm for 60 secs, which gives an uniform resist layer of around 1.3 μm. The photoresist was soft-baked in oven at 120 °C oven

for 30 mins, to drive out the solvent from the resist and improve adhesion to the film. This is followed by the expose of photoresist with UV light (λ=365 nm) through the chromium mask with MA6 mask aligner in hard contact mode for 8.5 secs. The photoresist is then developed in MF-319 developer for 45 secs. Finally, the sample is hard-baked in 90 °C oven for 30 mins to enhance the resistance of the resist during etching.

2.2.4 Etching

Ta_2O_5 have been used in microelectronics industry and there have been research into the types of etching processes, including reactive ion etching (RIE) and ion-beam milling (IBM). Waveguides were etched with both methods to compare the sidewall roughness.

Using ion-beam milling (Oxford Instruments Ionfab 300 Plus), waveguides were realised where the area of the sample uncovered by the photoresist is bombarded with argon ions and etched away. The sample was attached to the sample holder with a high thermal conductivity non-curing heat transfer paste to conduct the heat away from the sample. This sample holder is angled at -45 ° to the ion-beam and rotates at 5 rpm to ensure a uniform etch and avoid any redeposition on the sample. The parameters used for etching Ta_2O_5 are listed in Table 2. This gives an etch rate of approximately 14 nm/min for Ta_2O_5 and etch selectivity of approximately 1:1.

Table 2: Ion-beam milling parameter for etching sputtered Ta_2O_5

RF power	500 W	**Ar gas flow rate**	6 sccm
Beam voltage	500 V	**He pressure**	20 mτ
Neutraliser current	300 mA		

The beam current and beam accelerator voltage were varied to observe the effect of these two parameters on the waveguide sidewall roughness. Figure 2 shows the scanning electron microscope (SEM) images of sample I1, I2 and I3, where the beam current has been varied. From all six samples, sample I1 appeared to have the most vertical sidewalls and are also smooth. From the SEM images, the lower beam accelerator voltage for sample I4, I5 and I6 appeared not to have any effect on the shape and sidewall roughness, similar to I1 and I2. However as they used lower beam accelerator, the etch rate was slower. Therefore a beam current of 100 mA and beam accelerator of 300 V were chosen.

Table 3: Different beam currents and beam accelerator voltages tested

Sample	Beam current, mA	Beam accelerator, V
I1	100	300
I2	60	300
I3	30	300
I4	100	200
I5	100	100
I6	60	200

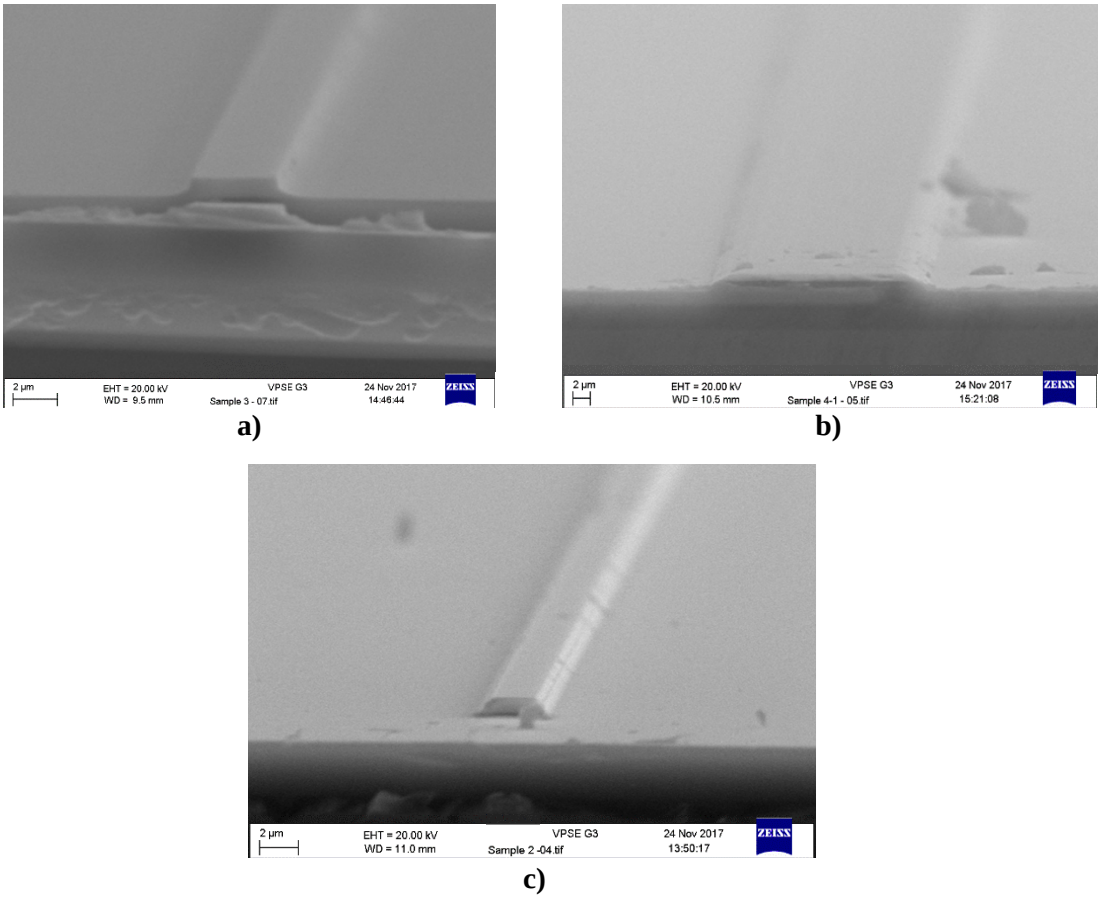

Figure 2: SEM cross-section image of waveguide on sample a)I1, b)I2 and c) I3

RIE is the most common method to etch Ta_2O_5, performed using fluorine gas chemistry with species such as CF_4 and CHF_3 [23, 24]. RIE occurs in a vacuum chamber where a RF field is applied creating a plasma of ionised gas molecules [25]. Due to the electric field induced by the electrodes, ions are attracted to the sample's surface. The ions react chemically with the sample surface leading to the removal of material. Two RIE recipes were used [26, 27] to realise Ta_2O_5 waveguides using Oxford Instruments Plasmalab 80 Plus. The waveguides cross-section were observed in the SEM after resist removal and polishing, rounded corners (Figure 3) were observed and the other recipe had no structures after the removal of resist. Therefore it was decided that IBM was to be used to realise the Ta_2O_5 waveguides.

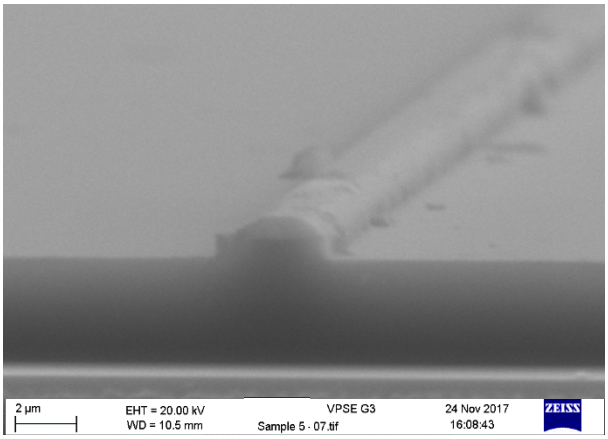

Figure 3: SEM cross-section of RIE-etched waveguide

2.2.5 Resist Removal

After the etching of the waveguides, the resist is removed. Firstly, the sample is placed in a beaker filled with acetone in an ultra-sonic bath for 15 mins. To ensure the complete removal of the resist, a plasma ashing step is followed. Oxygen plasma inside the plasma asher (PVA Tepla 300) removes any of the organic resist.

2.2.6 Cladding

The last step of Ta_2O_5 fabrication is to clad the waveguides with a SiO_2 layer. This helps protect the surface of the waveguides. A 2 µm thick SiO_2 cladding layer is sputtered using the Oxford Instruments Plasmalab System 400 at 20 °C, using the parameters listed in Table 4. The rate of deposition was 3.33 nm/min.

Table 4: Sputtering conditions for SiO_2

Power	300 W	**Ar**	20 sccm
Pressure	10 mτ	**O_2**	5 sccm

The cladding layer is then annealed at 600 °C for 2 hours, ramping temperature up at 2 °C/min and down at 1 °C/min, with O_2 flow of 2 l/min. This was performed at the same temperature as Ta_2O_5 to prevent the crystallisation of Ta_2O_5.

2.2.7 Lapping and Polishing

Light is launched into the waveguides by butt coupling, therefore the quality of the end facets are important. To enhance the coupling efficiency into the waveguides, the waveguide facets are lapped and polished. The sample is lapped down with a coarse abrasive slurry to remove any damages or scratches. Firstly using 9 µm Al_2O_3 slurry

for around 30 mins, followed by 3 µm Al_2O_3 slurry for another 20 mins. This removes any damage or scratches due to the 9 µm Al_2O_3 slurry, the samples are then ready to be polished. Polishing with syton (SF1) was used to ensure an optical finish to the facets.

2.3 Conclusion

The fabrication of Ta_2O_5 waveguides was detailed in this chapter. Ta_2O_5 is sputtered on oxidised Si 4" wafers and patterned using lithography. Waveguide shape and sidewall roughness are important when fabricating waveguides. They affect the effective index and losses of the waveguides. Waveguides etched with various RIE and IBM recipes were compared. IBM appeared to give a sharper waveguide profile compared with RIE, which gives a rounded profile. Therefore IBM was chosen to be the etching process. The waveguides are then cladded with SiO_2. Finally, the end facets are lapped and polished for butt coupling. Detailed design and fabrication parameters and results for each process are given in the chapters on each device.

Chapter 3 Gain and Lasing near 2 μm in Thulium-doped Tantalum Pentoxide

3.1 Introduction

The design, fabrication and characterisation of thulium-doped tantalum pentoxide ($Tm:Ta_2O_5$) lasers for integration onto a silicon platform is discussed in this chapter. Thulium-doped lasers offers an operating wavelength between 1.8 to 2.1 μm, with a pump excitation of 790 nm.

There has been significant research in the development of integrated optical sources and amplifiers. In particular, integration of laser sources and amplifiers on a silicon platform has been widely researched. Due to silicon being an indirect bandgap semiconductor, it is an inefficient light emitter. One of the method is to integrate rare-earth-doped laser sources directly on the silicon platform, allowing for monolithic integration and wafer scale manufacturing. However this requires a gain material which is compatible with silicon. Integrated rare-earth-doped lasers on silicon platform have been demonstrated with rare-earth doping such as ytterbium and erbium [28, 29, 30, 31, 32]. To extend the operation wavelength of silicon photonics to 2 μm, thulium-doped lasers can be integrated, where silicon also has a lower two-photon absorption, by around 5 times compared to at 1.55 μm [33].

There is a wide range of applications in the 2 μm wavelength region including optical communications, spectroscopy, medical surgeries, LIDAR and remote sensing. In particular for optical communications, 2 μm have had increasing interest in recent years. With the ever increasing internet traffic, data capacity has been approaching the Shannon's limit. One of the solution to tackle the 'capacity crunch' is to increase the bandwidth by opening up a transmission window around 2 μm, broadening the current transmission window around 1.55 μm [34]. This has led to the recent developments of optical devices operating in the 2 μm region for optical communication to tackle the 'capacity crunch', for example the development of hollow-core photonic bandgap fibres which have predicted low losses of 0.1 dB/km and lower nonlinearity around 2 μm compared with conventional silica fibres [35]. The emission region of thulium between 1.7 and 2.1 μm makes it a suitable candidate for gain and amplification optical devices in this interested wavelength region. The already existing erbium-doped optical devices will have to be replaced with ones operating at the 2 μm waveband. The recent developements of thulium-doped fibres [36] and amplifiers [37] are some examples.

However to date, there has only been two reports of 2 μm lasers compatible with silicon platform realised by doping amorphous films with thulium ions. This had been achieved with integrating silicon nitride (Si_3N_4) and Tm-doped alumina ($Tm:Al_2O_3$) in the form of a waveguide [13] and ring resonators [38].

As an alternative approach, combining the advantages of both Si_3N_4 and Al_2O_3, high index contrast and suitable host for rare-earth ions, in one material, Tm:Ta_2O_5 is investigated. Tantalum pentoxide (Ta_2O_5) is a promising material for realising photonic devices integrated with silicon photonics. It is CMOS compatible and its refractive index of 2.1 around 1.55 μm gives it a high index contrast with silica (SiO_2) cladding. This is higher than Al_2O_3 and Si_3N_4, allowing the realisation of tight bends and compact devices. Ta_2O_5 is also a good host for rare-earth ions to realise waveguide lasers, which had previously been demonstrated with neodymium [39], erbium [31], and ytterbium [30]. By doping Ta_2O_5 with thulium-ions, emission in the range of 1.7 to 2.1 μm ($^3F_4$ → $^3H_6$ transition) can be achieved by pumping at 795 nm ($^3H_6$ → $^3H_4$ transition).

3.1.1 Thulium-doped CMOS-compatible Materials

The main attractive feature of doping with thulium (Tm) ions is its emission in the range of 1.7 to 2.1 μm [40], corresponding to the $^3F_4 \rightarrow {}^3H_6$ transition, and also pumping around 0.8 μm [41]. It has several favourable properties including high quantum efficiency, wide gain bandwidth, and strong absorption band around 800 nm [42]. Thulium-doped lasers are commonly pumped at around 790 nm, due to availability of high-efficiency laser diode operating at around 800 nm and the strong absorption of the $^3H_6 \rightarrow {}^3H_4$. There have also been demonstration of in-band pumping at around 1550 nm [43], and 1200 nm [44]. Several advantages of pumping in this wavelength range include good overlap of pump and signal modes giving lower signal reabsorption and more efficient lasing from low photorefractive damage [45]. Thulium also has a larger emission bandwidth compared with erbium, which makes it favourable for broadband applications. High efficiency Tm lasers can be also achieved by pumping around 790 nm due to a 'two-for-one' cross-relaxation process occurring between the $^3H_4$ and $^3F_4$ levels [46]. Cross-relaxation process is where an ion in the excited state transfer energy to an ion in the ground state and therefore an ion from the ground state and excited state will both go to an intermediate state, commonly it will be the $^3F_4$ state. This improves the efficiency of Tm-doped laser emitting around 2 μm, as two Tm ions reaches the $^3F_4$ state for every ion that has been pumped [47].

Thulium-doped laser systems pumped at around 790 nm can be described simply as a 3-level laser system as shown in Figure 4. With a pump wavelength of around 790 nm, energy are transferred to the ions at the ground state $^3H_6$ exciting them to the $^3H_4$ excited state. Through non-radiative decay, the ion transit to the $^3F_4$ state. The ion from $^3F_4$ transit to the ground state causing emission around 2 μm. Population inversion can be achieved when more than half of the ions in the ground state are excited to the excited state and also a fast non-radiative decay from the excited state to $^3F_4$ level.

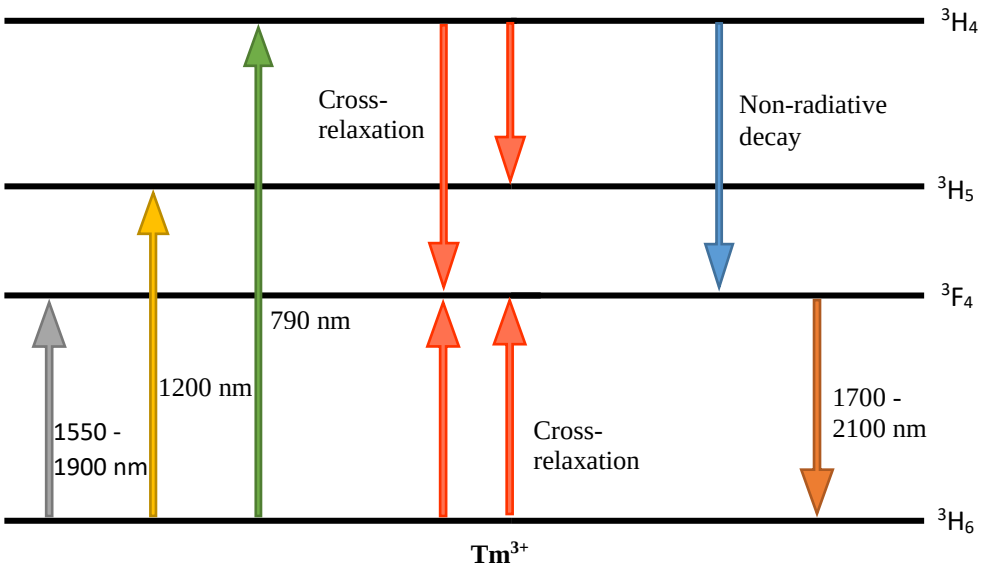

Figure 4: Energy level diagram for Tm^{3+} ions with the common pump transitions and laser transitions

3.1.1.1 Thulium-doped Aluminium Oxide (Al_2O_3)

With a higher refractive index of 1.7 compared with other CMOS-compatible amorphous materials such as silica and low fabrication temperatures, Al_2O_3 has been a candidate for rare-earth-doped lasers.

Thulium-doped aluminium oxide films were initially studied by J. J. Penninkhof [48]. The films were doped with Tm ion concentration of $1x10^{15}$ cm^{-3} with ion implantation at room temperature. The samples were annealed at 600, 800 and 900 °C in vacuum and 750 °C in air for an hour. Photoluminescence was observed at 1.6 µm for the samples annealed at 800 and 900 °C when excited with wavelength of 788 nm, and measured lifetime of 4.0±0.3 ms.

There has also been other reports of photoluminescence of sputtered Tm:Al_2O_3. For a dopant concentration of 1.6×10^{20} cm^{-3}, excited-state lifetime of 568 µs and absorption cross-section of 5.6×10^{-21} cm^2 at 785 nm was achieved [49]. Loiko et al. [50] with a Tm concentration of $5x10^{20}$ cm^{-3} achieved lifetime of 210 µs, emission cross-section of 0.47×10^{-20} cm^2 at 1808 nm and absorption cross-section of 0.45×10^{-20} cm^2 at 784 nm.

Recently, there have been two reports of lasing in Tm:Al_2O_3 in a ring resonator configuration [38] and in the form of a waveguide [13], with output power as high as 387 mW achieved in the later. They achieved a slope efficiency of 24% and 23% respectively and threshold pump power of 773 µW and 65 mW respectively.

3.1.1.2 Thulium-doped Tantalum Pentoxide

Ta_2O_5 has a similar refractive index as Si_3N_4 of around 2 making it a suitable candidate of compact devices. However to date, there has been no demonstration of a rare-earth-doped Si_3N_4 laser. Ta_2O_5 has a low phonon energy (100-400 cm^{-1}) which makes it an attractive material for hosting rare-earths [51]. It allows less non-radiative decay and longer excited-state lifetimes [52]. With less non-radiative decays occurring, allow higher quantum efficiencies to be achieved [53].

Thulium-doped tantalum pentoxide thin films were studied by K. Miura et al. [54, 55]. The method of deposition of these thin films is by co-sputtering. Thulium oxide (Tm_2O_3) pellets are placed on top of the tantalum pentoxide sputtering target and co-sputtered using a RF magnetron sputtering system. The films were deposited under the following conditions: argon flow rate of 15 sccm and RF power of 200 W. This is followed by annealing the samples in an electric furnace in ambient air at 600, 700, 800, or 900 °C for 20 mins. The samples were excited with a (helium-cadmium) HeCd 325 nm laser to measure the photoluminescence spectra. A sharp photoluminescence (PL) peak was observed around 800 nm, as the result of the $^3H_4$ -> $^3H_6$ transition of Tm^{3+}, for the sample annealed at 900 °C. The Tm concentration for this film was found to be approximately 2.3 mol% (~0.38 at%). In another paper, they published an observation of a photoluminescence peak around 400nm using the same fabrication method, a similar 800 nm peak from before was also obtained. Two pellets of Tm_2O_3 were used instead of three in the previous result.

Doping of tantalum pentoxide with thulium ions were also investigated by M. Macatrao et al. [56] on laser heated pedestal growth (LHPG)-grown Ta_2O_5 fibres. These fibres were doped with thulium ion concentrations of 0.1 at% and 1 at%. PL measurements performed with HeCd 325 nm laser showed PL dominated by the $^3H_4$ -> $^3H_6$ transition at 800 nm for fibres doped with 1 at%. With a resonant excitation with 476 nm, transitions $^1G_4$ -> $^3F_4$ (650 nm) and $^1G_4$ -> $^3H_5$ (780 nm) were also observed. Peaks due to the $^1G_4$ -> $^3H_4$ (1200 nm), $^3H_4$ -> $^3F_4$ (1500 nm) transitions and a nearby 1750 nm peak were attained pumping within the $^1G_4$ multiplet.

To my knowledge, there has been no report of lasing with thulium-doped tantalum pentoxide.

3.2 Fabrication

Tm:Ta_2O_5 thin films were fabricated by sputtering using processes described in Chapter 2 with the specific parameters described in this section. This was followed by an annealing process to improve the quality of the films.

3.2.1 Deposition

2 μm thick Tm:Ta_2O_5 thin films was deposited on 4" oxidised Si wafers using RF sputtering. A powder pressed sputtering target doped with 3 wt% (9 x 10^{20} ions/cm^3) of Tm_2O_3 was used, which is expected to yield a similar doping levels in the deposited films. The conditions used for sputtering is listed in section 2.2.1. After deposition, the 4" wafer was cleaved into samples of sizes 1 by 1.5 cm. These allowed the investigation into the effect of annealing temperature and duration on emission lifetime and fluorescence.

3.2.2 Annealing

Annealing of Tm:Ta_2O_5 thin films was performed to improve the stoichiometry and reduce the losses in the films. The samples were annealed in a tube furnace under oxygen atmosphere at temperatures of 500, 550, 600 and 650 °C for 2 and 12 hours to investigate the effect of annealing parameters on the photoluminescence. A temperature increment of 2 °C/min, decrement of 1 °C/min, and O_2 flow of 2 l/min was used.

3.3 Characterisation

The Tm:Ta_2O_5 thin films were characterised after annealing. Measurements to determine the refractive index, loss, excited-state lifetime and photoluminescence was performed.

3.3.1 Refractive Index, Surface Roughness and Loss Measurements

In order to understand the optical properties of the thin films, the refractive index, loss and surface roughness were evaluated. The refractive index and loss of the Tm:Ta_2O_5 slabs were measured using a prism coupling system, Metricon. From the modes of the waveguide, the refractive index and film thickness can be determined. These measurements were taken at both 633 and 1550 nm wavelength. The loss was determined from the scattering of the streak of propagation light measured using the Metricon, losses of 0.5 dB/cm was measured for 633 nm and around 0.1 dB/cm for 1550 nm. They were then compared with the surface roughness of the films, as shown in Figure 5. The surface roughness was measured with a non-destructive optical profiler, Zemetrics ZeScope. On average, the films had a roughness of 1.1 nm.

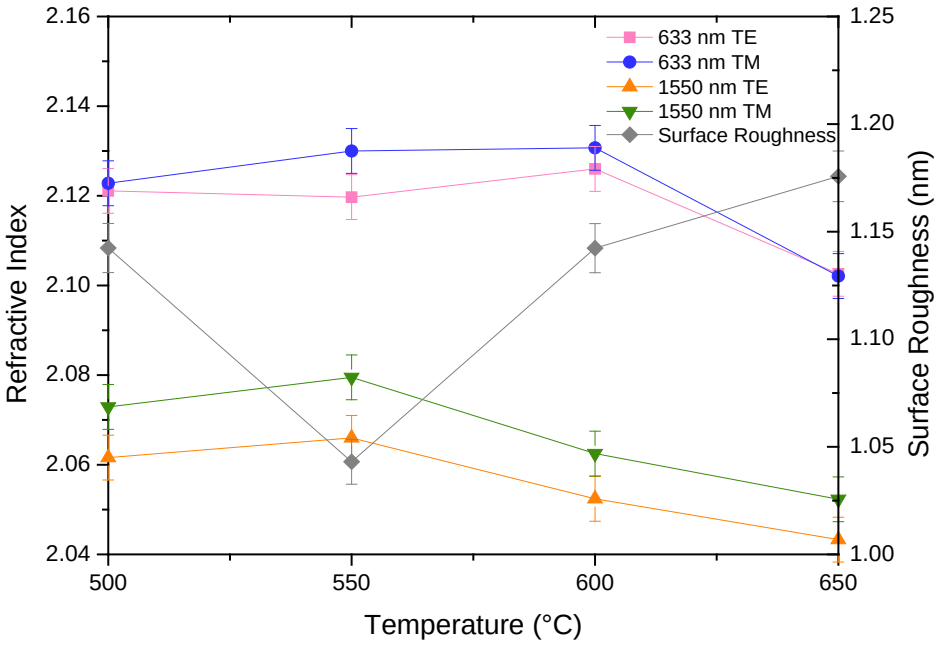

Figure 5: Refractive index and surface roughness of Tm:Ta_2O_5 annealed at 500, 550, 600 and 650 °C for 2 hours

The lowest surface roughness achieved, for samples annealed for 2 hours, was 1.04 nm which was attained with annealing at 550 °C. This matches with the highest refractive index measured for the four samples. The decrease in refractive index and increase in surface roughness for samples annealed at 600 and 650 °C could be due to the crystallisation of the Tm:Ta_2O_5 thin films. It has been reported that the crystallisation of Ta_2O_5 occurs at temperature around 650 °C [21, 22].

3.3.2 Excited-state Lifetime and Photoluminescence Measurements

The lifetime (τ) is the time required for the excited ions to decay to $\frac{1}{e}$ of its original population and indicates the time excited ions remain in the excited state before returning to ground state. The photoluminescence intensity, I(t) decay can be described simply with a single exponential decay according to equation 1 [57].

$$I(t) = I_0 e^{-\frac{t}{\tau}} \quad (1)$$

where I_0 is the initial intensity at time t = 0. By doing an exponential fitting to the photoluminescence intensity decay plot, from the slope of the decay, the lifetime can be determined. The fitting could be multi-exponential which suggests multiple de-excitation processes are occurring that could be due to defects in the material.

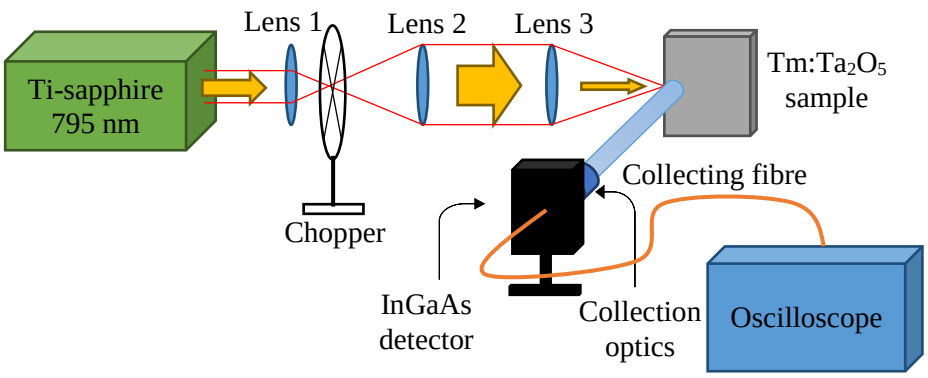

Figure 6: Characterisation setup for lifetime measurements

The lifetime of the sample was measured using the setup shown in Figure 6. A Ti-sapphire laser tuned at 795 nm and with a pump power of 625 mW was used to excite the Tm ions to the $^3H_4$ manifold. This was passed through a 25 mm (lens 1) and 100 mm (lens 2) lens which increased the beam diameter to around 4 mm. To allow a smaller focused spot to be achieved for coupling into the $Tm:Ta_2O_5$ slab via the side of the sample, a 50 mm focal length lens (lens 3 - Thorlabs LA1213-B, AR coating 650-1050 nm) is used before the sample. The spot size between lens 2 and 3 was measured using the knife-edge measurement, giving a horizontal $\frac{1}{e^2}$ beam radius of 2.06 mm and vertical of 1.91 mm. A chopper (50% duty cycle) is placed between lens 1 and lens 2, at the beam waist of lens 1, chopping the pump signal at 170 Hz. The fluorescence is then collected with a 1 mm core diameter SM2000 fibre which is connected to an InGaAs photodetector (Thorlabs DET10D, wavelength range 800-2600 nm, 25 ns rise time) via a packaged collection optics system. The collection optics contains a collimating lens (Thorlabs C230TMD-C, f = 4.51 mm, AR coating 1050-1700 nm), a long pass filter which filters below 1000nm and a focusing lens (Thorlabs C260TM-C, f = 15.29 mm, AR coating 1050-1620 nm) to focus onto the detector. The detector is connected to an oscilloscope (DL1740EL) to display the decay of the fluorescence. The excited-state lifetime can therefore be deduced by the fitting of an exponential decay curve, as shown in Figure 7. The quantisation is due to the resolution of the oscilloscope.

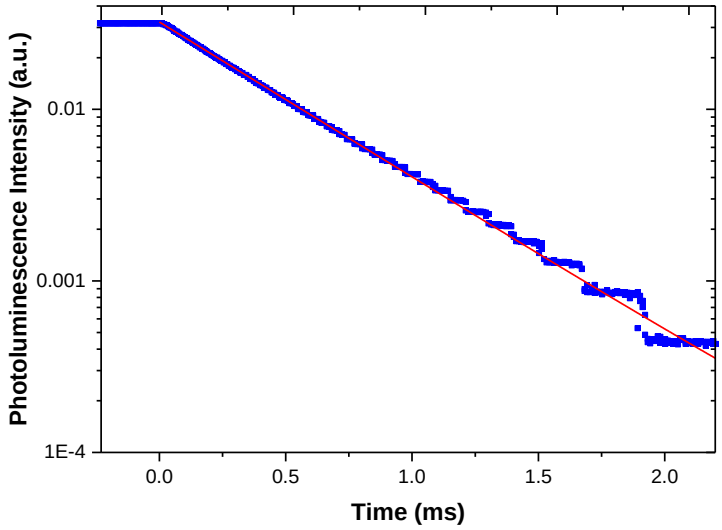

Figure 7: Photoluminescence decay for sample annealed at 650 °C for 12 hrs

To determine the optimum pump wavelength, the photoluminescence power from the sample was collected at different pump wavelengths ranging from 775 to 830 nm. Figure 8 shows the photoluminescence power which has been normalised to incident pump laser power measured after lens 2. As seen, the highest photoluminescence power was attained at a pump wavelength of 795 nm, therefore it was chosen as the pump wavelength. At this pump wavelength, the pump power was 625 mW.

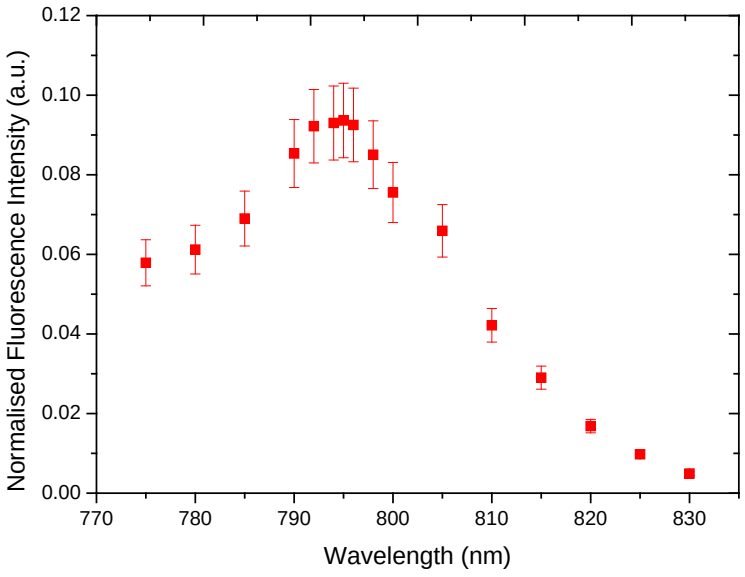

Figure 8: Normalised fluorescence intensity at different pump wavelengths at room temperature

3.3.3 PL and Lifetime Dependence on Annealing Temperature and Duration

The effect of annealing temperature and duration on the 3 wt% Tm:Ta_2O_5 samples were studied. The photoluminescence power and lifetime were characterised for all samples annealed at 500, 550, 600 and 650 °C for 2 and 12 hours. The lifetimes and photoluminescence power vs annealing time and temperature are shown in Figure 9. An increase in lifetime and fluorescence intensity was achieved for higher annealing temperature and longer annealing duration. Annealing improves the stoichiometry and lowers losses in the films, and also reduces the non-radiative defect centres caused during sputtering [58]. The longest lifetime achieved with the sample annealed at 650 °C for 12 hours was 477 µs. The highest photoluminescence power was also achieved with this sample. Therefore longer annealing duration was studied.

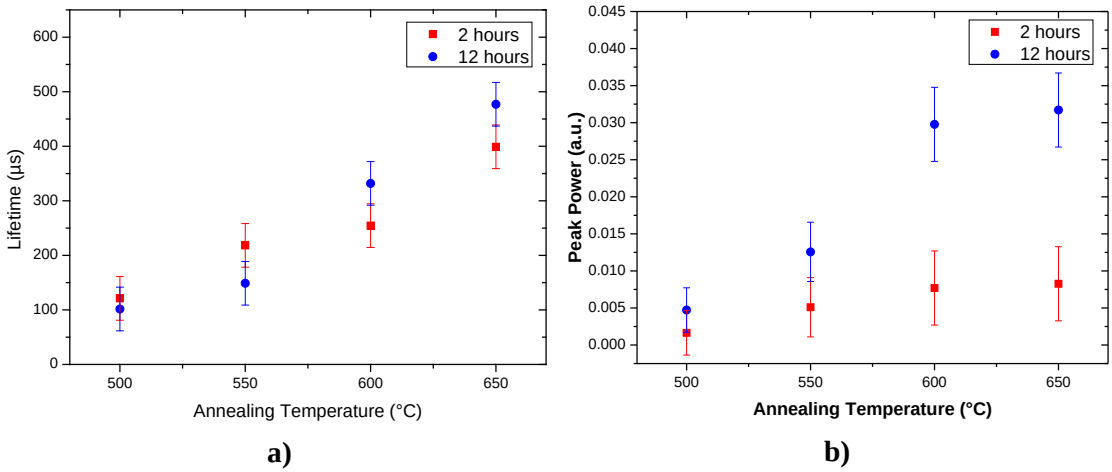

Figure 9: a) Excited-state lifetime and b) photoluminescence peak power for samples annealed at 500, 550, 600, 650 °C for 2 and 12 hours

Further samples were annealed at 650 °C for a duration of 12, 48 and 96 hours. Photoluminescence measurements were taken for these samples to determine the fluorescence intensity and excited-state lifetime. The excited-state lifetime was similar for increasing annealing duration, 477, 462 and 481 µs respectively. On the other hand, there was a large increase in peak photoluminescence power increasing from 48 hrs to 96 hours, as shown in Figure 10. These increases could be due to the removal of some defect centres in the material by annealing in oxygen and therefore reducing the number of non-radiative decay processes and decreasing the rate of relaxation for these processes. However as there was not a large difference in lifetime with annealing duration, 12 hours was chosen as final the annealing duration.

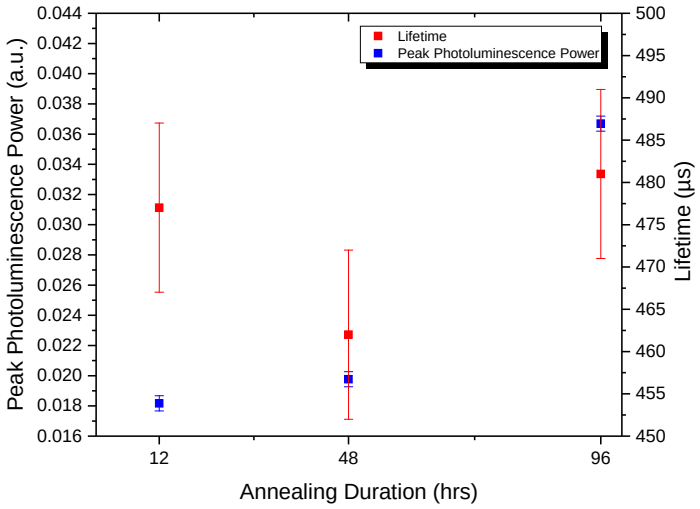

Figure 10: Excited-state lifetime measurement for samples annealed at 650 °C for 12, 48 and 96 hours

In comparison with other thulium-doped materials, the excited-state lifetime is in a similar range with what has been reported for silica fibres with similar dopant concentrations [59]. A shorter lifetime of 250 µs [60] was observed from a high-index nanoparticulate silicon film, but longer lifetime of 2.32 ms was observed in Al_2O_3 [50] and other lower dopant concentration silica fibres [61]. There has been report of similar lifetime of 568 µs with Al_2O_3 [49] and ~650 µs with silica [61]. Silicate fibres have a high phonon energy and multiphonon relaxation leading to lower $^3F_4$ lifetime [62]. The shorter lifetime is due to the higher refractive index of Ta_2O_5 [62].

3.3.4 PL and Lifetime Dependence on Thulium Concentration

2 µm thick 1 and 2 wt% Tm:Ta_2O_5 slab waveguides were deposited and annealed at 650 °C for 12 hours in oxygen atmosphere. They were compared with the previously deposited 3 wt% sample, shown in Figure 11. The highest intensity was obtained with the 3 wt% Tm:Ta_2O_5 sample however it had the shortest lifetime. Although the 3 wt% sample had the shortest lifetime, 3 wt% was chosen due to its highest intensity and concentration in hope to achieve a higher gain.

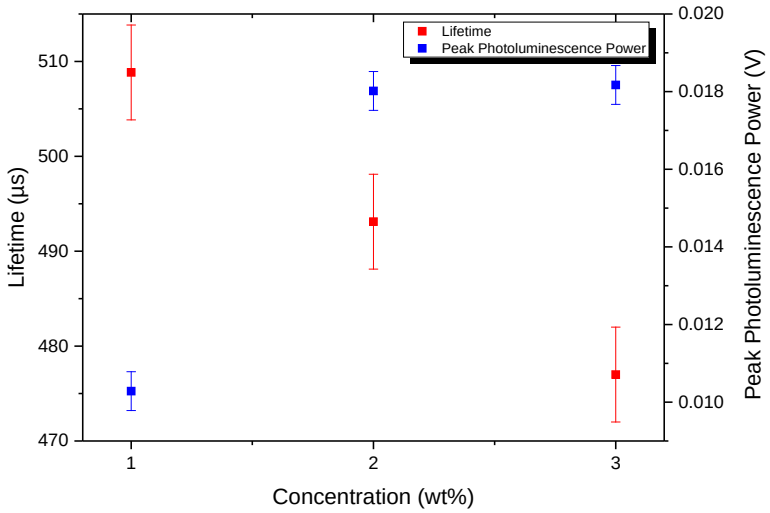

Figure 11: Peak photoluminescence intensity and lifetime for 1, 2 and 3 wt% Tm:Ta_2O_5, annealed for 12 hrs

The shorter lifetime and higher photoluminescence power is due to the increase in the number of rare-earth ions which reduces the distance between the thulium ions and leading to more ion-ion interactions. Ion-ion interaction is a general term describing processes which lead to energy transfer between neighbouring rare-earth ions. This introduces a form of loss mechanism through non-radiative decay, leading to faster photoluminescence decay [63].

3.4 Spectroscopic Measurements of Tm:Ta_2O_5

To provide quantitative data for laser performance, the emission and absorption cross-section, in particular at the pump and lasing wavelength, are characterised.

3.4.1 Emission Spectrum Measurements

A similar setup to the photoluminescence measurement was used for the emission spectrum measurement. For the latter, the collection optics and oscilloscope was replaced with an optical spectrum analyser (OSA – Yokogawa AQ6375) to record the emission spectrum for 2 µm thick samples annealed at 650 °C for 12 hrs, as shown in Figure 12.

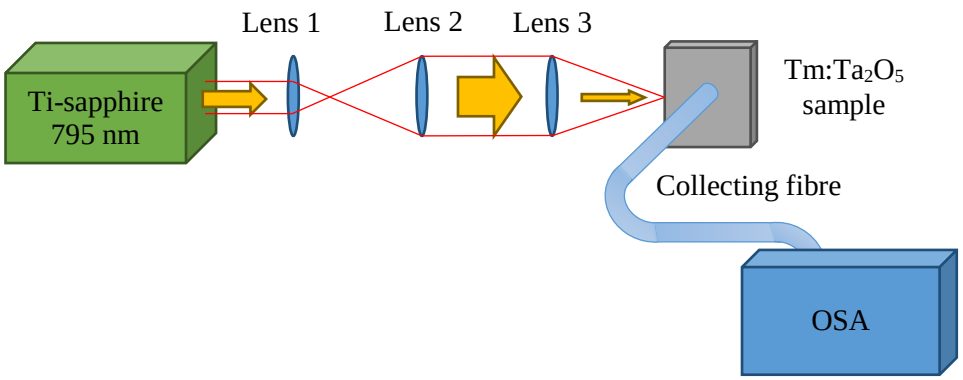

Figure 12: Characterisation apparatus for photoluminescence lifetime measurements

3.4.1.1 Emission Spectrum

To confirm the optimum pump wavelength to achieve emission, emission spectrums were taken at different pump excitation wavelength ranging from 775 to 835 nm on a $Tm:Ta_2O_5$ sample annealed at 650 °C for 12 hrs, shown in Figure 13. A broad peak in photoluminescence ranging from 1600 to 2100 nm and centring around 1850 nm was observed for the $Tm:Ta_2O_5$ slab waveguides. Peak emission was observed when pumped at 795 nm. This corresponds with the maximum photoluminescence power measured with an oscilloscope when pumped at 795 nm, from Figure 8. Fluctuations observed at around 1.9 μm are believed to be due to the strong atmospheric absorption around this wavelength region.

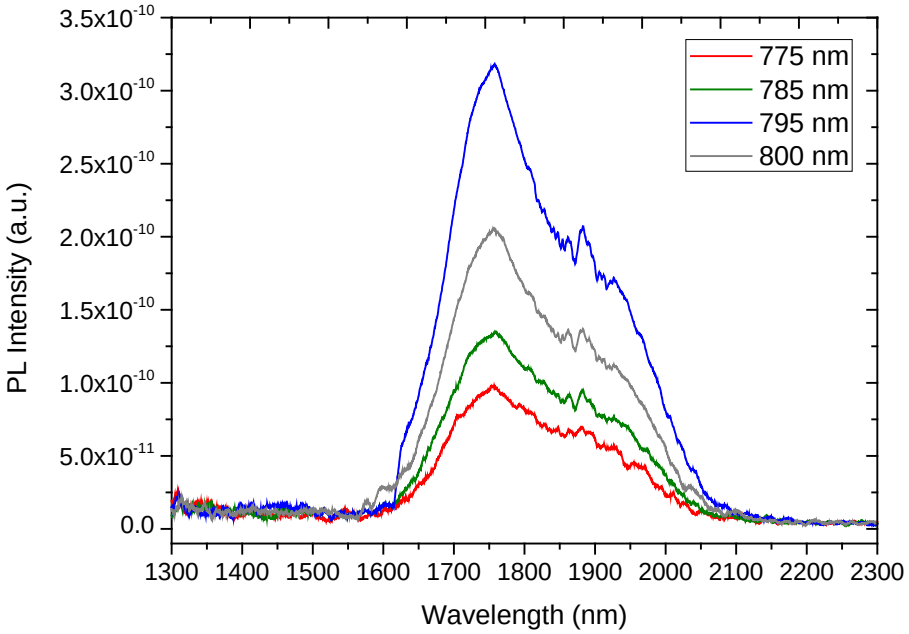

Figure 13: Emission spectrum of $Tm:Ta_2O_5$ when pumped at 775, 780, 795 and 800 nm

A new OSA with better specification was purchased, Thorlabs OSA203C. Emission spectrum measurements were performed again for the sample annealed at 650 °C for

12 hrs. Less fluctuations were observed around 1.9 μm, as seen in Figure 14, this is believed to be due to machine having been purged when purchased.

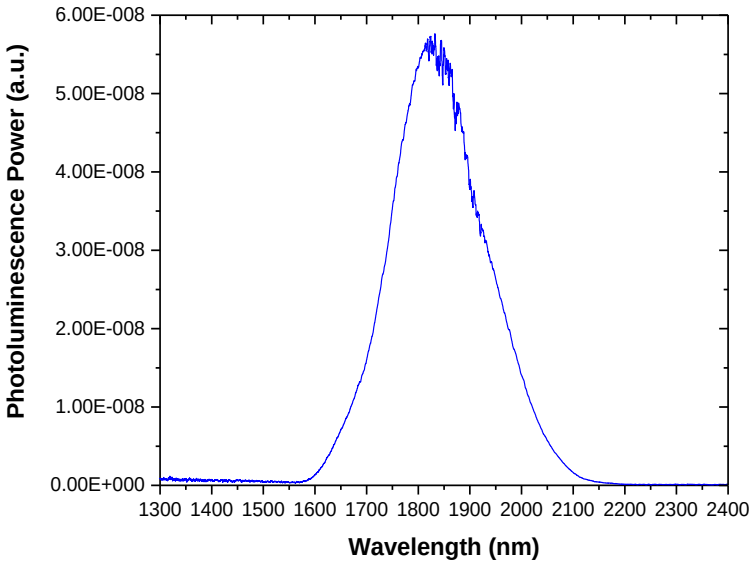

Figure 14: Emission spectrum of Tm:Ta_2O_5 with pump wavelength of 795 nm taken with Thorlabs OSA203C OSA

3.4.1.2 Emission Cross-Section

The probability of a certain emission transition occurring can be quantified by the emission cross-section (σ_{em}). This can be estimated using the Füchtbauer-Ladenburg equation from the measured emission spectrum, as shown in equation 2 [64].

$$\sigma_{em}(\lambda) = \frac{\lambda^5 \eta_q}{8\pi n^2 \tau c} \frac{\beta(JJ')I(\lambda)}{\sum \int \lambda I(\lambda)\, d\lambda} \tag{2}$$

where λ is the peak emission wavelength, η_q is the fluorescence quantum efficiency, $\beta(JJ')$ is the luminescence branching ratio for the $^3F_4$ -> $^3H_6$ transition (which is 1 in this case as there are no other lower energy levels to decay to apart from the ground state), τ is the fluorescence lifetime, n is the refractive index of the medium, $I(\lambda)$ is the emission spectrum. It is derived from the Einstein's relation which can be used to describe spontaneous emission.

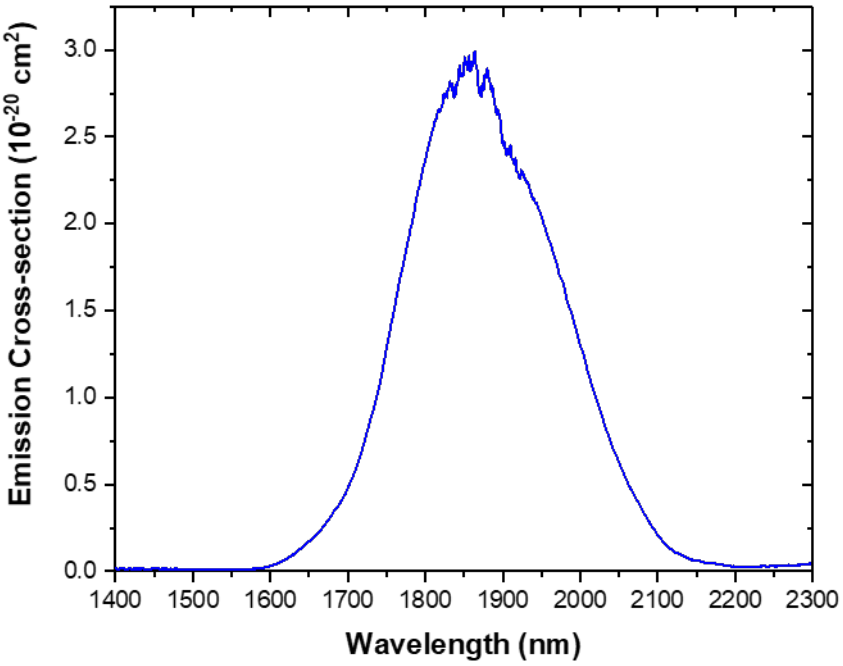

Figure 15: Emission cross-section of Tm:Ta_2O_5 annealed at 650 °C for 12 hours

Using the Füchtbauer-Ladenburg equation, the emission cross-section of a Tm:Ta_2O_5 annealed at 650 °C for 12 hours, shown in Figure 15, was calculated from the emission cross-section in Figure 14. The peak emission cross-section was found to be 2.99×10^{-20} cm^2 at 1863 nm.

There had been investigations into photoluminescence from Tm:Ta_2O_5, where emission at around 800 [51], 650, 1250 and 1550 nm [65] had been observed. We had previously reported first emission of Tm:Ta_2O_5 at around 1800 nm [66]. The emission cross-section is higher than a similarly doped silica fibre 0.36×10^{-20} cm^2 [59], and 0.47×10^{-20} cm^2 from aluminium oxide films (Al_2O_3) with Tm^{3+} concentration of 5×10^{20} ions/cm^3 [50]. Similar reason to the shorter lifetime is Tm:Ta_2O_5, this is due to the higher refractive index of Ta_2O_5 [62] and therefore the waveguide has a better mode confinement ensuring better absorption along the waveguide.

3.4.2 Tm:Ta_2O_5 Rib Waveguide Fabrication

For absorption and lasing measurements Tm:Ta_2O_5 rib waveguides were used. 2 μm thick Tm:Ta_2O_5 films deposited on 4" oxidised silicon wafer were realised into Tm:Ta_2O_5 rib waveguides were realised with by conventional lithography and ion beam milling (as described in section 2.2.3.2 to 2.2.7). This sample had been annealed at 650 °C for 12 hrs. The rib waveguides were etched by 330 nm. An already available chromium photomask with waveguides ranging from 2 to 20 μm was used for photolithography. The samples for absorption measurements were cladded with 2 μm SiO_2 to reduce the propagation loss and prevent damage to the waveguides.

Absorption measurements were performed on a 20 µm wide and 0.7 cm long Tm:Ta_2O_5 rib waveguide. A large rib waveguide geometry ensures better mode confinement, giving a good representation of the material, lower losses due to waveguide sidewalls and longer absorption length. The larger waveguide also improves the coupling efficiency with a single mode and multimode fibre.

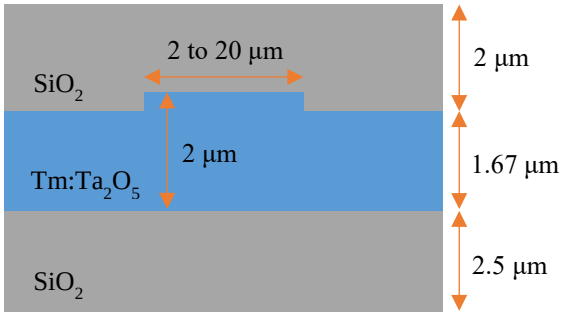

Figure 16: Tm:Ta_2O_5 rib waveguide dimensions

3.4.3 Absorption Spectrum and Cross-section

The absorption measurement was performed using a broadband white light source. The wide operating wavelength range of the white light source allow the absorption measurement of Tm:Ta_2O_5 between 400 to 1800 nm. Light from a tungsten halogen bulb is coupled into a SMF28 fibre and butt coupled into a 20 µm wide waveguide. The transmission was collected with a multimode fibre and recorded with an OSA (Yokogawa AQ6375 - between 600 to 1600 nm). The setup of the absorption measurement is shown in Figure 17.

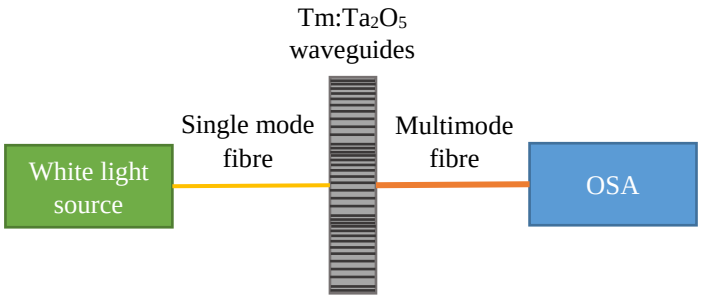

Figure 17: Setup for absorption spectrum measurement

3.4.3.1 Absorption Cross-section

The absorption cross-section (σ_{abs}), quantifying the probability of an absorption transition occurring, was calculated with the Beer Lambert's equation [67] from the absorption spectrum (between 600 and 1600 nm) recorded in the previous section. The

Beer-Lambert law in equation 3 can be rearranged as equation 4 to be in terms of absorbance, how much light have been absorbed by the rare-earth ions. Absorbance is the logarithmic ratio of the initial light intensity, I_o to light intensity after passing through the sample, I. The absorption cross-section can then be determined from the absorbance, Tm concentration of sample, N, and length of sample, L, using equation 4.

$$I = I_0 \exp(-\sigma_{abs} \cdot L \cdot N) \tag{3}$$

$$\text{Absorbance} = \ln\left(\frac{I_0}{I}\right) = -\sigma_{abs} \cdot L \cdot N \tag{4}$$

Due to the high noise floor of the OSA (Yokogawa AQ6375), of around -80 dBm, above 1600 nm, it was not possible to accurately determine the shape of the absorption spectrum beyond this wavelength. Therefore for the absorption cross-section above 1600 nm, it was calculated using McCumber theory [68] from the emission spectrum, using equation 5.

$$\sigma_{abs}(\nu) = \sigma_{em}(\nu) \exp\left(\frac{h\nu - E_{ZL}}{k_B T}\right) \tag{5}$$

where h is Planck's constant, ν is frequency, E_{ZL} is the zero-phonon line (1739 nm [69]), k_B is the Boltzmann constant and T is the temperature. The calculated absorption cross-section at 1600 nm was found to match the absorption cross-section at 1600 nm calculated with the Beer Lambert's equation. The two calculated absorption cross-section spectrum were joined together giving the absorption cross-section spectrum shown in Figure 18. The calculated peak absorption cross-section at 1756 nm was 1.09×10^{-20} cm^2.

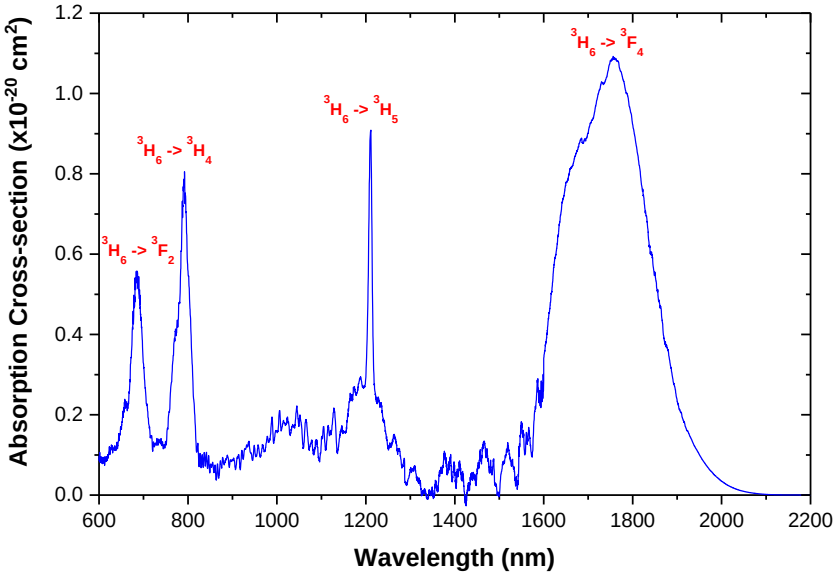

Figure 18: Absorption cross-section spectrum of $Tm:Ta_2O_5$

The reported absorption cross-section on thulium-doped materials have been mainly of thulium-doped silica fibres and bulk glasses. The absorption peaks are in similar position to what have been observed in other host [70]. The absorption cross-section for the $^3H_6 \rightarrow {}^3F_4$ transition is higher than for example silica fibres of 0.42×10^{-20} cm^2 [59] and Al_2O_3 of 0.28×10^{-20} cm^2. However, similar absorption cross-section was reported for $^3H_6 \rightarrow {}^3H_4$ transition with silica fibres [71]. The ratio of the absorption peaks and absorption cross-section are dependent on host material.

3.5 $Tm:Ta_2O_5$ Waveguide Lasers

Waveguide lasers were realised on a $Tm:Ta_2O_5$ thin film on oxidised Si wafer, annealed at 650 °C for 12 hours. Using Soref's equation [72], for a 2 µm high $Tm:Ta_2O_5$ and etched 330 nm, the widest waveguide on the sample for single mode operation is 3 µm. This was chosen as the waveguide for lasing as it provided better mode confinement than narrower waveguides, allowing better overlap of the waveguide mode and the thulium-ions distribution and lower losses due to sidewall roughness. A 3 µm wide rib waveguide was simulated in COMSOL Multiphysics, as shown in Figure 19. The mode diameter at emission wavelength of 1.866 µm was 9.12 µm in x-direction and 2.21 µm in the y-direction, and at the pump wavelength 795 nm the mode diameter was 7.58 µm in x-direction and 1.96 µm in the y-direction. The spot size will be used to determine the pump launch efficiency in section 3.5.2.

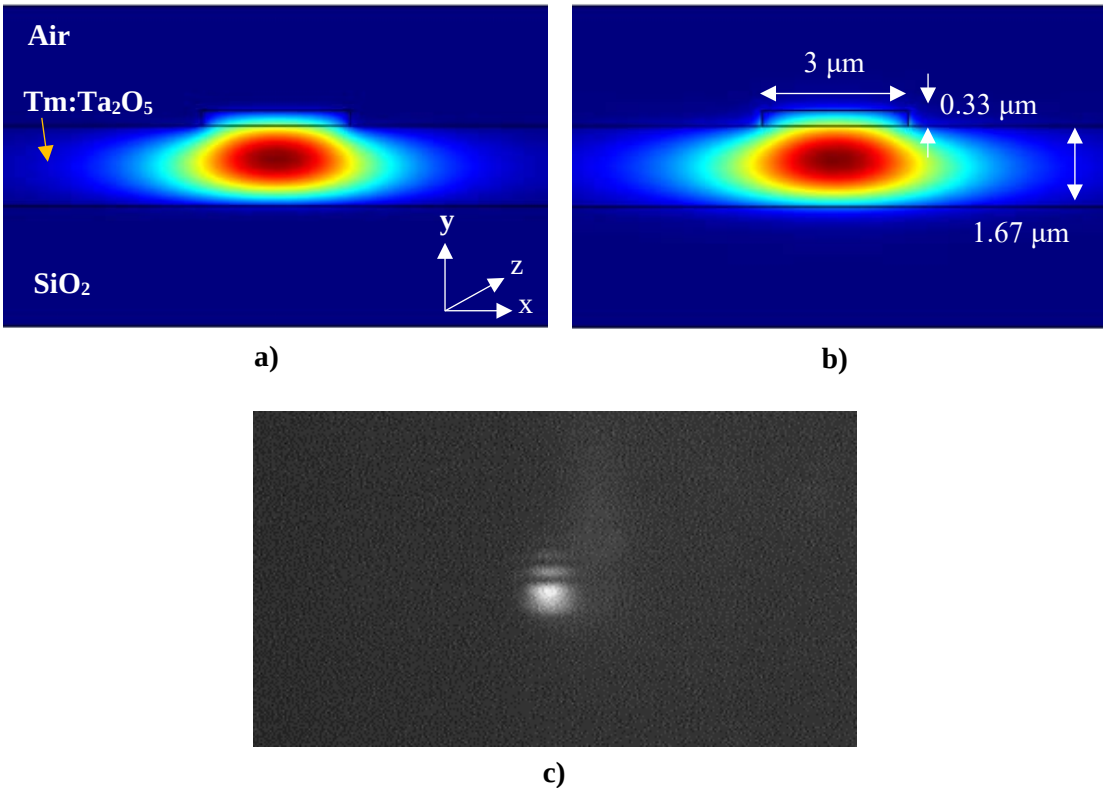

Figure 19: Mode profiles of 3 μm wide $Tm:Ta_2O_5$ rib waveguide at a) 795 nm and b) 1866 nm, and camera image of output from 3 μm wide $Tm:Ta_2O_5$ rib waveguide at 795 nm

3.5.1 Laser Operation

The waveguide lasers can achieve lasing if the cavity gain can overcome the cavity losses. The gain per unit length at position z , G(z),was calculated using equation 6 [42] using the measured emission cross-section (σ_{em}) at signal wavelength and absorption cross-section (σ_{abs}) at pump wavelength, in section 3.4.1.2 and 3.4.3.1 respectively, where N_0 is the total Tm concentration, Γ is the overlap between propagation mode and concentration profile and η_e is the excited-state density. Assuming full inversion and an overlap of 70%, the maximum gain per unit length which can be achieved is 24 dB/cm.

$$G(z)= N_0\Gamma\left[\sigma_{em}\,\eta_e(z)- \sigma_{abs}\left(1- \eta_e(z)\right)\right] \quad (6)$$

Two other parameters are also important in the operation of a laser, pump threshold power and slope efficiency. Threshold pump power (P_{th}) indicates the pump power at which lasing starts to occur. This was calculated with equation 7, where ν_p is the pump frequency, A is the beam area, l_{rt} is the round trip loss, η_p is the pump launch efficiency, τ is the excited-state lifetime and σ_{em} is the emission cross-section.

$$P_{th} = \frac{h\nu_p A l_{rt}}{\eta_p \tau \sigma_{em}} \quad (7)$$

A preliminary theoretical calculation gives a threshold pump power of 8.7 mW guided power. The calculated threshold pump power was lower than reported in literature for similar Tm-doped lasers [13, 73], which is due to the one order of magnitude higher emission cross-section.

Another important property to characterise the laser performance is the slope efficiency. It depicts how efficient the laser is at converting input pump power to lasing output signal. This is defined as the slope of the input pump power vs output power curve. Theoretically the single end slope efficiency (η_{sl}) can be calculated using equation 8 [74].

$$\eta_{sl} = \eta_p \frac{T_1}{\delta_1} \frac{h\nu_s}{h\nu_p} \quad (8)$$

where η_p is the fractional pump power contained in the active region of the laser (assumed 70% in this case), T_1 is the output coupler loss, δ_1 is the total cavity loss, ν_s and ν_p are the signal (λ=1866 nm) and pump (λ=795 nm) frequencies respectively. The silver mirror has a 98.3% reflectivity, therefore the output coupler loss is calculated to be 4.1 dB. The total cavity loss, δ_1, includes the input reflection loss from the polished end-facet (12.6% reflectivity, loss of 0.13), output coupler loss, T_1, and assuming a propagation loss of 2 dB/cm, giving a δ_1 of 6.2 dB.

For the Tm:Ta_2O_5 lasing setup described later in section 3.5.4, where lasing was achieved with one polished end-facet (12.6% reflectivity) and a silver mirror (98.3% reflectivity) at the waveguide output, the slope efficiency was calculated to be 19.6%. This is slightly lower than what has been reported in Tm:Al_2O_3 waveguide [75], however this could be due to the lower reflectivity the polished end-facet or higher losses of the waveguides.

3.5.2 Pump Launch Efficiency

One of the main factors of loss in a waveguide laser system is input coupling into the waveguide. To estimate the absorbed pump power, the pump launch efficiency was calculated by the overlap integral of the mode field of the waveguide and focussed beam with equation 9 [76]. The overlap of the pump beam with the waveguide fundamental mode will give a good estimate of the launched pump power to determine the slope efficiency and threshold pump power of the waveguide laser.

Light from a HI1060 fibre was collimated and focussed into a 3 μm waveguide. There is a loss incurred from the mode mismatch between the focussed beam and the waveguide. The mode field diameter of the HI1060 is 5 μm at 795 nm. This is collimated and focussed into the waveguide by an aspheric lens (C220D-TMB) giving a beam diameter of 1.494 μm.

$$\text{Coupling efficiency, } \eta = \frac{\left[\int_{-\infty}^{\infty}\int_{-\infty}^{\infty} E_b(x, y)E_g(x, y)\,dx\,dy\right]^2}{\int_{-\infty}^{\infty}\int_{-\infty}^{\infty}|E_b(x, y)|^2\,dx\,dy \int_{-\infty}^{\infty}\int_{-\infty}^{\infty}|E_g(x, y)|^2\,dx\,dy} \quad (9)$$

where, $E_b(x, y)$ is the input beam's field profile, $E_g(x, y)$ is the mode's field profile. Equation 9 can be rewritten as equation 10 [77], which gives a relationship of the coupling efficiency in terms of the beam and waveguide modal spot size.

$$\text{Coupling efficiency, } \eta_0 = \frac{4W_b^2 W_x W_y}{(W_b^2 + W_x^2)(W_b^2 + W_y^2)} \quad (10)$$

where, W_b is the input beam's mode radius (assuming a circular mode) of , W_x is the waveguide's mode radius in the x-direction and W_y is the waveguide's mode radius in the y-direction. Using the spot size of the waveguide fundamental mode listed in section 3.5, at 795 nm, a pump launch efficiency of 10% was calculated. The pump launch efficiency can be improved with the use of another input lens.

3.5.3 Lasing from Polished End-Facets

Initial lasing characterisation were performed on the waveguide lasers without mirrors, with just the waveguide polished end-facets to create the laser cavity, using the setup shown in Figure 20. The reflections (R) from the polished end-facets due to Fresnel reflection amounts to ~12% assuming normal incidence and no imperfections, calculated using equation 11 [78], where n_1 is the refractive index of Tm:Ta_2O_5 (~2.1) and n_2 the refractive index of air (1.0).

$$R = \left[\frac{n_1 - n_2}{n_1 + n_2}\right]^2 \quad (11)$$

A different setup to the photoluminescence characterisation was built to characterise the Tm:Ta_2O_5 waveguide lasers. Light from the Ti-sapphire laser was focussed into a HI1060 fibre with an objective lens. The output of the fibre is collimated (F220FC-780) and focused into the waveguide with an aspheric lens (C330TMD-B, f = 3.1mm, AR coating = 650-1050 nm). Another aspheric lens (C330TMD-C, f = 3.1mm, AR coating = 1050-1700 nm) collects the signal from the waveguide which then passes

through a long-pass filter to filter out any wavelength below 1000 nm. The filtered lasing signal was focussed into a 1 mm diameter core SM2000 fibre with an objective lens and recorded with an OSA to produce a lasing spectrum. The apparatus is shown in Figure 20.

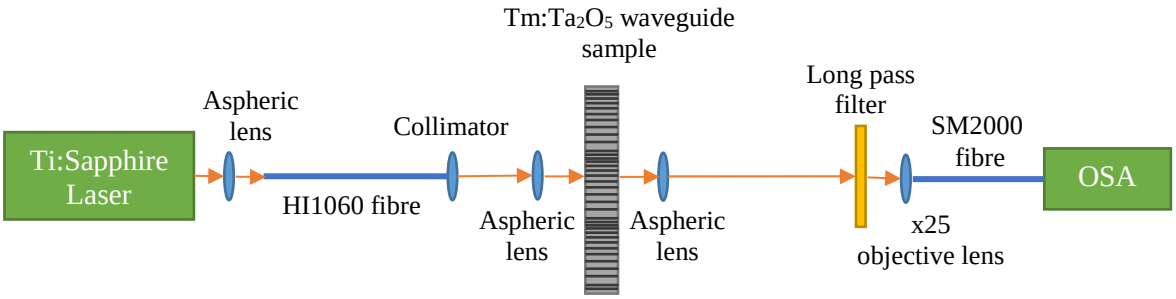

Figure 20: Setup for waveguide laser characterisation

An incident pump power of 170 mW at 795 nm was used. With a 3 µm wide waveguide, lasing was attained at 1238 and 1858 nm, corresponding to $^3H_5 \rightarrow {}^3H_6$ and $^3F_4 \rightarrow {}^3H_6$ transition respectively. The lasing spectrum is shown in Figure 21.

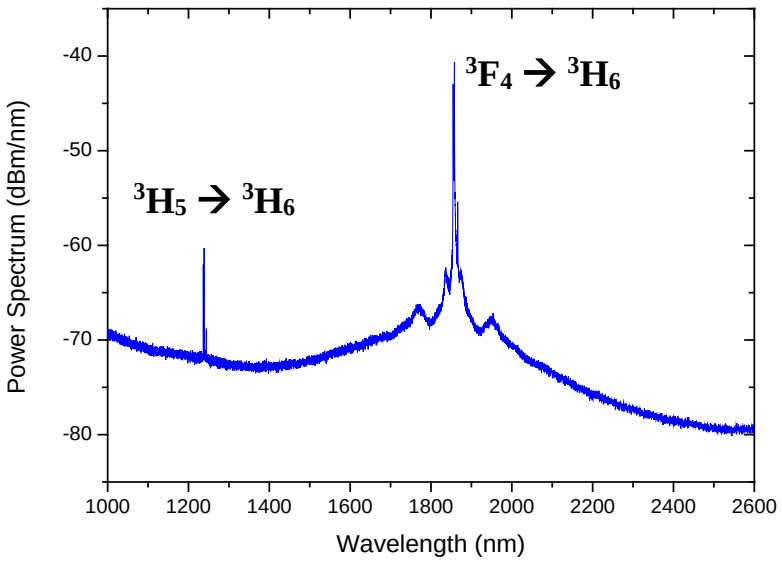

Figure 21: Lasing spectrum showing lasing peaks at 1238 and 1858 nm, at incident pump power of 170 mW at 795 nm pump wavelength

The side lobes seen at the 1858 nm peak are believed to be due to competition of gain between the longitudinal modes within the cavity, as they were more sparse than the free-spectral range of the cavity of 82 pm. The side mode suppression ratio of ~27.5 dB was found at this peak. Lasing was achieved with the waveguide polished end-facets, which suggest it has a gain higher than 9 dB/cm. This corresponds well with the maximum gain per unit length calculated in section 3.5.1.

3.5.4 Lasing with Mirrors

Due to the instability of the laser which could be due to degradation of the waveguides or end-facets, a mirror was added to the output end of the waveguide laser to improve the round trip loss. A silver mirror, with high reflectivity at the pump (95.5%) and lasing (98.3%) wavelength, was butted up against the waveguide output end-facet. With this configuration, the lasing signal will be collected from the end of the waveguide where the pump is inputted. A dichroic mirror (Thorlabs DMSP1180) was therefore added between the collimator and aspheric lens, as shown in Figure 22, to split the lasing signal from the pump signal. The lasing signal is diverted through a long pass filter which filters out anything below 1 μm, so the pump is filtered out. The signal is then focussed into a 1 mm core SM2000 fibre and connected to an OSA to record the lasing spectrum.

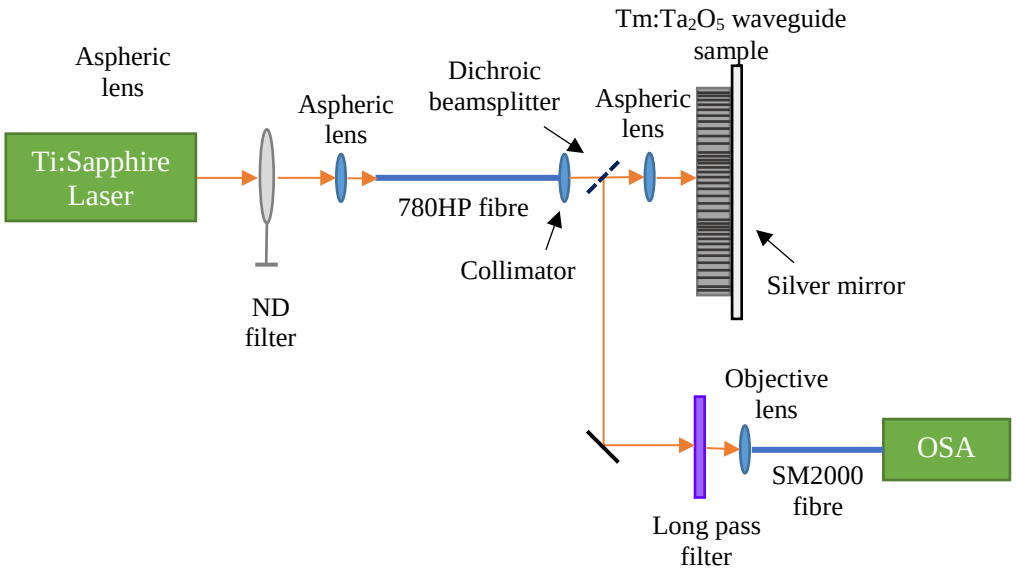

Figure 22: Setup to characterise waveguide laser with mirror at output end-facet

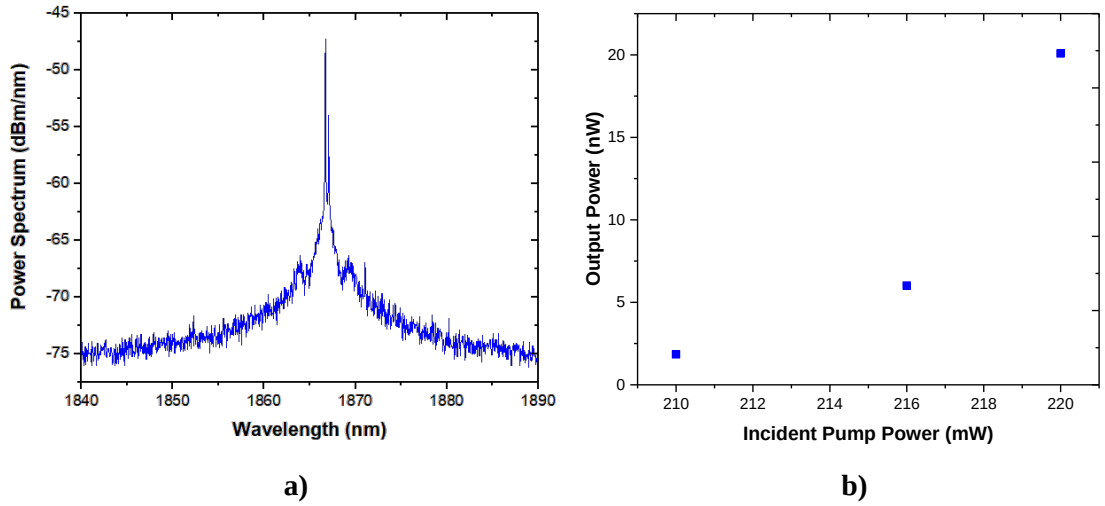

Figure 23: a) Lasing spectrum with incident pump power of 220 mW and b) incident pump power vs output power

Lasing was achieved at 1866 nm, corresponding to the $^3F_4 \rightarrow {}^3H_6$ transition, shown in Figure 23a). This gave an output power of 20.1 nW. An attempt to characterise the threshold pump power and slope efficiency has been performed for incident pump power of 210, 216 and 220 mW, as shown in Figure 23b). Due to some degradation of the waveguide lasers, damaged facets or waveguides, it was not possible obtain further measurements for lower incident pump power. Fabrication of new sample are in progress to characterise the output power at lower incident pump power.

In section 3.5.2, the launch pump efficiency was calculated to be about 10% and with refraction loss of 12.6% from the input facet, the incident pump power used to achieve lasing of 210, 216 and 220 mW, will give an estimated launch pump power of around 18.4, 18.9 and 19.2 mW respectively. This is closer to the theoretical pump power of 8.7 mW guided power calculated in section 3.5.1.

3.6 Conclusion

The first demonstration of a Tm:Ta_2O_5 waveguide laser was shown, lasing at 1866 nm with 20.1 nW output power pumping at 795 nm. The first photoluminescence was also achieved in Tm:Ta_2O_5 thin film waveguides at around 2 µm, pumping at 795 nm, a broad emission centring around 1.85 µm was observed. A lifetime of 477 ± 40 µs and high emission cross-section of 2.99×10^{-20} cm^2 were attained. Rib Tm:Ta_2O_5 waveguides were fabricated for absorption characterisations. Absorption cross-section of 8.05×10^{-21} cm^2 at 792 nm and 1.09×10^{-20} cm^2 at 1756 nm. The high emission and absorption cross-section show that Tm:Ta_2O_5 is a promising material for realising integrated lasers and amplifiers on a Si platform, for telecommunication and sensing applications. To the best of my knowledge, to date there has not been a demonstration of integrated Tm-doped laser sources directly with silicon. The integration of Tm:Ta_2O_5 laser source with a silicon platform has been investigated in the form of a

grating-assisted coupler, to allow the laser signal to be coupled to other devices on the silicon platform which could be on another layer. The grating-assisted coupler has been designed to couple between a Si waveguide and Ta_2O_5 waveguide. This device will be discussed in chapter 5.

Chapter 4 Second-order Nonlinearity in Tantalum Pentoxide

4.1 Introduction

Photonic circuits provide a route to highly functional low-cost optoelectronic and all-optical devices, and are a field of rapid commercial growth. In particular, silicon-on-insulator (SOI) waveguide technology offers high performance with standard wafer processing, for mass-market applications [1]. Recently, dielectric waveguides on silicon have shown enhanced performance for nonlinear processes, particularly due to low two-photon absorption at telecommunications wavelengths and wideband optical transparency [4]. Thin film dielectric waveguides exploit existing silicon process technology and complement SOI waveguides in multilayer silicon photonic circuits or all-dielectric circuits [2]. As in integrated electronics, functionalities such as gain, all-optical and electro-optic switching, feedback and frequency filtering are needed to realise a full range of circuit capability, and dielectric waveguides may complement SOI waveguides in providing these functions. However, amorphous dielectric films do not exhibit the second-order optical nonlinearity required to achieve efficient electro-optic switching, known as the Pockels effect, due to lack of average non-centrosymmetry.

Second-order optical nonlinearity is essential for many optical processes such as electro-optic modulation, second harmonic generation (SHG), sum and difference frequency generation, and optical parametric oscillation. These can be utilised for electro-optic applications, for example optical modulators and switches, to enhance functionalities of a silicon photonics chip. Optical modulators in Si by carrier injection have already been realised, however the speed of the devices are limited at the telecommunications wavelengths due to free-carrier lifetime. Second-order nonlinearity exists in material which have non-centrosymmetric structure. However commonly used CMOS-compatible waveguide material, such as Si, SiO_2 and Si_3N_4, are centrosymmetric and therefore do not exhibit second-order nonlinearity. Therefore inducing second-order nonlinearity in these materials or integration with a second-order nonlinearity material would be favourable. One of the methods to achieve this is to break the centrosymmetry of a material by thermal poling. This chapter investigates a thermally-poled Ta_2O_5 layer to enhance second-order nonlinearity functionalities to a silicon photonics chip.

Second-order nonlinearity naturally exists in crystals with non-centrosymmetric structure and has been induced in glasses by the process of thermal poling [79]. Thermal poling is a well-established process which allows the possibility of creating permanent $\chi^{(2)}$ in a centrosymmetric, isotropic material that originally has zero $\chi^{(2)}$. A centrosymmetric material has points of inversion symmetry within the medium.

Thermal poling breaks this centre-symmetry by applying a DC electric field to a heated sample across the material creating charge dissociation and moving cations through the glass. The sample is then brought back to room temperature to freeze the charges in place, creating a frozen-in electric field. This frozen-in electric field, E_f, then acts upon the third-order susceptibility ($\chi^{(3)}$) inherent in the material to create an effective second-order susceptibility, $\chi^{eff(2)}$, through $\chi^{eff(2)} = 3E_f \chi^{(3)}$. Clearly, to achieve high $\chi^{eff(2)}$ a material must demonstrate a combination of high $\chi^{(3)}$ and the ability to sustain a high frozen-in electric field, which relates in a first approximation to a high dielectric breakdown strength.

Silicon nitride (Si_3N_4), aluminium oxide (Al_2O_3) and tantalum pentoxide (Ta_2O_5) are three leading candidates for integration of dielectric waveguides on silicon, due to their silicon process compatibility and high refractive index, leading to potential for compact devices. High $\chi^{(3)}$ without two-photon absorption has been exploited in Si_3N_4 and Ta_2O_5 waveguides [4, 5] and gain or lasing from rare-earth doping has been demonstrated in Al_2O_3 [75, 80] and Ta_2O_5 waveguides [8, 9]. Recently, higher values of $\chi^{(3)}$ [81, 82] and extremely low losses [83] have been demonstrated in Ta_2O_5 waveguides, when compared with Si_3N_4 waveguides, rendering them competitive among these thin-film materials. To date, demonstrations of induced $\chi^{(2)}$ in these materials have been limited to Si_3N_4 thin films, where 5 pm/V has recently been achieved on an unpoled, silicon-rich sample [84]. The high $\chi^{(3)}$ of Ta_2O_5 combined with comparable electrical breakdown strength and its use as a highly insulating high-k gate dielectric in CMOS transistors [85] offers the promise of Ta_2O_5 poled waveguides exhibiting higher electro-optic coefficients than those demonstrated to date in other amorphous materials. Furthermore, while $LiNbO_3$ and Si_3N_4 only transmit up to wavelengths of about 5 µm, heavy metal oxide (HMO) such as Ta_2O_5 transmit light at wavelengths up to about 8 µm [14], opening up opportunities for switchable and tunable devices in the mid-infrared.

While Ta_2O_5 appears to be a promising candidate for thermal poling, process conditions for poling and the resultant second-order nonlinearity have yet to be established. In this chapter, a quantitative study of induced $\chi^{(2)}$ in thermally poled sodium-doped and undoped Ta_2O_5 thin films deposited on borosilicate glass substrates, both as-deposited and annealed, is reported. The second-order nonlinearity in SiO_2 by thermal poling was caused by the reorganisation of impurities in particular sodium ions. To achieve a similar effect with Ta_2O_5, Ta_2O_5 doped with 0.75 wt% of Na_2O was investigated. The Na_2O concentration of the Na:Ta_2O_5 target was decided from previous knowledge of thermal poling of Nb_2O_5-containing glass thin films, achieving a high $\chi^{(2)}$, around 3 pm/V [86]. The concentration chosen matches with that of the Borofloat 33 substrate to ensure a similar conductivity for the film and the substrate. The stability of the second-order nonlinearity response was also investigated over more than 1300 hours for all samples. The influence of sodium doping and annealing of Ta_2O_5 thin films on the poling-induced $\chi^{(2)}$ and stability is discussed. Some of the material in this chapter has been publication [87].

This project is a collaboration with Prof. Marc Dussauze and Dr. Flavie Bondu from the University of Bordeaux. The fabrication and characterisation of the films were carried out at the University of Southampton. They were then sent to the University of Bordeaux to be thermally poled and the work performed there are discussed in section 4.4.

4.1.1 Second-order Nonlinearity Materials

There are several poling methods demonstrated to induce second-order nonlinearity, such as corona poling, optical poling and ultraviolet (UV) poling. Compared with other poling process like corona poling and UV poling, thermal poling have shown more reliable results [88]. Other methods reported to induce second-order report include straining the material [89] and providing a multilayer structure [90, 91].

Towards this end, bulk glass systems with high third-order nonlinearity such as niobates [92], tellurites [93, 94], or germinates [95] for oxides and also arsenic or germanate sulphide for chalcogenide compositions, have been explored. To date, promising results have been obtained for heavy metal oxide systems with stable $\chi^{(2)}$ values reported in the range 1-10 pm/V [92] and also for poling of chalcogenides, though the latter have issues in the stability of the induced nonlinearity [96, 97, 98, 99, 100].

The literature on poled amorphous thin films is less abundant and mainly focuses on various kinds of silica film [101, 102, 103] with additional reports on heavy metal oxide systems [86]. These studies have demonstrated the possibility of transferring the poling process from bulk to thin film forms. Finally, examples of electro-optical devices [104, 105] or frequency convertors based on thermally poled glasses have also been demonstrated [106]. On SiO_2 films, Fage-Pedersen et al. [107, 108] have obtained the best frequency conversion performance with a normalized conversion efficiency of $1.4x10^{-3}$ %/W/cm^2 using periodic electrodes to obtain a high periodic contrast of the inbuilt static field. The effective second order optical response in this device was $\chi^{eff(2)} = 0.13$ pm/V which is comparable to the efficiency observed in a similar bulk glass. Nevertheless, up to now, practical applications of thermally poled glassy materials have been limited, mainly due to their unfavourable comparison with the very high second-order optical coefficients exhibited by ferroelectric crystals such as $LiNbO_3$ (~27 pm/V [109]).

4.1.1.1 Lithium Niobate

Second-order nonlinearity exists naturally only in centrosymmetric materials. The most commonly used material for modulators is lithium niobate ($LiNbO_3$). Lithium niobate is well known for its high second-order nonlinearity and its electro-optic applications such as modulators. High speed modulators on a silicon platform is an ongoing research area, and one solution that has been investigated to integrate lithium niobate on silicon [110]. However lithium niobate is not a CMOS compatible material,

therefore the integration on silicon is not straightforward. Fabrication of lithium niobate waveguides requires a diffusion, implantation or annealed proton-exchange step [111], which is not compatible with the CMOS foundries. Therefore lithium niobate requires to be bonded onto silicon platforms, which is an expensive and inconvenient process.

4.1.1.2 Tantalum Pentoxide

Tantalum pentoxide (Ta_2O_5) is a suitable material for integration with silicon photonic devices as it is CMOS compatible and already a widely used material in the microelectronics industry like for gate dielectric. Its high index contrast between the core and silica cladding allow the realisation of tight bends and therefore compact circuits. Ta_2O_5 has a high third-order nonlinearity making it a promising material for attaining high second-order nonlinearity by thermal poling. It has a nonlinear refractive index of 72.3×10^{-20} m^2/W at 800 nm [5], which is around 30 times larger than that of silica, 2.36×10^{-20} m^2/W [6], one of common material investigated for thermal poling. Therefore in principle, Ta_2O_5 should produce a $\chi^{(2)}$ around 30 times higher than that already achieved with silica, which is ~1 pm/V, rendering it potentially competitive with $LiNbO_3$.

There have been some investigations of Ta_2O_5 as a medium to achieve second-order nonlinearity. Second-harmonic generation has been reported with an Ag and Ta_2O_5 multilayer structure [90]. The integration of lithium niobate and Ta_2O_5 on a Si platform has been investigated by Rabiei et al. [112]. It utilises high nonlinearity of lithium niobate and also the CMOS compatible Ta_2O_5 as waveguides to avoid the processing of the $LiNbO_3$ layer. No devices have yet to be realised with this material configuration. However both these methods require multiple complex fabrication steps.

4.1.2 Thermal Poling

Thermal poling is commonly done to attain $\chi^{(2)}$ in bulk glass. Myers et al. [113] in 1991 was the first to observe a second order nonlinearity of 1 pm/V in bulk fused silica by thermal poling. This was achieved by poling at temperatures between 250 to 325 °C and applying an electric field of $\sim 5 \times 10^6$ V/m. This work has led investigation of poling in other glasses and thin films to achieve higher $\chi^{(2)}$.

There are several factors which may affect the magnitude of induced $\chi^{(2)}$ by thermal poling. In addition to a high $\chi^{(3)}$, a large built-in field is also important in achieving a high $\chi^{(2)}$ but it also has to be concentrated in a layer a few micron thick beneath the anode [92]. One method to overcome this is by depositing a thin film with a higher resistivity than the substrate, to reduce electronic conductivity and therefore achieving a higher built-in field [114]. Other factors include the cation's mobility and concentration, electronic conductivity, material breakdown strength and poling conditions [99].

4.1.2.1 Thermal Poling Mechanism

Thermal poling breaks the centre-symmetry of a material by creating a negatively charged depletion region. The material used for poling contains impurities, commonly sodium (Na), applying a strong electric field and heat leads to the movement of these sodium ions. Firstly, the sample is heated to increase the mobility of the ions and then a potential is applied. This causes the positive sodium ions to migrate towards the cathode [115]. The ions leave behind a negatively charged depletion region under the anode. Finally the sample is cooled to room temperature and the electric field is then removed. This causes a space-charge region to be maintained after the removal of the applied field, as shown in Figure 24. This charge distribution creates a built-in field, inducing $\chi^{(2)}$. Two possible theories for the creation of second-order nonlinearity by thermal poling are discussed in [116]. Firstly the frozen-in field leading to (direct current) DC electronic polarisation and secondly, due to the orientation of the dipoles.

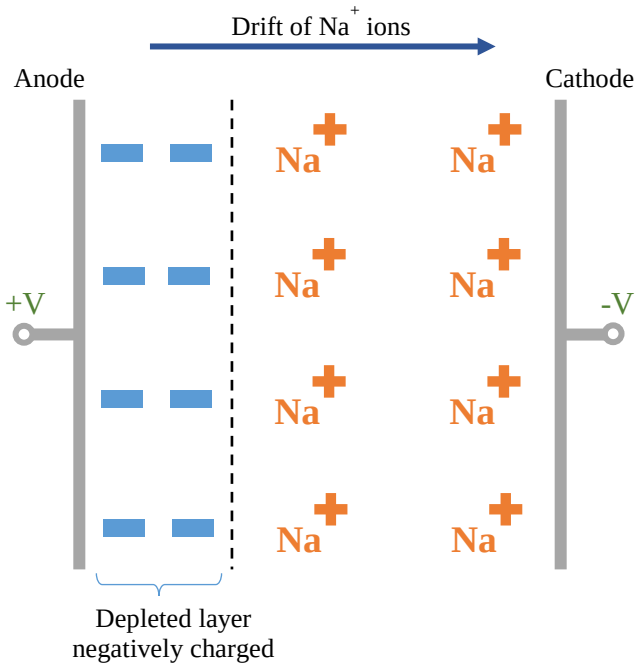

Figure 24: Mechanism of thermal poling

4.2 Fabrication

Thermal poling was performed on 4 µm thick Ta_2O_5 and Na:Ta_2O_5 thin films on Borofloat 33 substrates. The thickness has been reported for similar thermally-poled thin film [86]. Na:Ta_2O_5 samples were used for comparisons with the Na-doped samples to investigate the effect of Na-doping on induced second-order nonlinearity. These thin films were deposited with RF sputtering as described in general in chapter 1. The specific fabrication process for Na:Ta_2O_5 is detailed in this section, starting from cleaning of the substrates, followed by sputtering of the films and finally annealing of the films.

4.2.1 Cleaning Process

The Borofloat 33 substrates were bought as 50 x 50 mm slides. They were cut with a dicing saw to 10 x 20 mm. Before deposition, the substrates were cleaned to ensure good adhesion of the deposited films to the substrate. Firstly, substrates were solvent cleaned in an ultrasonic bath to remove any particles on the surface of the substrate by high frequency waves agitating the solvent. Next, a piranha clean removes any remaining organic residues and metal contamination with its strong oxidising nature. And finally the substrates were placed in fuming nitric acid to remove any organic material that had not been removed by the piranha clean.

The cleaning process of the Borofloat 33 substrates were as follows:

1. Samples are placed in a beaker filled with acetone and placed into an ultrasonic bath for 20 mins.
2. They are removed and placed into an isopropanol (IPA)-filled beaker and put into the ultrasonic bath for another 20 mins.
3. The samples were then rinsed with deionised (DI) water and dried with nitrogen gun.
4. This was followed by a piranha clean, 3:1 ratio of sulphuric acid (H_2SO_4) and hydrogen peroxide (H_2O_2) respectively.
5. They are left in the solution for 20 mins, then taken out and thoroughly washed with DI water and dried with nitrogen gun.
6. They are put into a beaker filled with fuming nitric acid and left for 5 mins, followed by rinsing in DI water and dried with nitrogen gun.
7. Lastly, after checking the substrates were clean under the microscope, they were left overnight in a 120°C oven to remove all the moisture.

4.2.2 Sputtering

Thin films were deposited from 6” diameter powder-pressed targets of Ta_2O_5 or 0.75 wt% Na_2O-doped Ta_2O_5 were deposited on Borofloat substrate using RF sputtering, under the same conditions listed in section 2.2.1. The first deposition was performed on a microscope slide sample to establish the deposition rate. From the known deposition time and measured thickness of film, the deposition rate was calculated to be 2.33 nm/min. This is a little slower than the deposition rate of pure Ta_2O_5 reported in section 2.2.1, however this is due to the deposition performed with an older magnetron which provides less RF power for the $Na:Ta_2O_5$ samples.

4.2.3 Annealing

After deposition, half of the samples were annealed, however with a different annealing temperature and duration than described in section 2.2.2. This is due to the manufacturer’s recommended maximum operating temperature for the substrate (Borofloat 33) as 500 °C for short-term usage less than 10 hours [117]. Therefore 500 °C was chosen as be the annealing temperature for the $Na:Ta_2O_5$ films. Undoped Ta_2O_5 were normally annealed at 600 °C for 2 hours. Therefore to compensate for a

lower annealing temperature, a longer anneal of 3 hour was performed on the Na:Ta_2O_5. For the undoped Ta_2O_5 samples, annealing was also performed at 500 °C for 3 hours.

4.3 Characterisation

After fabrication, the films are characterised for their thickness, refractive index and crystallinity.

4.3.1 Thickness Measurements

The thickness of the deposited films were measured using the KLA Tencor P16 stylus profiler. Before the deposition of the film, Kapton tape was applied to a small corner of the substrate. The tape was removed after deposition leaving an area of the substrate with no film. By scanning the sample with a 2 µm diameter stylus, the surface profile is created from the vertical displacement of the stylus during the scan. This allows the film thickness to be determined.

The film thickness measured was found to be 4 µm ±10 %. Overall, the film uniformity across each sample is approximately 4.5 %, this is based on five measurements along the length of the sample. It is around the film uniformity expected from the sputtering machine used, which is 5 %.

4.3.2 Refractive Index Measurements

The refractive indices of the films were measured using an ellipsometer (J.A. Woollam M-2000) at wavelengths between 500 and 1600 nm. The ellipsometry measurements of refractive index for the undoped and Na-doped, annealed and unannealed Ta_2O_5 films are shown in Figure 25.

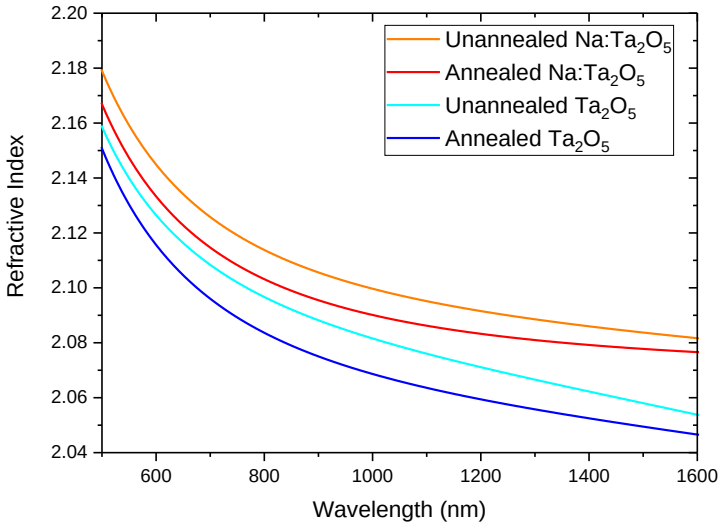

Figure 25: Dispersion curves of refractive indices of annealed and unannealed Na-doped Ta_2O_5 films and annealed and unannealed undoped Ta_2O_5 films, obtained by ellipsometry

Figure 25 shows that the refractive index of the Na-doped films is higher than that of the undoped films for both annealed and unannealed samples, as also seen in glasses [118]. The annealed films showed lower refractive index than the unannealed films, due to the replenishment of oxygen vacancies in material during annealing, as observed previously [20].

Maker fringe measurements, described in section 4.4.3.2, are performed with a pump wavelength of 1550 nm and a second harmonic wavelength of 775 nm, so the refractive index values at these wavelengths extracted from the data in Figure 25 are used for the Maker fringe calculations are given in Table 5 below.

Table 5: Refractive indices of Ta_2O_5 films at the Maker fringe wavelengths

	1550 nm	**775 nm**
Unannealed Na:Ta_2O_5	2.083	2.116
Annealed Na:Ta_2O_5	2.077	2.106
Unannealed Ta_2O_5	2.056	2.099
Annealed Ta_2O_5	2.048	2.086

4.3.3 Crystallinity

To identify the effect of incorporating sodium ions in Ta_2O_5 on the crystallinity of the thin films, x-ray power diffraction (XRD) measurement was used to identify the crystallinity of the film. It was used to determine any change to the crystalline structure due to the addition of sodium in Ta_2O_5 and also annealing. These measurements were taken with the help of Dr. Vinita Mittal. XRD measurements were taken on annealed (500 °C) and unannealed Na:Ta_2O_5 and Ta_2O_5 samples on Si wafer. The results showed that both the films were amorphous.

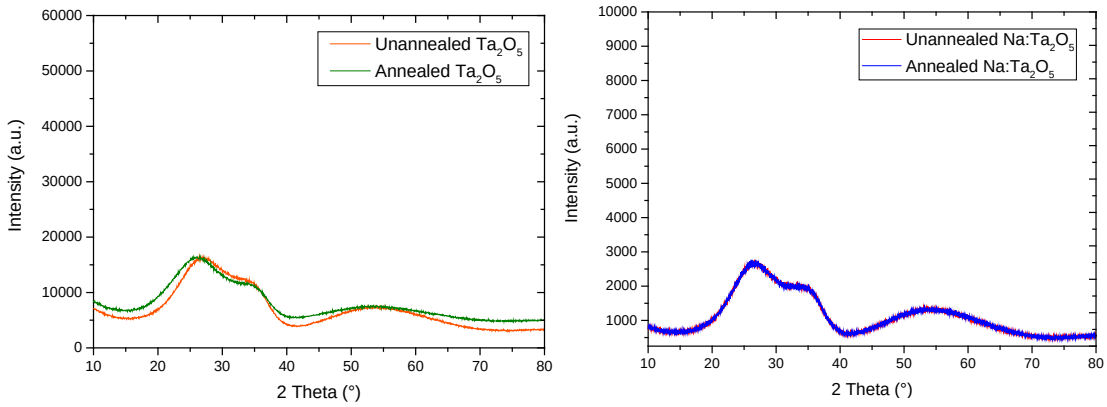

a) b)

Figure 26: XRD diffraction pattern of unannealed and annealed a) Ta_2O_5 and b) Na:Ta_2O_5 thin films

4.4 Thermal Poling

After annealing of the deposited samples, they were sent to University of Bordeaux to be thermally poled for characterisation of their SHG. This section will outline the thermal poling process and characterisation of the $\chi^{(2)}$ performed at the University of Bordeaux.

4.4.1 Thermal Poling Process

The electrodes used for thermal poling are made of a 100 nm indium tin oxide (ITO) layer deposited on microscope glass slide. Thermal poling was performed in an inert atmosphere (flow of N_2) to provide blocking anode conditions avoiding protonic injection. The sample was first placed on the heating plate and heated to 300 °C. Once the temperature has stabilised at that temperature, either a 1.3 or 2 kV electric potential (ramp time of 2 mins) is applied across the anode and cathode, causing the sodium ions to be mobile. The current is monitored during the whole poling process, tracking the movement of the sodium ions, as shown in Figure 27. When the current has dropped to zero, there are no more charges moving suggesting a poled region was formed. The heating plate is then turned off and the sample is left to cool. The whole poling process takes approximately 1800 s. The electric field was removed when the sample was cooled down to room temperature. A region depleted of sodium ions was created, leading to a built-in field near the anode. This maximum built-in field is limited by the breakdown strength of the material [114].

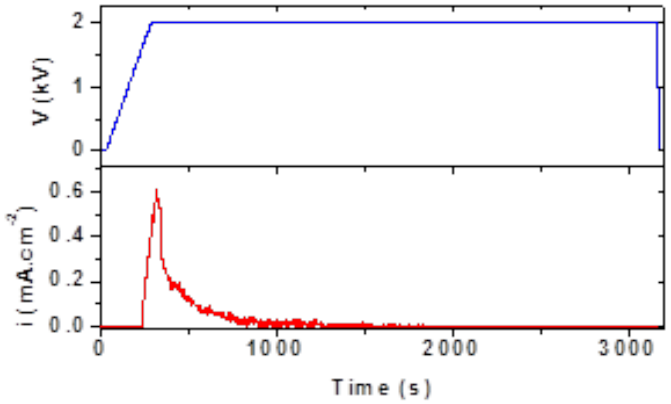

Figure 27: Monitored applied electric field (V) and current (i) through thermal poling process

4.4.2 Depth Distribution of Second-order Nonlinearity Layer

To optimise thermal poling of thin film materials, the first objective is to localise the poling effects within the film, with limited penetration into the substrate. The thickness of the polarised layer depends on both the conductivity properties of the materials (cationic mobility, electronic conductivity) and the poling conditions (temperature, voltage and atmosphere). The influence of applied voltage upon the thickness of the

polarised layer was studied by measuring SHG profiles over the cross section of the poled thin film and substrate.

Micro-SHG measurements were recorded in backscattering mode from a cut cross-section of the poled region using a confocal microscope, in order to determine the spatial distribution of the second-order nonlinearity through the film and substrate. A picosecond laser operating at 1064 nm with a classical linear polarisation was focussed and scanned across the top of the sample. Both 1064 nm excitation and second harmonic collection were through a 50× microscope objective lens with a numerical aperture of 0.5. The in-plane spatial resolution is estimated to be 1.5 µm.

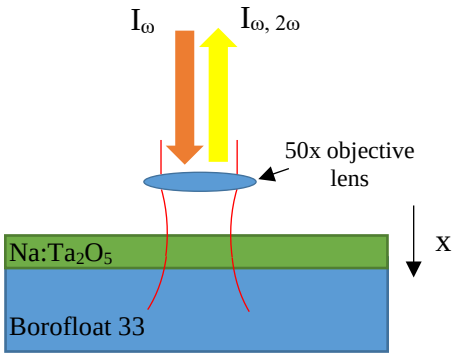

Figure 28: Micro-SHG experimental setup

Two identical 4 µm thick unannealed Na-doped Ta_2O_5 films deposited on borosilicate glass were poled by applying an electric field of 1.3 kV to one and 2.0 kV to the other. Figure 29 shows the SHG profiles of the poled samples changing as it gets from the air, into then thin film and the substrate. The nonlinear optical (NLO) layer is well confined within the Ta_2O_5 film for an applied voltage of 1.3 kV whereas the use of a higher electric field (2.0 kV) extends the NLO layer into the substrate. Some SHG is detected in the air which is unexpected, but this is due to the 1 µm resolution of the equipment. Taking into account the spatial resolution of the SHG measurement, the polarised layer thickness is estimated to be 4 and 6 µm for a poling voltage of 1.3 and 2.0 kV, respectively. This preliminary optimisation demonstrates that the NLO layer localisation can be tuned to be adapted to the film thickness by adjusting the applied voltage.

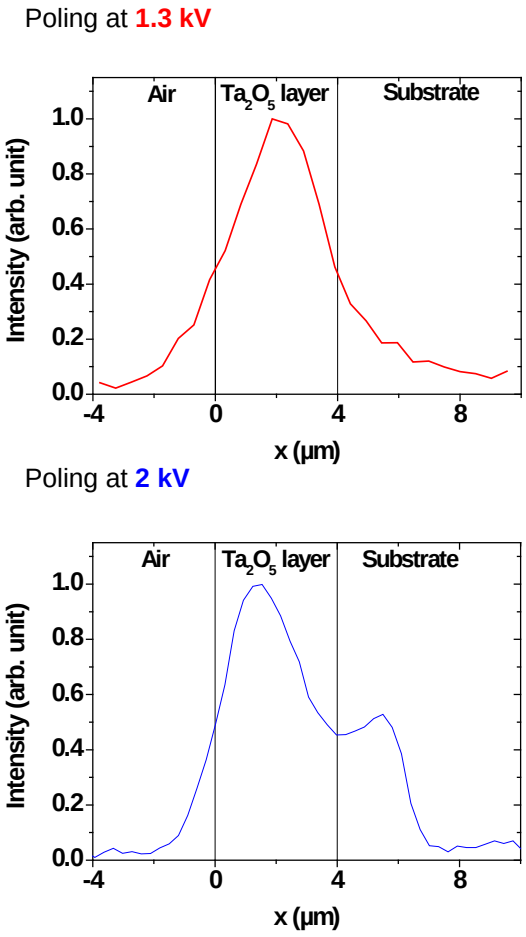

Figure 29: SHG profiles, of Na:Ta_2O_5 amorphous thin films on borosilicate substrate poled at 1.3 kV and 2.0 kV

For the remainder of this study, the applied voltage was fixed at 1.3 kV, allowing the effect of any induced second-order nonlinearity in the substrate to be neglected, simplifying the quantification of the efficiency and stability of second-order optical responses of the poled Ta_2O_5 thin films themselves.

4.4.2.1 XPS Measurements on Poled Samples

Initially to determine the composition of the Na:Ta_2O_5 thin films, measurements were performed on the samples using energy-dispersive x-ray spectroscopy (EDX), with the help of Dr. Vinita Mittal. It is an X-ray analysis technique to determine the chemical and elemental composition of a sample. However, due to the concentration of sodium in the film is below the detection limit of EDX of 1 wt%, another method of measurement is needed to confirm the concentration.

XPS (x-ray photoelectron spectroscopy) was performed to understand the effect of thermal poling on the formation of the polarised layer. Depth profiling was performed to map the Na ions distribution throughout the sample, to distinguish the depletion region, as shown in Figure 30. This is done by focussing an ion beam on an area of the sample, removing material from that area. The concentration of Na, Ta_2O_5 and Si were monitored as the sample was etched.

The cathode and anode were placed on the bottom and top of the sample respectively during poling. Therefore when a field and temperature is applied across the sample, the positively charged sodium ions are attracted to the negatively charged cathode. So it is expected that the region near the top of the film should be depleted of sodium ions. This was confirmed by the XPS results, where there was fewer sodium ions present near the surface of the annealed poled Na:Ta_2O_5 sample, whereas closer to the substrate, the Na concentration increases. At the film and substrate interface around 4 μm, concentration of Si was detected and a drop in Ta_2O_5 concentration. It is unexpected to see Ta_2O_5 in the substrate, however this is believed to be due to redeposition of Ta_2O_5 during the etching process. This could be also the reason for low Si concentration detected in the substrate.

The results of the XPS results correlates well with the Na concentration profile from other poled materials [92].

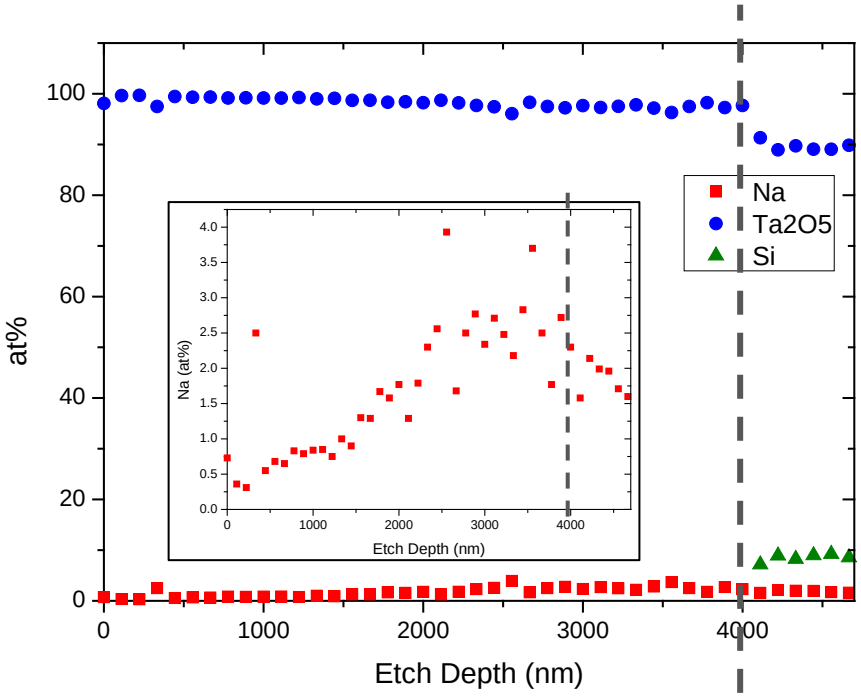

Figure 30: XPS depth profile measurement of 4 μm annealed Na:Ta_2O_5, poled at 1.3 kV and zoomed-in Na concentration (insert), dotted lines mark the film/substrate interface

4.4.3 Second-order Nonlinearity in Ta_2O_5

The second-order nonlinearity induced in the 4 μm thick thermally poled annealed and unannealed, and Na-doped and undoped Ta_2O_5 thin films were measured using the Maker fringe technique.

4.4.3.1 Maker Fringe Experiment

Maker fringe analysis is the conventional method to determine the $\chi^{(2)}$ of a film by measuring the second-harmonic generated by the sample. In the sample, the fundamental signal in the sample do not travel at the same velocity as the second-harmonic signal due to the refractive index dispersion of the material. As the sample is rotated and irradiated with a pump laser beam, with frequency ω, the coherence length is varied at the different position and thus causing the generated second-order harmonic signal, with frequency 2ω, to constructively or destructively interfere forming interference fringes. By fitting these Maker fringes to a theoretical model, such as quartz, the second-order nonlinearity can be characterised.

Maker fringe analysis was performed on four different Ta_2O_5 films (annealed and unannealed, with and without Na doping) of 4 μm thickness, poled at 1.3 kV at 300 °C for 30 minutes. The induced $\chi^{(2)}$ value was determined immediately after the thermal poling treatment by a complete Maker fringe analysis using both angular rotation scans and polarisation scans at a fixed angle of incidence.

Maker fringes were measured using a nanosecond laser operating at 1550 nm. For all experiments, a maximum energy of 100 μJ was applied to the sample. The pulse width was about 20 ns and the repetition rate of the laser pulses was 100 Hz. The intensity of the fundamental was monitored for each measurement and the SHG signal was recorded using a photomultiplier and averaged over 64 laser pulses.

4.4.3.2 Maker fringe Measurements and SHG Stability

All four sets of experimental Maker fringe data were fitted to a model based on the optical transfer matrix approach as described in [119], with the refractive indices and the thicknesses of the two layers (substrate and film) taking the values measured above. In fitting the theoretical Maker fringe curves to the experimental data, the hypothesis of an electro-optical origin of the induced $\chi^{(2)}$ linked to a frozen-in static electric field along the z axis direction (perpendicular to the anodic glass surface) has been assumed. This would bring about a $C_{\infty v}$ symmetry with a resultant ratio of $\chi^{(2)}_{33}/\ \chi^{(2)}_{31} = 3$ to describe the second-order optical response of the poled films. The agreement between experimental data and calculation were very good, confirming that the second-order nonlinearity is due to a frozen-in electric field. Based on the fitting procedure, the $\chi^{(2)}$ was found to be 0.46 pm/V for a Na:Ta_2O_5 film and 0.34 pm/V without Na doping, in both cases poled at 1.3 kV and 300 °C. Comparing the measurements obtained just after thermal poling on the four samples it was found that for Na-doped Ta_2O_5 films the effective second-order optical nonlinearity is higher than for undoped thin films. The initial $\chi^{(2)}$ after thermal poling was almost the same whether the samples were annealed or unannealed, for both Na-doped and undoped Ta_2O_5 films.

The stability of the induced $\chi^{(2)}$ was studied for each sample. The SHG intensity was recorded as a function of time after poling. Figure 31a) shows the results from 0 to 50 hours and Figure 31b) shows the results for the full 3000 hours. The lines fitted to the data in Figure 31b) are based on a stretched exponential function [120] shown in equation 12, which is a classical mathematical expression often used to describe relaxation phenomena in glassy materials, where t_0 is a delay if the beginning of the experiments is not perfectly defined, τ is the relaxation time, A is the initial magnitude of the SHG signal and β is the exponential power for which a departure from 1 (corresponding to a pure monoexponential behaviour) indicates a broadening of the relaxation time distribution.

$$I_{2\omega}(t)=A\exp\left(-\frac{t-t_0}{\tau}\right)^{\beta} \qquad (12)$$

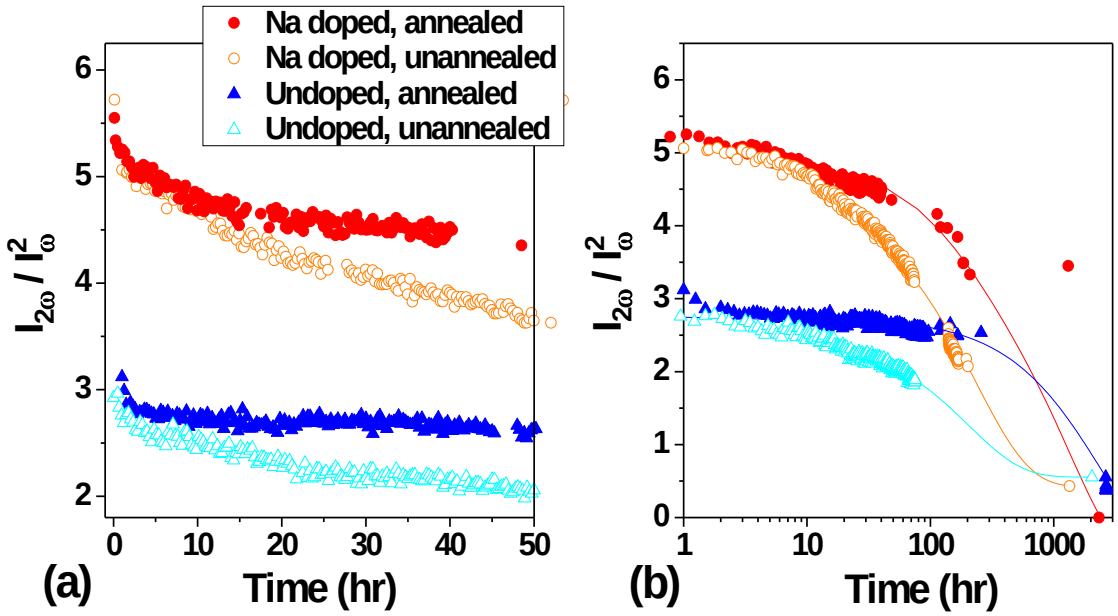

Figure 31: Time dependence of the SHG intensity of thermally poled annealed and unannealed Na-doped and undoped Ta_2O_5 layers on borosilicate glass substrate

For all samples, a fast decrease of the SHG signal is observed during the first three hours after thermal poling. After 50 hours the signal decreases by 23% for the doped annealed sample, by 35% for the doped unannealed sample, by 16% for the undoped annealed sample and by 28% for the undoped unannealed sample. The SHG signal decreases faster for Na-doped Ta_2O_5 thin films than for undoped Ta_2O_5 thin films. For both Na-doped and undoped samples the SHG signal of unannealed samples decreases faster than the SHG signal of the annealed ones. This trend is confirmed over longer periods seen in Figure 31b). The SHG signal of all samples decreases to reach a value close to zero approximatively 12 weeks after the poling treatment. The decay of the SHG is faster than expected and therefore to understand the cause of this, the electrical behaviour of the films were studied with impedance spectroscopy.

4.5 Impedance Spectroscopy

Impedance spectroscopy measurements were performed to understand the conduction mechanism which may cause of low $\chi^{(2)}$ and its instability of the films. The impedance were measured on the unannealed and annealed, Na-doped and undoped Ta_2O_5 films. Electrodes were applied on the top and bottom of the samples and an electrical signal is applied across the film to obtain the impedance.

4.5.1 Electrical Characterisation using Impedance Spectroscopy

Electrochemical impedance spectroscopy (EIS) is a method to characterise the electrical behaviour of a material, in the form of electrical impedance (Z) as a function of frequency. This was used to study the electrical behaviour of the depletion region formed during the thermal poling process. Impedance is the measure of resistance flow of the electric current [121] and can be expressed as a complex function with a real and imaginary part, where the real part is the resistance (R) and the imaginary part is the reactance (X). In cartesian form, $Z = R + jX$, and in polar form, in terms of its magnitude ($|Z|$) and phase (θ), $Z = |Z| \exp(j\theta)$. The impedance analyser presents the impedance frequency response as a Nyquist plot (real part vs imaginary part of impedance).

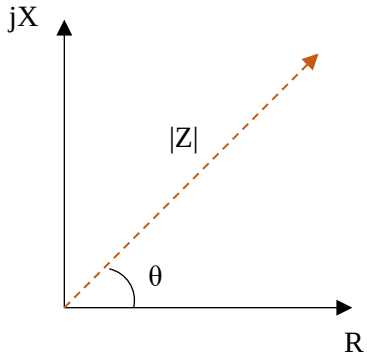

$$Z = R + jX$$

$$R = |Z|\cos\theta$$

$$X = |Z|\sin\theta$$

$$|Z| = \sqrt{R^2 + X^2}$$

$$\theta = \tan^{-1}\left(\frac{X}{R}\right)$$

Figure 32: Complex impedance plane

When an AC potential is applied to the sample through two electrodes, phase shift and amplitude of the resulting AC current, a Fourier series, can be analysed using Fast Fourier Transform (FFT) to determine the impedance.

To determine the electrical behaviour of the thin film and substrate, they can be modelled as an equivalent circuit in the form resistors and capacitors in series and/or parallel [122]. This is given in terms of the impedance of a resistor (Z_R) with resistance (R_p), and capacitor (Z_C) with capacitance (C_p). The impedance of a thin film can be

simply modelled by an equivalent circuit with a resistor and capacitor in parallel (RC circuit) [122], given by equation 13 and 14.

$$\frac{1}{Z_R} = \frac{1}{R_p}, \ \frac{1}{Z_C} = j\omega C_p \tag{13}$$

$$Z = \frac{1}{\frac{1}{Z_R} + \frac{1}{Z_C}} = \frac{R_p}{1 + j\omega R_p C_p} = \frac{R_p}{1 + (\omega R_p C_p)^2} + j\frac{\omega R_p^2 C_p}{1 + (\omega R_p C_p)^2} \tag{14}$$

The frequency response of a parallel RC circuit in the complex plane is represented as a semicircle, as shown in Figure 33a), where the lowest frequency starts at the largest X value and the highest frequency at the origin. Each parallel RC circuit will result in a semicircle, where the diameter (x-axis intercept) indicates the DC resistance. However the capacitance cannot be deduced directly from the Nyquist plot, as the frequency information is unknown. Instead, the impedance frequency response can also be presented in the form of bode plots, as shown in Figure 33b), in terms of its magnitude and phase at varying frequency. At the cut-off frequency $\omega_c(=2\pi f_c)$, which is defined as the point where the magnitude ($|Z|$) has dropped 3 dB and the phase (θ) is 45°, the capacitance can be determined by equation 15. On the Nyquist plot, the cut-off frequency is where the semicircle is maximum.

$$\omega_c = \frac{1}{RC} \tag{15}$$

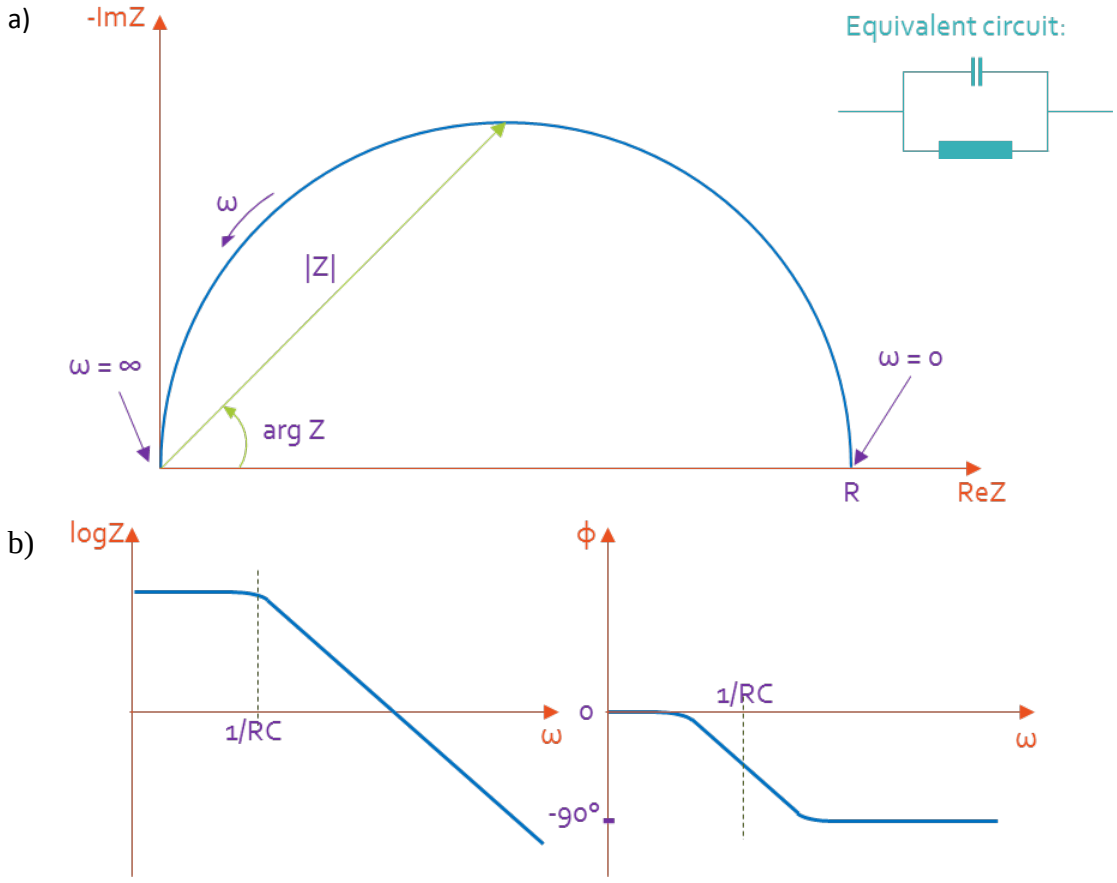

Figure 33: Frequency response from impedance spectroscopy of a parallel RC circuit represented as a) Nyquist plot and b) bode plots

4.5.1.1 Impedance Spectroscopy of Ta_2O_5

As mentioned previously, Ta_2O_5 has been used as a material for gate dielectric in CMOS circuits. Its electrical properties, such as its dielectric constant and breakdown strength, have therefore been well investigated. There have been reports of electrical studies of Ta_2O_5 thin films using impedance spectroscopy. Duggan et al. [123] and Sethi et al. [124] have both reported similar equivalent circuit model for RF sputtered Ta_2O_5 thin films, as shown in Figure 34. The reported DC resistivity for the RF sputtered film was between $3x10^3$ and $>10^8$ Ωm.

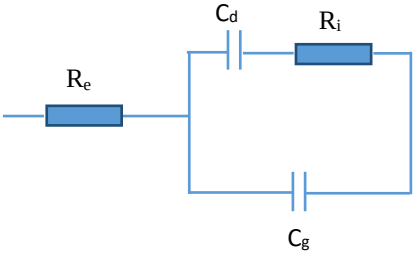

Figure 34: Equivalent circuit model of sputtered Ta_2O_5 film reported by Duggan et al. **[123]**, where R_e is the electrodes resistance, C_d is the double layer capacitance, R_i is the ionic resistance and C_g is the geometric capacitance between electrodes

4.5.2 Electrochemical Impedance Spectroscopy

The electrodes used in impedance measurement depends upon the measurement temperature and conductivity being investigated [125]. Gold, silver and platinum are the most commonly used for electrodes due to their high conductivity. An easily applicable silver epoxy paste (MG Chemical 8330S-21G) with a low resistivity (0.0007 Ωcm [126]) was chosen. Silver has lower resistance for temperatures below 600 °C, compared with gold and platinum [125]. The area of the electrodes were 1 by 1.5 cm. Insulated copper wire with stripped ends was then attached to the electrodes with some silver epoxy. The resistivity of the epoxy can be reduced by curing. This was performed in a furnace (Carbolite laboratory high temperature oven) at 65 °C, as recommended by datasheet, for 1 hour on one side and a further 1.5 hours after repeating the electrodes on the other side of the sample.

Impedance measurements were taken with an impedance analyser, Solartron 1260, which has a frequency range from 10 μHz to 32 MHz. An Agilent test fixture 16047E was used to connect up the sample to the analyser, and the sample is then placed into the furnace. The setup for the impedance measurement is as shown in Figure 35.

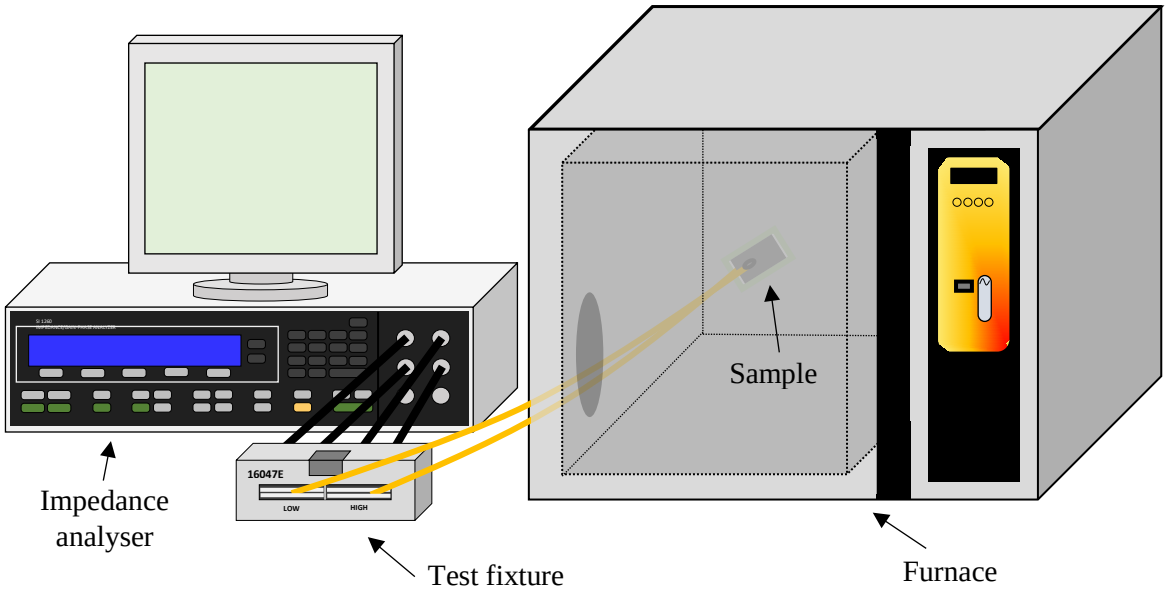

Figure 35: Setup for impedance measurement

As an initial measurement to ensure correct operation of the setup and equipment, impedance measurement was performed on a self-built electronic circuit with a 1 MΩ resistor in parallel to a capacitor of 3.3 pF. To deduce the equivalent circuit from the Nyquist plots, EIS data analysis software were employed. Using EC-Lab, it will fit the experimental impedance data to a circuit the user provides and determine the values of its resistors and capacitors which will provide a good fitting to the impedance data.

Impedance measurements were performed on Borofloat 33 substrate, annealed and unannealed Na:Ta_2O_5 on Borofloat 33 substrate, and annealed and unannealed Ta_2O_5 on Borofloat 33 substrate at 25, 100, 200 and 300 °C to investigate the conduction mechanism of the thin films at room temperature, temperature after poling, and at 300 °C, temperature at which poling occurs. The Ta_2O_5 films were deposited and annealed with the same parameters as the Na:Ta_2O_5.

Using the same method as the parallel RC circuit, the impedance data were fitted to equivalent circuit models. However the fitting of data with the model was poor, as an example for the Borofloat 33 substrate shown in Figure 36. Therefore calculating the resistivity of the thin was chosen as an alternative method to quantify the electrical behaviour.

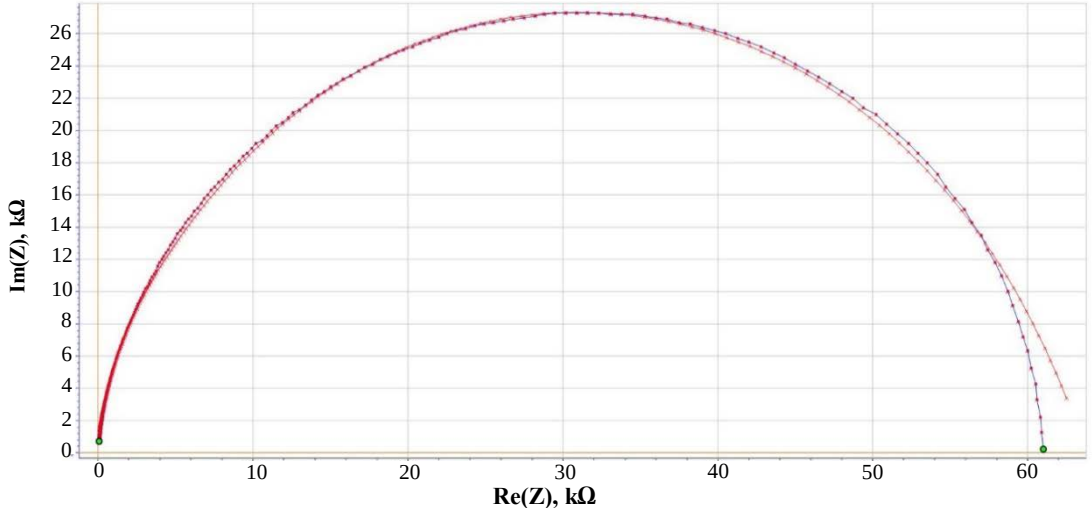

Figure 36: Fitting of impedance data of Borofloat 33 substrate (blue line) with an equivalent circuit model (red line)

4.5.3 Resistivity of Thin Film

The resistivity (ρ) of the film is calculated from the resistance, using equation 16.

$$\rho = \frac{R \cdot A}{l} \tag{16}$$

where A is the electrode area and l is the thickness of the film or substrate. The values used for the electrode area and film thickness are shown in Table 6.

Table 6: Electrode area (A) and film or substrate thickness (l) for Borofloat 33 substrate and Na-doped and undoped Ta_2O_5

	A, cm^2	**l, µm**
Borofloat 33 Substrate	2	1000
Na:Ta_2O_5/Ta_2O_5 Films	2	4

The DC resistance (R) of the samples can be identified as the intersection at the x-axis of the Nyquist plot. This was found by fitting a semicircle to the impedance data and determining the value at which the semicircle crosses the x-axis, as shown in Figure 37. To determine the resistance of the Ta_2O_5 thin films, the resistance of the Borofloat 33 substrate is removed from the total resistance of the sample.

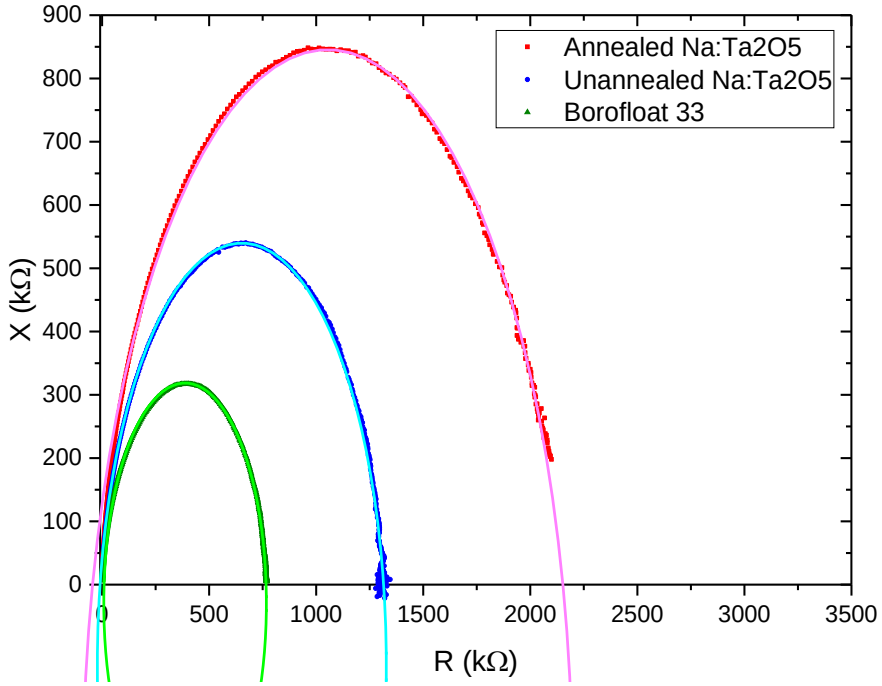

Figure 37: Nyquist plot of Borofloat 33 substrate, unannealed and annealed Na:Ta_2O_5 on Borofloat 33 substrate at 300 °C, with manual fitting of semicircles

This process was repeated for all the samples to calculate the resistivity of the Borofloat 33 substrate, unannealed and annealed, Na-doped and undoped Ta_2O_5 at 25, 100, 200 and 300 °C. The DC resistance of the Borofloat substrates was found to vary between 0.60 and 0.76 MΩ as the temperature increased from 25 to 300 °C. Estimation of film resistivity at temperatures below 200 °C was not possible due to the fluctuations of data from charging effects as the samples had high resistance at lower frequencies. Therefore for the measurements at 25 and 100 °C, the fitting of semicircles were not accurate and have not been discussed. For the measurements at 200 and 300 °C, the data had less fluctuations and so the data can be fitted well. Table 7 shows the resistivities of the Ta_2O_5 films at temperatures 200 and 300 °C.

Table 7: Resistivity (Ωm) extracted from impedance measurements of 4 μm unannealed and annealed Na-doped Ta_2O_5 layers, and unannealed and annealed undoped Ta_2O_5 layers performed at 200 and 300 °C

	Unannealed Na:Ta_2O_5	**Annealed Na:Ta_2O_5**	**Unannealed Ta_2O_5**	**Annealed Ta_2O_5**
200 °C	$1.11x10^9$	$4.24x10^9$	$7.14x10^9$	$1.15x10^{10}$
300 °C	$2.75x10^7$	$6.92x10^7$	$1.04x10^8$	$1.80x10^8$

The resistivity of all films decreased with increase in temperature, as expected in insulators. The resistivity of the Na-doped material is lower than that of the undoped materials, for both annealed and unannealed films, which could be due to the presence of mobile cations. The annealed films show higher resistivity than their unannealed counterparts, in both the Na-doped and undoped cases. When Ta_2O_5 is annealed in an oxygen atmosphere, the stoichiometry of the film improves and removes any structural defects formed during deposition (e.g. oxygen vacancies), improving the dielectric breakdown field [85]. The resistivities values of the undoped Ta_2O_5 films were within the range reported by Duggan et al. [123] for RF sputtered Ta_2O_5 films.

The unannealed and annealed Ta_2O_5 films appear to have the higher electrical resistance at all temperatures. Both the Na:Ta_2O_5 films and Borofloat 33 glass contains some sodium, 0.75 wt% Na_2O and 4 % Na_2O/K_2O [117] respectively, increases the electrical conductivity of both materials.

4.6 Discussion

Based on the Maker fringe analysis, the $\chi^{(2)}$ tensor of the thermally poled Ta_2O_5 films was shown to have an electro-optic origin referred to as EFISH (electric field induced second harmonic). This enables description of the second-order nonlinearity properties of poled Ta_2O_5 amorphous films in terms of the third-order optical susceptibility and the strength of the induced electric field, as described by $\chi^{eff(2)} = 3E_f \chi^{(3)}$. Immediately after poling, $\chi^{(2)}$ was found out to be 0.46 pm/V and 0.34 pm/V for an unannealed Na-doped and undoped Ta_2O_5 film, respectively, poled at 1.3 kV and 300 °C. Using $\chi^{(3)} \approx 11x10^{-21}$ m^2/V^2 [5] for our tantalum oxide thin films, the frozen-in electric field E_f can be estimated to be about 1.0 to 1.4×10^7 V/m. When comparing this with that in other polarised glassy networks it is important to consider only the studies in which the thermal poling treatment was carried out under blocking anodic electrode conditions, as it has been shown that using an open anode the field induced is one order of magnitude lower for the same glassy matrix [127]. Quiquempois et al. [128] reported $\chi^{(2)} = 0.40$ pm/V in silica Infrasil glass ($\chi^{(3)} \approx 2x10^{-22}$ m^2/V^2) poled under vacuum, Dussauze et al. [127] reported $\chi^{(2)} = 0.3$ pm/V for a soda-lime glass ($\chi^{(3)} \approx 0.6x10^{-22}$ m^2/V^2) poled under argon atmosphere and 5 pm/V for a phospho-niobate glass ($\chi^{(3)} \approx 5x10^{-21}$ m^2/V^2) [129]. For these three examples, the frozen-in electric field ranges from $0.3x10^9$ V/m up to $1.6x10^9$ V/m, which is respectively approximately 20 and 100 times higher than the field strength obtained for Ta_2O_5 films in the present study. In addition, as the thicknesses of the polarised layers reported are similar in all

these studies (2- μm of thickness), these differences in field strength can be correlated with the uncombined charge density reached in each of these polarised amorphous oxide materials. From our experiments on amorphous Ta_2O_5 films, the charge density can be estimated at $0.77x10^3$ Cm^{-3} (considering $\varepsilon_r = 25$ [130], L= 4 μm and $E_f = 1.4x10^7$ V/m) which is about an order of magnitude lower than the charge density evaluated in the thermally poled oxide glasses used for comparison [127]. This indicates that the relatively low second-order optical response measured in these Ta_2O_5 films can be linked to the lower density of uncombined charges which can be sustained by this amorphous matrix.

To explain this observation, charge dissociation processes during the thermal poling treatment must be considered. Poling induces the departure of mobile cations from the depletion region underneath the anode which is partially compensated in the presence of other mobile species, thereby reducing the space charge. In the case of poling under vacuum or in an inert gas, the departure of positive charges is compensated only by the motion of negative charges from the glass network. The nature and conduction mechanisms of these negative charge carriers are still unclear but several hypotheses have been suggested. Oxygen anion motion was first suggested by Carlson. [131, 132]. Other studies have noted that molecular oxygen has been observed in polarised glassy matrices, which was explained either by oxidation of the anions and release of electrons [95, 133] or by the formation of peroxide radicals through bond breakage which could then react to form molecular oxygen [134]. However, when the internal electric field reaches a value close to the dielectric breakdown strength, electronic charge carriers play an important role. In this way, the low density of uncombined charges achieved within the thermally poled Ta_2O_5 films can be explained by higher electronic conductivity during the poling process for Ta_2O_5 films as compared to other classical oxides such as silicate glasses. In other words, the activation energy of the compensation mechanism (i.e. negative charge motion) is much lower for Ta_2O_5 films, which lowers the strength of the space charge, limiting the frozen-in field.

The stability of the SHG signal after poling and the influence of prior thermal annealing of the Ta_2O_5 layer upon this was also investigated in this work. This is an important factor to consider for comparison with materials with inherent second-order nonlinearity. It was observed that for both Na-doped and undoped samples the SHG signal from unannealed samples decreases faster than the SHG signal of the annealed samples. The $\chi^{(2)}$ was monitored over a period and was found to have decayed close to 0 by 4000 hrs. The decay was much quicker than the first thermally poled SiO_2 sample by Myers [113], where they did not observe much decay of SHG months after first poling. The SHG stability in WO_3-TeO_2 thermally poled glass were found to be unstable even quicker than Ta_2O_5, Narazaki et al. [135] believed that the decay is due to the diffusion of Na ions. Thermal poling of chalcogenides were also found to less stable than SiO_2, Zaghlache et al. [136] reported that the SHG intensity and stability of sulfide chalcogenide could be improve by repoling the sample several times after the SHG has decayed away.

The SHG decay curves of Ta_2O_5 were found to follow a classical stretched exponential (equation 12) similar to the trapping model developed to describe electronic relaxation in amorphous semiconductors where excitons diffuse and recombine at network defects [120]. In the case of the poled Ta_2O_5 films, relaxation starts with the density of uncompensated charges formed during the poling treatment. These can diffuse and reach a "sink", a network defect, which will neutralize these excitons. At later times, excitons must diffuse over larger distances in order to be neutralised. In the case of an amorphous material the distribution of "traps" or "sinks" within the network is expected to be randomly distributed, resulting in an exponential decay stretched in time as described by the term β deviating from $\beta=1$. By fitting the measured SHG decay curves to equation 12 the β values obtained range from 0.65 to 0.75, similar to the results obtained in other amorphous semiconductors [120] and which supports the hypothesis of exciton diffusion within an amorphous network. The fitting procedure also confirms that relaxation times increase significantly with annealing. The two main annealing effects on the properties of amorphous Ta_2O_5 films are (i) a decrease in the refractive index explained by a replenishment of oxygen vacancies in the glass network during annealing and (ii) an increase in the electrical resistivity. These two observations, in the context of a trapping model for electrical charge relaxation, can explain the influence of annealing on (i) the diffusion coefficient of excitons which could be related to the resistivity and on (ii) the number of network defect or "sinks" in the films which could be linked to the oxygen vacancies.

4.7 Conclusion

Second-order optical nonlinearity was induced in amorphous Ta_2O_5 thin films by thermal poling. The effect of the electric field during the poling on the localisation of NLO layer within the thin film was studied and an applied voltage of 1.3 kV was found to produce a symmetrical NLO layer in a 4 µm Ta_2O_5 thin film. Effect of Na-doping and annealing on the induced nonlinearity has been studied using Maker fringe analysis. The stability of the induced nonlinearity over 3000 hours has been studied for annealed and unannealed, Na-doped and undoped Ta_2O_5 samples and the decay mechanisms based on EFISH have been discussed, in addition to comparing the conductivities of these samples at elevated temperatures close to poling temperature. These studies provided useful insight into the decay mechanism in relation with the structural units of the amorphous Ta_2O_5 network and research is underway to optimise the network and stabilise the induced nonlinearity by adding various cations and using a different HMO host. Demonstration of induced nonlinearity in amorphous HMO thin films leads to the realisation of electro-optic functionality in planar lightwave circuits especially in the mid-IR paving a way to tunable mid-IR devices such as modulators and on-chip FTIR spectrometers. However more work needs to be done to improve the stability and magnitude of the induced $\chi^{(2)}$.

Chapter 5 Multilayer Grating-assisted Coupler between Silicon-on-Insulator and Tantalum Pentoxide Waveguides

5.1 Introduction

Silicon photonics can be further enhanced with integration of other photonic devices which could be on another material onto a silicon platform. With increasing demands for increasing applications on a chip, the number of layers and interest for miniaturisation of integrated circuits have increased. Tantalum pentoxide (Ta_2O_5) is a CMOS-compatible material and its refractive index of 2.1 around 1.55 μm gives it a high index contrast to SiO_2 cladding of 1.46, makes it a suitable candidate for realising compact circuits with strong light confinement. Integration of Ta_2O_5 integrated devices can complement SOI waveguides to provide extra functionalities on multilayer silicon photonic circuits. In order to interface the between different material layers, the light has to be able to couple from one layer to another. There are two types of vertical coupling for multilayer, intralayer and interlayer. Intralayer is the coupling of light to another layer and interlayer is within the same layer.

Reports on intralayer and interlayer vertical multilayer coupling on a silicon platform have been on coupling between the same material or closely matched index material. A slope waveguide vertical coupler for coupling between layers in a silicon was reported in [137]. The coupler is in the form of a continuous waveguide joining from the bottom layer to a top layer. However this method is not as feasible for coupling between different materials. Grating couplers was another method for coupling to another layer of the same material by Zhang et al. [138] on a silicon platform. There have been demonstrations of coupling between different materials on a silicon platform, in particular between Si_3N_4 and a SOI platform [139, 140, 141]. There was also a design and analysis of using a grating-assisted coupler was presented by Masanovic et al. [142] to couple from between 3 layers, silicon oxynitride (SiON), Si_3N_4 and Si.

Grating-assisted coupler is one of the methods of coupling between two mismatched layers which can be of different material. With long grating periods, grating-assisted coupler provides easy fabrication with conventional photolithography, and also allows for selective wavelength tuning. It is suitable for applications such as filtering, switching and multiplexing. This chapter looks at using grating-assisted coupler to integrate Ta_2O_5 integrated devices onto silicon platforms, by investigating the coupling between a silicon waveguide layer with a Ta_2O_5 waveguide layer. Due to the large difference in refractive index of Si (3.477 at ~1.5 μm) and Ta_2O_5 (2.1 at ~1.5 μm), coupling between the two layers is weak. However with the additional of gratings, coupling can occur.

5.1.1 Grating-assisted Coupler Theory

When two identical waveguides (directional coupler) are in close proximity with each other, due to the overlap of the evanescent field from each waveguide, coupling between the compound modes of the waveguides occur. Compound modes are the modes of individual waveguide that has been perturbed due to the close presence of the other waveguide, creating a superposition of the two individual waveguide modes. Complete power coupling can only occur when the propagation constant of the two waveguides compound modes are the same [143], which is the phase-matching condition. For non-identical waveguides especially with a large refractive index difference, the coupling is weak due to the mismatch of the propagation constants of these waveguides, as shown in Figure 38a). However a grating (periodic perturbation) with period Λ can be added on one of the waveguides to phase match these two waveguides, as shown in Figure 38b). Such a waveguide structure is called a grating-assisted coupler.

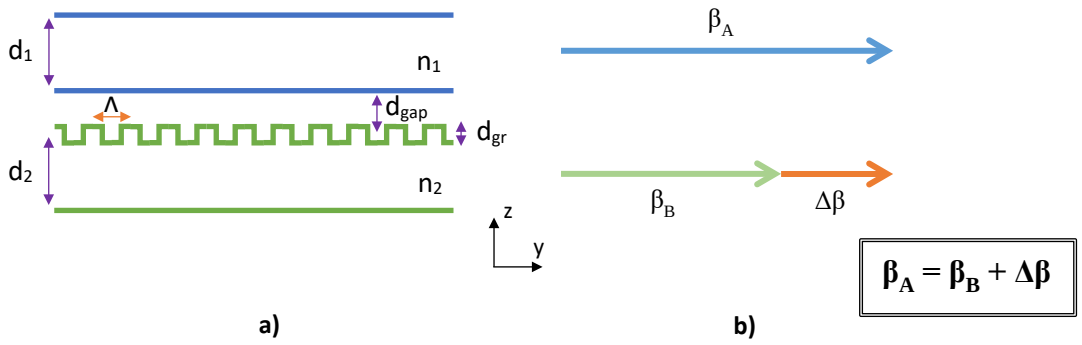

Figure 38: a) Grating-assisted coupler b) phase-matching condition

The grating ($\Delta\beta$) changes the propagation constant (β_B) of the compound mode, that the waveguide it is on, to match that of the compound mode of the other waveguide (β_A). The coupling length (L_c) required for complete power transfer from one waveguide to the other waveguide and back again can be calculated using equation 17 [143].

$$L_c = \frac{2\pi}{\beta_B - \beta_A} \tag{17}$$

5.2 Grating-assisted Coupler Design and Simulation

A grating-assisted coupler was designed to couple between a Si (400 by 250 nm) and Ta_2O_5 (750 by 750 nm) waveguide. These waveguide dimensions were chosen as 750 by 750 nm was the largest simulated Ta_2O_5 waveguide to have single mode operation and for the Si waveguide it was the typical dimensions used in silicon photonics. The grating-assisted coupler was designed for operation at 1.5 μm, due to the availability

of laser sources for characterisation. However the design can be tailored for other wavelength operation. The schematic of the grating-assisted coupler is shown in Figure 39.

To determine the grating period required to these two waveguides, the effective index of the compound modes of the grating-assisted coupler has to be identified. These were simulated in COMSOL Multiphysics. The grating-assisted coupler cross-section model along the length of the waveguide was also simulated in COMSOL Multiphysics. 2D model was chosen it was a quicker alternative to a 3D model and can give a good approximation for the design of the grating-assisted coupler. This model helps understand the coupling behaviour between the two waveguides.

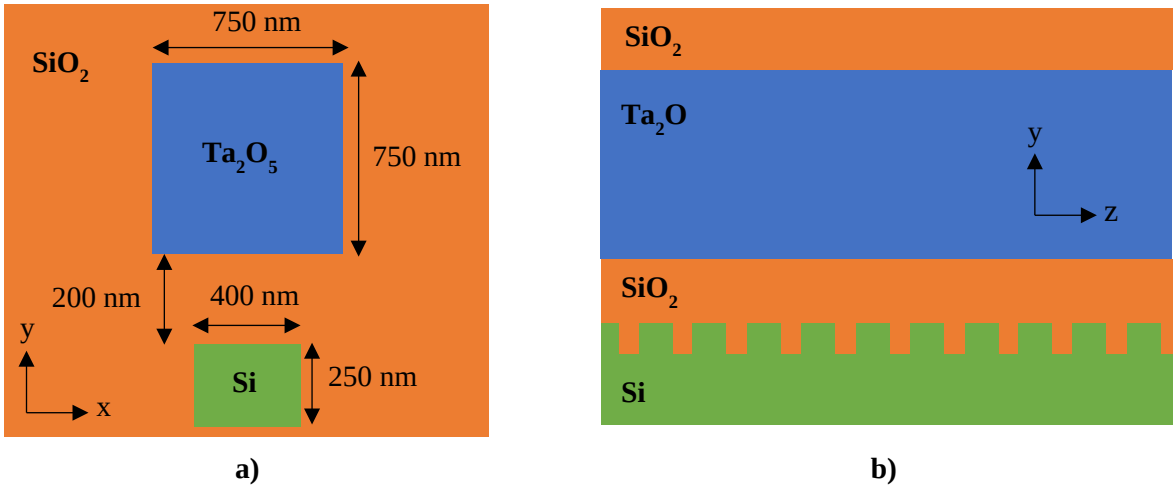

Figure 39: Schematic of grating-assisted coupler a)cross-section and b)along the waveguide propagation

5.2.1 Waveguides Cross-section

The cross-section of a Si and Ta_2O_5 channel waveguide was first simulated separately to determine the effective index of the fundamental mode of each waveguide. A model was built with the Wave Optics module in COMSOL Multiphysics, using the waveguide dimensions and refractive indices shown in Figure 40. Mode analysis was ran in the COMSOL model to generate the mode profile and its respective effective index of the fundamental waveguide mode and several other modes with similar effective index. The fundamental mode of each waveguide was determined by inspection of the generated mode profiles.

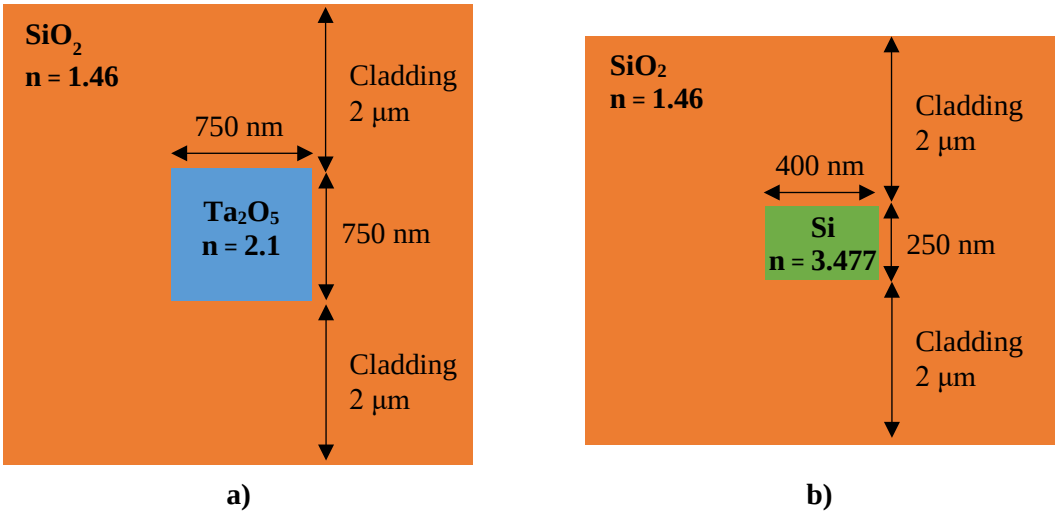

Figure 40: Cross-section of simulated waveguides a) Ta_2O_5 and b) Si

The simulated mode profile of a Ta_2O_5 and Si channel waveguides are shown in Figure 41a) and b) respectively. For a Ta_2O_5 channel waveguide with dimensions 750 by 750 nm, the effective index of the fundamental transverse electric (TE) mode was 1.814. A Si channel waveguide with width and height of 400 by 250 nm have a fundamental TE mode with an effective index of 2.4. Only TE polarisation was considered as the Si waveguide only has one guiding mode and it is in the TE polarisation.

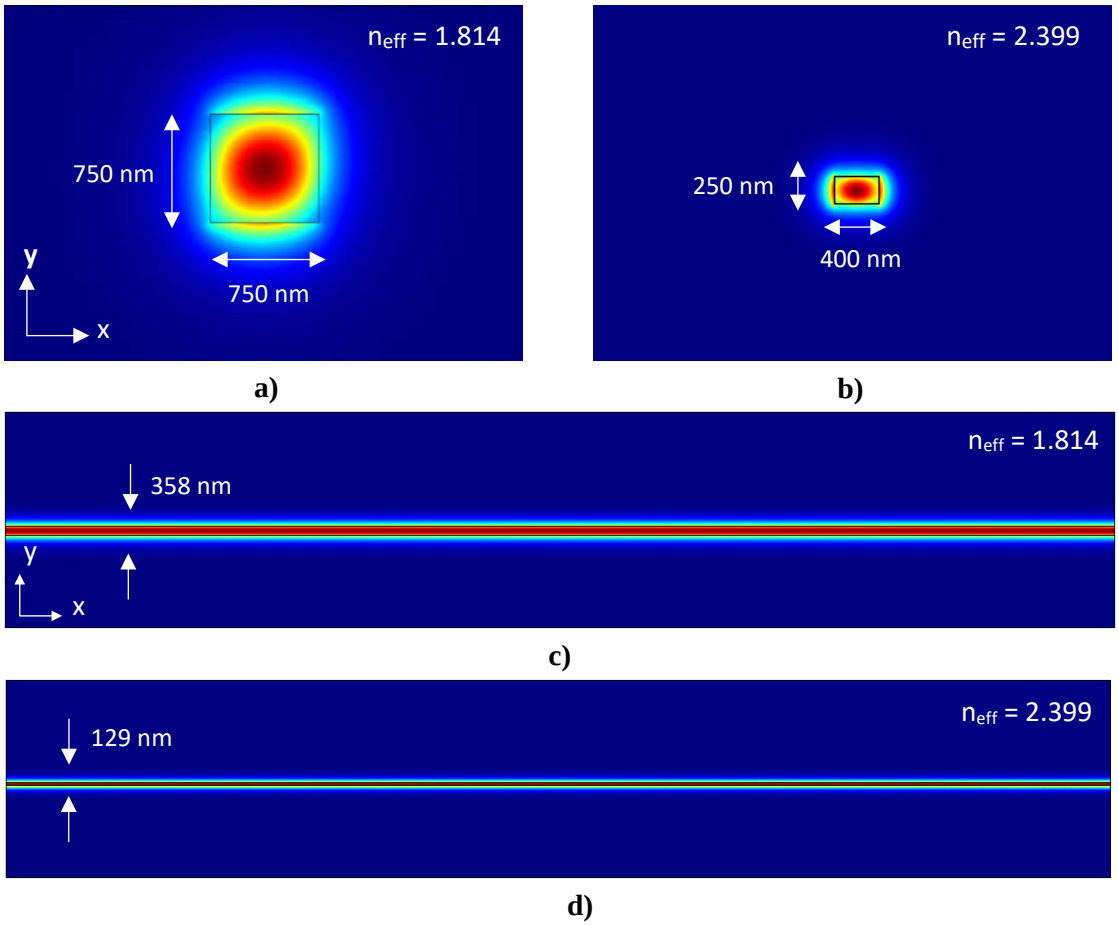

Figure 41: Cross-section simulation of a a) Ta_2O_5 channel waveguide and b) Si channel waveguide and its equivalent slab waveguide c) Ta_2O_5 slab waveguide and d) Si slab waveguide in TE polarisation

Due to the large computation time of 3D simulation model, the grating-assisted coupler was modelled as a 2D model. This was done using the effective index method, where the channel waveguides (Figure 41a) and b)) were reduced to a slab waveguide model (Figure 41c) and d)) with 50 µm width. A range of thickness of the Si and Ta_2O_5 slab waveguides were simulated to identify one that would achieve the same effective index as its channel waveguide equivalent. These were found to be 0.129 µm and 0.358 µm respectively.

5.2.2 Grating Period

In order to simulate the coupling between the two waveguides in the grating-assisted coupler, a model of the cross-section along the length of waveguide propagation was simulated. This requires the grating period to couple between the two waveguides. This was determined from the effective index of the two compound modes. Power transfer in grating-assisted coupler occurs between the compound modes of the structure. By obtaining the effective index of the two compound modes, n_{eff1} and n_{eff2}, it is possible to estimate the grating period (Λ) required to couple the compound modes, calculated using equation 18.

$$\Lambda = \frac{\lambda}{n_{eff2} - n_{eff1}} \tag{18}$$

The cross-sectional model of the grating-assisted coupler was built, this can be visualised as two slabs one on top of each other. It uses the thicknesses of the slab waveguides modelled in the previous section to simulate the effective index of the compound modes of the grating-assisted coupler and therefore determine the grating period. The study of the effect of varying the separation between the slab waveguides on grating period was investigated. This is shown in Figure 42.

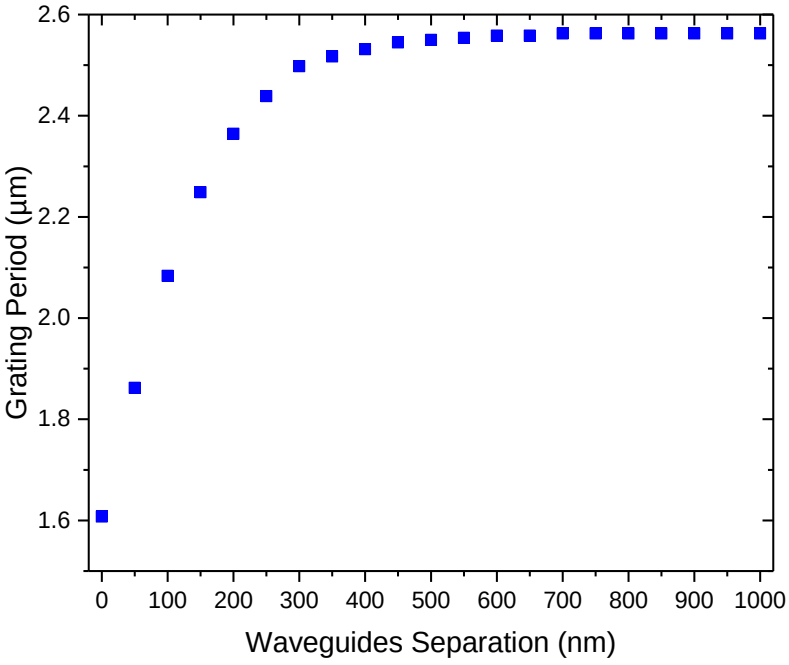

Figure 42: Grating period varying with waveguide separation

The grating period increases with waveguide separation but reaches a maximum value at a waveguide separation of 600 nm. As the separation increases, the mode field overlap of the waveguides decreases and the effective index of the compound modes resemble the individual slab modes in isolation. Therefore the grating period no longer increases. For grating-assisted design, a waveguide separation of 200 nm was chosen. This allowed better control of the waveguide separation layer during fabrication and also there was still overlap of the electric field of the slab modes. The overlap of the slab waveguides electric field at the grating position determines the strength of coupling strength [143]. Therefore for the best coupling strength, the grating was chosen to be positioned on the top of the Si waveguide, as found by Marcuse for coupling between two asymmetric waveguides [143].

At a waveguide separation of 200 nm, the two compound modes effective index were found to be 1.771 and 2.405, as shown in Figure 43. For an operating wavelength of 1.5 μm, using equation 18 the grating period required to couple between the Ta_2O_5 waveguide and a Si waveguide was 2.361 μm.

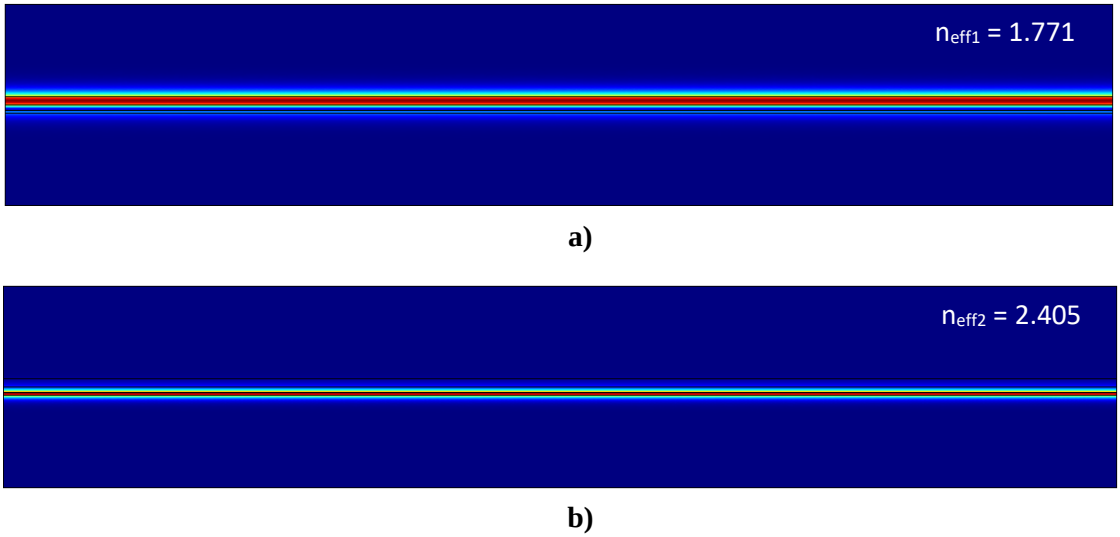

Figure 43: Cross-sectional model of grating-assisted coupler a) compound mode in Ta_2O_5 and b) compound mode in Si waveguides

5.2.3 Grating-assisted Coupler Propagation along Waveguide Length

After the determination of the effective indices of the compound modes, a cross-section along the length of the waveguide of the grating-assisted coupler was simulated to check the coupling between the two waveguides. 20 nm was decided to be the height of the gratings as this was the minimum thickness that will allow the control of the etched thickness. Sputtering will also provide a conformal SiO_2 separation layer on top of the gratings, the chosen grating height will minimise the effect of the conformity giving a flatter separation layer. Compared with a deeper etched grating, shallow etched grating yield weaker coupling between the waveguides, therefore a longer grating period and coupling length are required.

This shows the coupling behaviour and the coupling length, shown in Figure 44. Complete power transfer was achieved, demonstrated by the intensity in one waveguide was 0 when the other was at its maximum.

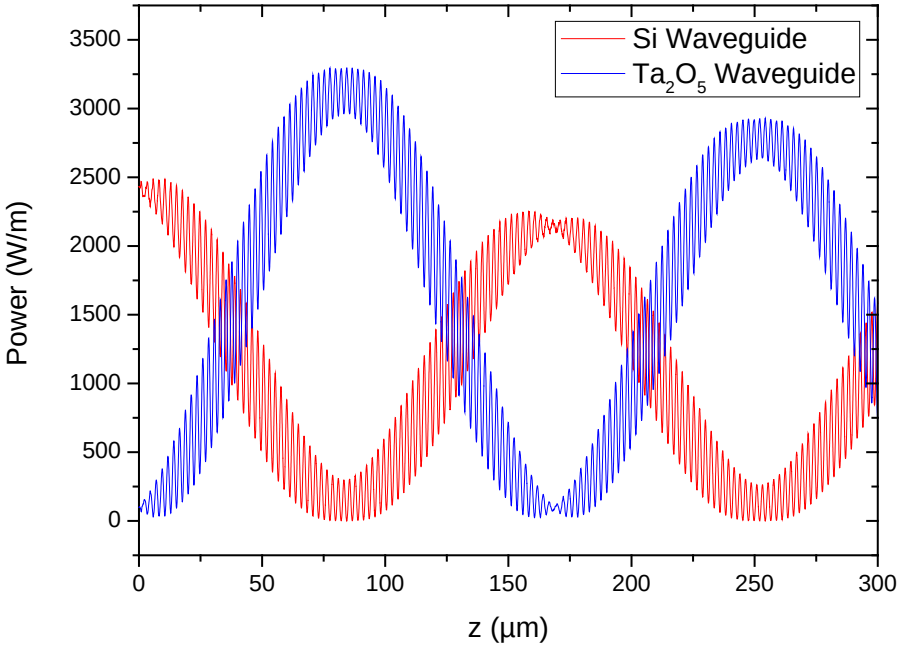

Figure 44: Power exchange between Si and Ta_2O_5 waveguide

Two oscillations can be observed in the power exchange of the two waveguides, one with a long period and the other with a short period. Firstly, the long period is due to the coupling between the two waveguides as power is transferred between the two waveguides. The short period is the coupling due to the gratings and the period represents the period of the gratings [144]. The length for power to couple completely (coupling length) from a Si channel waveguide to the Ta_2O_5 channel waveguide and back again was 170 μm.

5.2.4 Grating Position

The position of the gratings did not have to be on the top of the Si waveguide. They may also be located on the bottom surface of the top waveguide (Ta_2O_5) for good coupling strength [143]. The effect of the grating position was investigated with a COMSOL simulation.

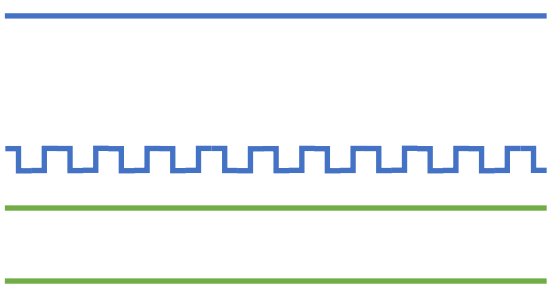

Figure 45: Position of grating in grating-assisted coupler at the bottom of top waveguide

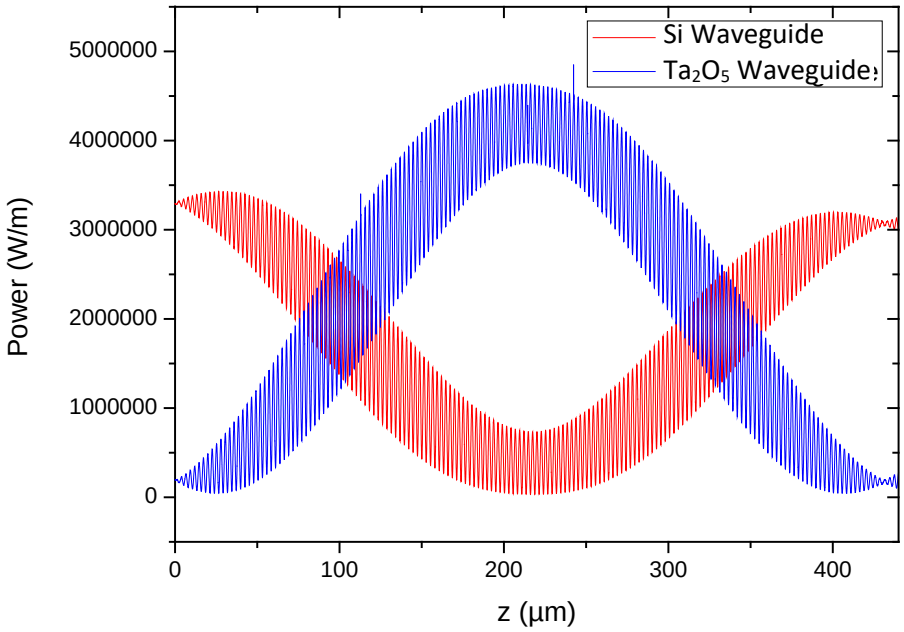

Figure 46: Power exchange with gratings underneath the Ta_2O_5 waveguide

The product of the electric field strength of the waveguides at the grating position determines the strength of coupling [143]. As the electric field strength is proportional to the effective index of the waveguide, therefore the coupling is weaker when the grating is located on the bottom of the Ta_2O_5 waveguide and strongest when on the top of the Si waveguide. As seen from Figure 46, the coupling length is longer when the gratings were on the bottom of the Ta_2O_5 waveguide, as the coupling length is inversely proportional to the coupling coefficient, κ, seen in equation 19. This phenomenon had also been observed by Marcuse in his grating-assisted couple model to couple between two waveguides in different material [143].

$$L_c = \frac{\pi}{2|\kappa|} \tag{19}$$

When the gratings were positioned on the bottom surface on the Ta_2O_5 waveguide, the coupling length increased to 450 μm.

5.3 Device Fabrication

The grating-assisted coupler is comprised of four main material layers which have to be processed. The Si layer where the Si waveguides and gratings will be realised. A SiO_2 layer which separates the Si and Ta_2O_5 layers. The Ta_2O_5 layer to realise Ta_2O_5 waveguides and lastly a SiO_2 overcladding layer.

Due to the number of fabrication steps, alignments marks are required to align the different layers. This was first realised by e-beam and etched into the substrate, 20 µm deep, which allows them to be visible after the deposition of the other layers. Next the gratings were realised in the Si layer also with e-beam lithography and inductively coupled plasma etching. With the gratings already position, it allows for less fabrication tolerances when realising the Si waveguide. The Si waveguide were also realised with e-beam lithography and inductively coupled plasma etching. Next the SiO_2 waveguide separation was deposition using RF sputtering and annealed. This is followed by the deposition and annealing of Ta_2O_5 layer. Due to the small waveguide dimension, the waveguides were patterned using e-beam lithography and were etched using ion-beam milling. Finally, a SiO_2 overcladding was deposited and annealed. The fabrication process flow is shown in Figure 47 and the fabrication process is detailed in Chapter 2 in sections below.

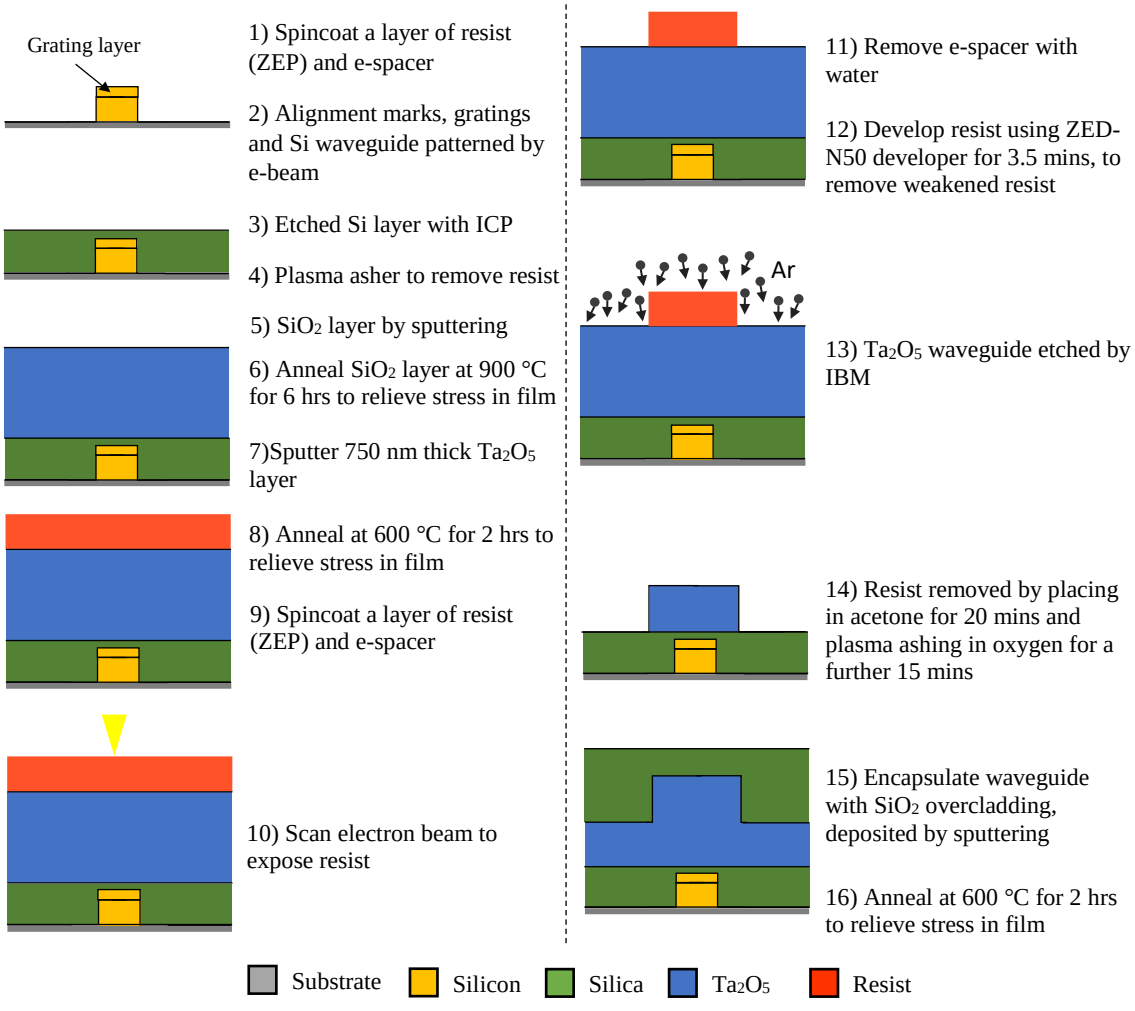

Figure 47: Grating-assisted coupler process flow

Several variation of the grating-assisted coupler will be fabricated on the chip. This is to compensate for any fabrication tolerances. A range grating period and the number of period around the calculated values were chosen. Adiabatic tapers were also added

to the input and output of some of the Si and Ta_2O_5 waveguide to improve the input and output coupling efficiency to the fibre. The tapers were 150 μm long, similar length to what have been reported for SOI waveguides [145], to taper from 1.5 μm to the waveguide widths. This is described in more detail in the next section.

5.3.1 E-beam Mask Design

E-beam lithography is a direct-writing method which uses a focussed electron beam to expose the resist with desired pattern. The design of the desired features was created in L-edit and converted into a GDS file format which is accepted by the e-beam lithography software. The design, as shown in Figure 48, is 20 by 30 mm and consists of four layers listed below. Each layer contains a 1 by 1 mm box which allows measurements of the thickness of each layer. The cross-sections of the grating-assisted coupler at the coupling region and end-facet are shown in Figure 49.

1. **Alignment marks -** There are 2 sets of 10 alignment marks, one on the left and right of the sample. These alignment marks are crosses which 400 by 400 μm and 20 μm thick.
2. **Gratings -** The gratings are located where the Ta_2O_5 waveguides overlay the Si waveguides. They are wider than the width of the Si waveguides and are placed first to allow easier alignments to the Si waveguides. With a 50% duty cycle, their half period varies from 1.14 to 1.22 μm. The grating periods are repeated 50, 100, 150, 250 or 500 times to allow for fabrication tolerances.
3. **Si waveguides -** Si waveguides have a width of 400 nm and have a bend region in the centre. This prevents launching into both waveguides at the same time. Some inputs and outputs of the Si waveguides have been widened to 1.5 μm to allow launching and collecting from the Si waveguide. To do this, adiabatic tapers have been added to taper the waveguide from a width of 1.5 μm to 400 nm over a 150 μm region [145]. There is a straight Si waveguide after every 5 couplers and also a 10 μm straight waveguide at the end of the sample, allowing easier characterisation if there are any problems with any waveguides.
4. **Ta_2O_5 waveguides -** All Ta_2O_5 waveguides are straight waveguides with 750 nm widths and are separated, in plane, from the Si waveguides by 150 μm. Similar to the Si layer, as mentioned above, there is a straight waveguide and a 10 μm wide waveguide after every 5 couplers and at the bottom of the sample, respectively.

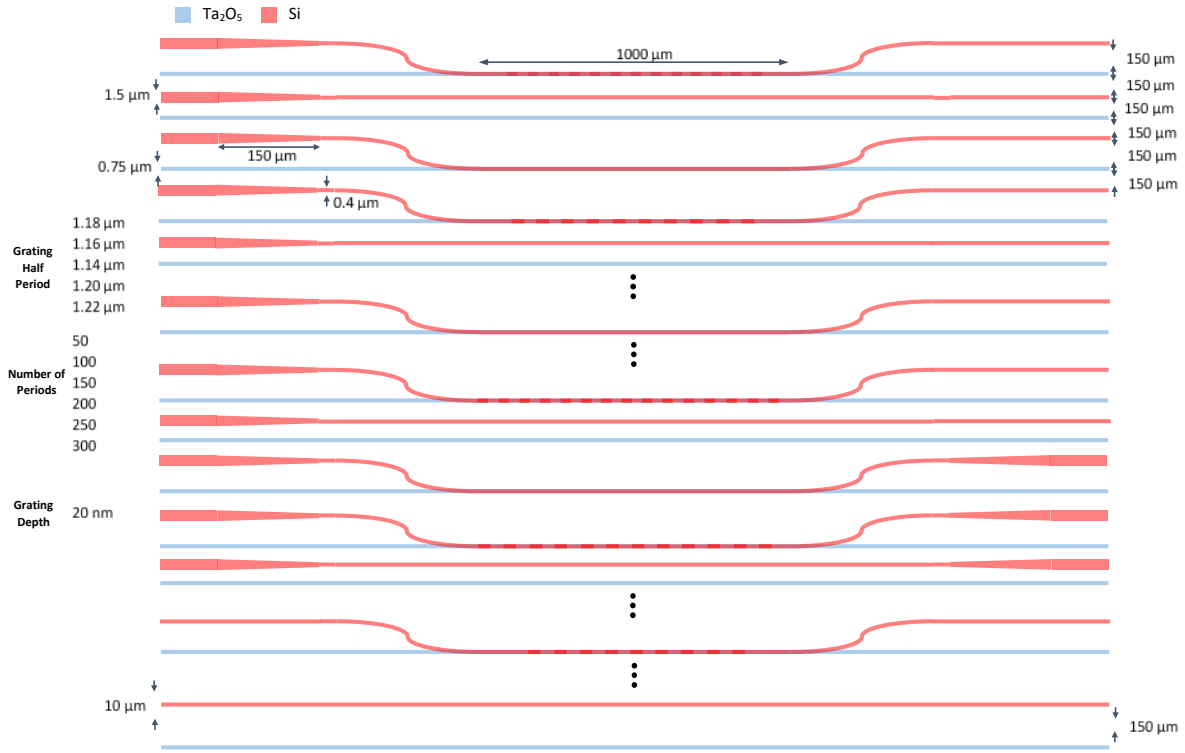

Figure 48: Grating-assisted coupler mask design

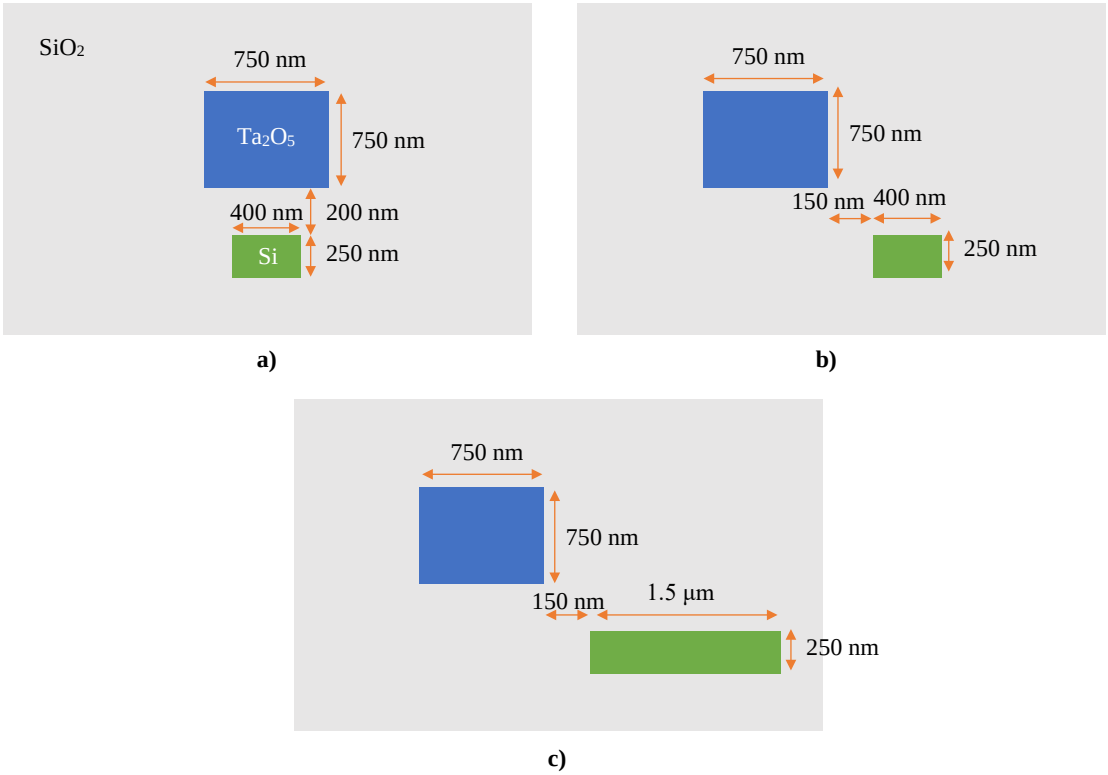

Figure 49: Grating-assisted coupler cross-section at a) coupling region, b)end-facet with no tapered waveguides, and c) end-facet with tapered Si waveguide

5.3.2 E-beam Lithography of Alignment Marks, Si Gratings and Waveguides

The Si gratings and waveguides were patterned with e-beam lithography as the waveguide dimensions were below the conventional photolithography resolution. This was performed with the same process as described in section 2.2.3.1. A 400 nm thick ZEP 520A resist layer was used for realising the Si waveguides. The e-beam and etching processes of the alignment marks, gratings and waveguides were performed by Dr. Ali Khokhar and Dr. SweZin Oo.

5.3.3 Etching of Alignment Marks, Si Gratings and Waveguides

The realisation of alignment marks, gratings and Si waveguide were realised by inductively coupled plasma (ICP) etching. This was performed with a chemistry of SF_6 (25 sccm) and C_4F_8 (65 sccm), ICP power of 800W, RF power of 50W and under a pressure of 15 mτ.

5.3.4 Deposition and Annealing of SiO_2 Gap

Following the realisation of Si waveguides, a 200 nm separation layer of SiO_2 was deposited. This was deposited with RF sputtering using the same parameters listed 2.2.6. This was followed by an annealing step to remove the defects due to sputtering in an oxygen atmosphere, in the 1200 °C tube furnace at 900 °C for 6 hours, with a ramp up and down rate of 1 °C/min and an oxygen flow of 2 l/min.

5.3.5 Deposition and Annealing of Ta_2O_5

The next step was to deposit the Ta_2O_5 layer, which was sputtered using the same parameters as in section 2.2.1. The samples were deposited at 200 °C with a deposition rate of ~2.6 nm/min. The Ta_2O_5 was also annealed after sputtering to reduce the defects and improve the stoichiometry of the Ta_2O_5. This was performed at 600 °C for 2 hrs.

5.3.6 E-beam Lithography of Ta_2O_5 Waveguides

As the width of the Ta_2O_5 waveguides were also below the size for conventional lithography, e-beam lithography was chosen for patterning the resist. 875 nm of ZEP resist and e-spacer was spun on top of the Ta_2O_5 layer. Using the alignment marks, the Ta_2O_5 layer was aligned with the Si layer and written with an electron beam.

5.3.7 Etching of Ta_2O_5 Waveguides

Waveguides were realised using ion-beam milling, where the area of the sample uncovered by the photoresist is bombarded with argon ions and removed. The parameters used for etching Ta_2O_5 are listed in section 2.2.4. This gives an etch rate of Ta_2O_5 of approximately 14 nm/min. After ion-beam milling, the resist was removed

using processes described in section 2.2.5. A microscope image of the etched Ta_2O_5 is shown in Figure 50.

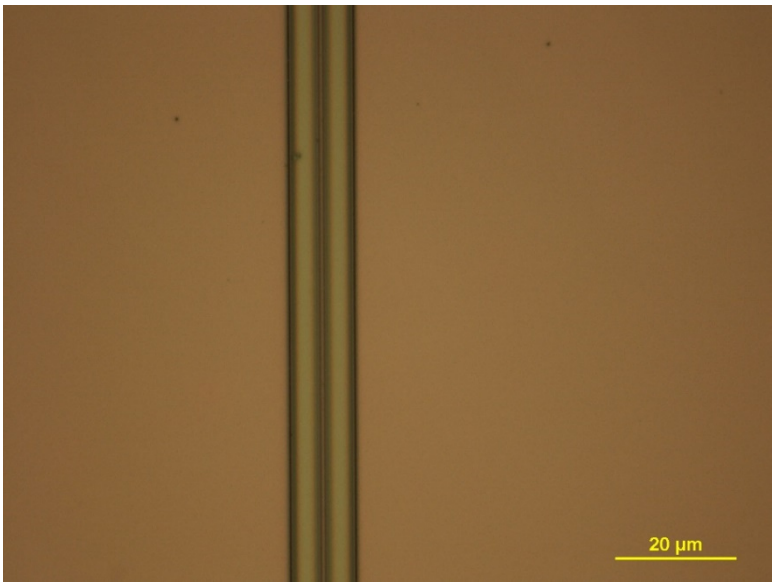

Figure 50: Microscope image of 750 x 750 nm Ta_2O_5 waveguide after IBM milling

5.3.8 Deposition and Annealing of SiO_2 Cladding Layer

The final fabrication step is to deposit an overcladding to encapsulate the Ta_2O_5 waveguides. This cladding layer can reduce the waveguide losses due to surface roughness and protects the waveguides. A 1.8 µm thick SiO_2 layer was deposited, using the same recipe as in section 5.3.4. The overcladding layer was annealed at 600 °C for 2 hrs, with the same parameters for annealing Ta_2O_5 as it is not possible to anneal this SiO_2 layer at 900 °C, the same temperature as the annealing of the SiO_2 gap layer, which will cause the Ta_2O_5 to crystallise.

5.3.9 Polishing

Butt coupling was chosen as the input and output coupling method. Both end-facets of the sample was lapped and polished to obtain an optical finish, as described in section 2.2.7.

5.4 Fabrication Evaluation

To check if the fabrication process went as expected, the height of the Ta_2O_5 waveguides were measured after the removal of the resist with a stylus profiler. The etched depth was measured to be 636 nm, which is less than expected. The estimated deposition thickness of the Ta_2O_5 layer was 750 nm, which means that the waveguides were not fully etched (channel waveguide) but rib waveguides were realised instead.

The fabricated Ta_2O_5 waveguide had an etch depth of 636 nm, rib height of 750 nm and width of 750 nm, as shown in Figure 51.

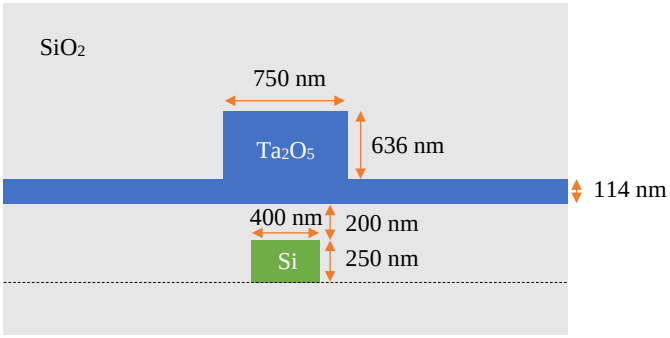

Figure 51: Cross-section of grating-assisted coupler after fabrication

The cause of the shallow etch is believed to be due to a thin resist layer and therefore the resist layer may have been completely etched away. The difference in etch depth will affect the coupling between the Si and Ta_2O_5 waveguides. The effective index of the Ta_2O_5 waveguide fundamental mode will be different and therefore the compound modes will differ. The COMSOL model described in section 5.2.3 was edited to depict the fabricated device dimensions. With a different Ta_2O_5 waveguide dimensions, a different grating period is required to couple between the two waveguides. However the grating period is fixed for the fabricated device, this can be solved experimentally with a different operating wavelength (equation 18). A wavelength sweep was performed in COMSOL to determine the wavelength at which full coupling between the Si and Ta_2O_5 waveguides can be achieved. This was found to be at 1.60 µm.

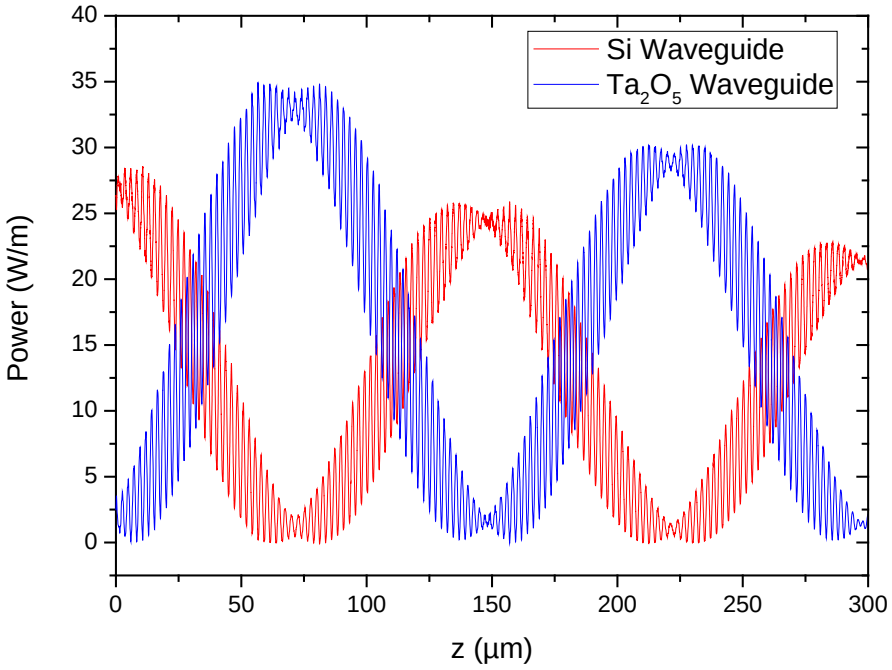

Figure 52: Power exchange between Si and Ta_2O_5 waveguide with waveguide dimensions after IBM at operating wavelength of 1.6 μm

A theoretical calculation was also performed to confirm this. The operating wavelength can be calculated using equation 18, using the simulated effective index of the Si and Ta_2O_5 waveguide compound modes and the grating period. This was found to be 1.63 μm, which correlates well with the COMSOL simulation. The small difference in wavelength is believed to be due to the addition of the gratings in the simulation along the propagation length of the waveguide, which has not been taken into account when simulating the compound modes. The operating wavelength of 1.63 μm is within the laser operating range.

5.5 Experimental Characterisation

A setup was built to characterise the grating-assisted coupler. Light from a tunable laser source (Agilent 8164B) was coupled into a single mode fibre (SMF28). This is then butt-coupled into a waveguide. The alignment of the fibre to the waveguide is monitored from the top with a microscope and a charge-coupled device (CCD) camera setup which is connected to a computer for viewing. The transmission signal is collected with a multimode fibre and connected to the in-built power meter of the tunable laser. The output power was observed to check for any transmission from the waveguide.

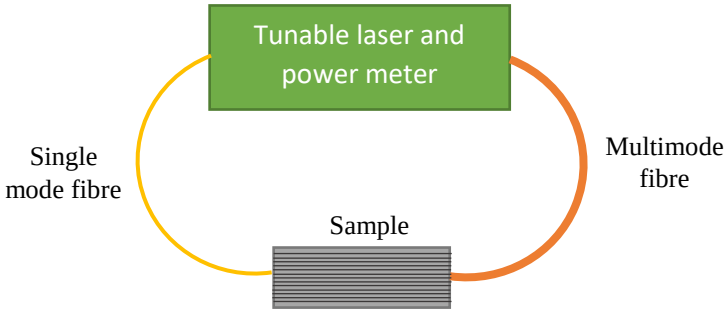

Figure 53: Apparatus for characterising grating-assisted coupler

Initial measurements were performed at operating wavelength of 1.5 μm with an input power of 7 dBm. Light was coupled in from the Si or Ta_2O_5 waveguide and collected from the Si or Ta_2O_5 waveguide. However, an output was not observed from either waveguide. A HeNe was used to allow visual inspection of the waveguide. As seen in Figure 54, inputting light from a Ta_2O_5 waveguide a streak of light propagating along the device can be observed and a spot was seen at the waveguide output from the top. On closer examination, light could be observed in the Si waveguide at the coupling region. This suggests that the device works and the problem could be due to poor vertical misalignment at the output, which can be solved by imaging both the end-facets for better vertical alignment. It could also be due to fabrication issues such as rough waveguide sidewalls or poor material quality, causing a high propagation loss, which in this case a new device has to be fabricated.

Figure 54: Initial characterisation of grating-assisted coupler with a HeNe input from a Ta_2O_5

5.6 Conclusion

This chapter describes the design, simulation and fabrication of a grating-assisted coupler to couple between a Ta_2O_5 and Si waveguide. COMSOL simulations were created to determine the grating period to couple between a 750 by 750 nm channel Ta_2O_5 and a 400 by 250 nm channel Si waveguide, separated by a 200 nm SiO_2 layer. The grating period was found to be 2.361 μm. Different position of the gratings were also simulated to see its effect on the grating period. The grating-assisted coupler was

designed for an operating wavelength of 1.5 μm due to the availability of pump source, however it can be tailored for other operating wavelength. The grating-assisted coupler demonstrate the possibility of realising optical devices on a Ta_2O_5 layer on a silicon platform which can interact with other silicon photonic devices on the platform.

Chapter 6 Conclusion and Future Work

Silicon photonics is a growing field but can be further enhanced with functionalities such as gain, switches which can be provided by integration with dielectric waveguide layers. In this thesis the design, fabrication and characterisation of several integrated devices realised in Ta_2O_5 were presented. This includes 1) Tm:Ta_2O_5 waveguide lasers, 2) induced second-order nonlinearity in Ta_2O_5 and 3) grating-assisted coupler between Si and Ta_2O_5 layers.

Chapter 2 established the fabrication process of Ta_2O_5 waveguides. Ta_2O_5 thin films were deposited using RF sputtering. Annealing were performed on the samples under oxygen atmosphere to relieve stress and replenish oxygen which have been depleted during the sputtering process, and improve the stoichiometry. Depending of Ta_2O_5 widths, the waveguides were patterned with either e-beam lithography or photolithography. Etching was then performed to realise the waveguides. Optimisation of etching process were performed to determine a process to produce smoother waveguide sidewalls. Compared with RIE, IBM produced more isotropic waveguides with smooth waveguide sidewalls and were therefore chosen as the etching method. Ta_2O_5 were cladded with SiO_2 layer to protect the surface of the waveguides. Finally, the waveguide end-facets were lapped and polished, to enhance the input and output coupling efficiency of the waveguides.

In Chapter 3, the first demonstration of Tm lasing in Ta_2O_5 and first spectroscopic characterisation of the material were introduced. The fabrication and optical characterisation of Tm:Ta_2O_5, with a Tm concentration of $9x10^{20}$ ions/cm^3, was described. Spectroscopic measurements were performed on the Tm:Ta_2O_5 waveguides to determine the emission and absorption cross-section, and the excited-state lifetime. The annealing temperature and duration on the peak photoluminescence and lifetime was studied. Highest photoluminescence was observed with a 2 μm sample annealed at 650 °C for 12 hours at the optimum pump wavelength of 795 nm. A high emission cross-section of $2.99x10^{-20}$ cm^2 and absorption cross-section of $8.05x10^{-21}$ cm^2 at 792 nm and $1.09x10^{-20}$ cm^2 at 1756 nm was achieved. The lifetime was found to be 477 ± 40 μs. Lasing was achieved with a 2 μm rib height, 330 nm etch depth and 3 μm wide Tm:Ta_2O_5 rib waveguide laser, firstly with just the waveguide polished end-facets (12.6% reflectivity) and also with a silver mirror (98.3% reflectivity) on the waveguide laser output. Lasing at 1238 nm and 1858 nm, and 1866 nm was attained respectively. A theoretical gain of 16.8 dB/cm and threshold pump of 8.7 mW was calculated. The high emission and absorption cross-section achieved, and calculated gain are higher than reported by Tm-doped materials.

Chapter 4 presents the induction of second-order nonlinearity in Ta_2O_5 by thermal poling. This was the first demonstration of induced nonlinearity in amorphous heavy metal oxide thin films. The fabrication, and optical and electrical characterisation of 4 μm thick unannealed and annealed, sodium-doped and undoped Ta_2O_5 thin films was reported. Following the fabrication of the thin films, the samples were thermally poled and characterised their induced second-order nonlinearity by collaborators in University of Bordeaux. The effect of annealing and doping with sodium ions on the induced second-order nonlinearity was studied. A $\chi^{(2)}$ of 0.46 pm/V and 0.34 pm/V was found for an annealed Na:Ta_2O_5 film and undoped Ta_2O_5 film respectively. The stability of the induced $\chi^{(2)}$ was studied for each sample for 3000 hours. A decay of SHG signal was observed for all samples, where it decayed faster for Na-doped Ta_2O_5 thin films than for undoped Ta_2O_5 thin films. In both cases the unannealed samples had a faster decay. In order to understand SHG stability, the electrical behaviour of the thin films were studied by impedance spectroscopy. The resistivity of Na-doped Ta_2O_5 films were nearly one order of magnitude lower than undoped Ta_2O_5 films, but the strongest second-order optical nonlinearity immediately after poling was induced in the Na-doped films despite their lower resistivity. Therefore the thermal poling effects cannot be just described by conduction properties of the materials. It is believed that the low induced second-order nonlinearity is due to the combination of charges lowering the strength of the space charge and limiting the frozen-in field. The stability of the SHG of the poled Ta_2O_5 are due to the electronic relaxation in the films where excitons diffuse and recombining at network defects.

Finally in Chapter 5, to consider the integration of Ta_2O_5 devices onto a silicon platform, a grating-assisted coupler to couple between a Si and Ta_2O_5 waveguide has been studied. Simulations of the grating-assisted coupler were performed with COMSOL Multiphysics to determine the grating period required to couple between a 750 by 750 nm Ta_2O_5 channel waveguide with a 400 by 250 nm Si channel waveguide at an operating wavelength of 1.55 μm. To reduce computation time, the device was simulated as a 2D model along the direction of light propagation. This was reduced down using the effective index method, where the channel waveguides are modelled as slab waveguides. The mode profiles of a Si and Ta_2O_5 channel waveguide was first simulated to determine the effective index of the individual waveguide. Next, the thickness of the slab waveguide which have the same effective index as the channel waveguide was determined. With these dimensions, a cross-section of the grating-assisted coupler was built, using a waveguide separation of 200 nm and grating height of 20 nm. The effective index of the compound modes of this structure is used to calculate the theoretical grating period require to couple between the two waveguides. A model of the grating-assisted coupler along the direction of waveguide propagation with the above mentioned parameters was simulated. It was found a grating period of 2.361 μm is required to couple between a Si and Ta_2O_5 channel waveguide and complete coupling of light from one waveguide to the other waveguide and back again can be achieved in 170 μm. The position of the gratings on the coupling strength of the device was also simulated and discussed. A grating-assisted coupler has been fabricated however due to the limited time, it has not been characterised.

The work presented in this thesis shows that tantalum pentoxide has great potential as a material for realising integrated photonic devices on a silicon platform. These devices can be incorporated together on the same chip providing different functionalities and foundation for integration with other established silicon photonic devices to realise a photonic integrated circuit.

5.7 Future Work

Further endeavours from the work demonstrated in this thesis are suggested in the sections below.

5.7.1 Multilayer Tm:Ta_2O_5 Ring Resonator Laser

To date, there has been no reports of Tm-doped laser sources integrated directly with silicon waveguides. Combining the work presented in Chapter 3 and Chapter 5 , the design of a multilayer ring resonator laser for integration with a silicon platform has been considered. The device will have three main layers encapsulated with SiO_2 layers. Starting with a SOI wafer, the silicon layer will be etched to realised waveguides. A SiO_2 layer separates the Si layer with the Tm:Ta_2O_5 layer. A Tm:Ta_2O_5 ring or racetrack resonator laser will be realised. Finally the Ta_2O_5 waveguide layer is also separated with another SiO_2 layer and encapsulated with a SiO_2 cladding. The design is shown in Figure 55. The advantages of this configuration, firstly is the benefit of easier fabrication process. It allows simple method of doping just the ring or racetrack with thulium ions compared to selective doping and also vertical coupling between the waveguides and resonators can be accurately controlled by tailoring the separation layer between them. Secondly, it allows the collection of the laser signal in a different waveguide of a different material, in this case Si, to interface with other devices on the silicon platform. The coupling between the Si and Ta_2O_5 layers can be achieved by incorporating the grating-assisted coupler design discussed in Chapter 5. Thirdly, the ring or racetrack resonator configuration do not require facets or grating to create a cavity and lastly pumping through an undoped Ta_2O_5 reduces the loss due to absorption of the pumped and emitted light by the unpumped thulium ions.

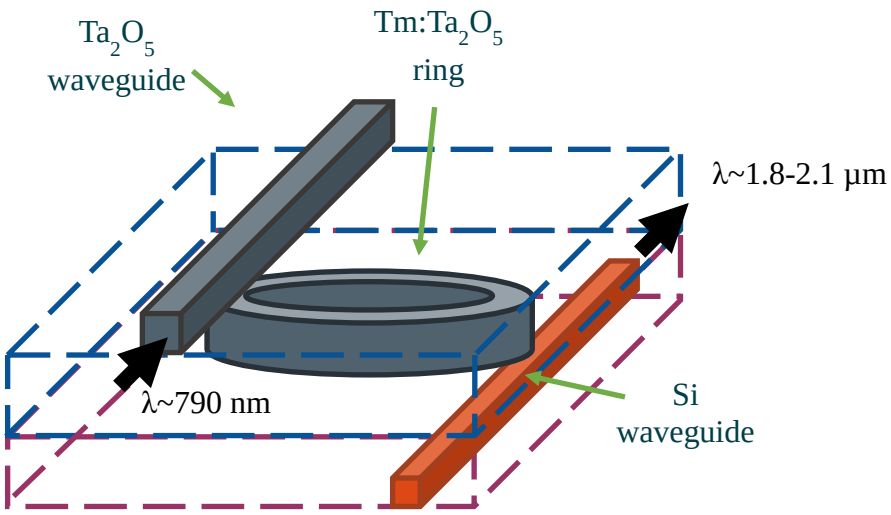

Figure 55: Multilayer Tm:Ta_2O_5 ring resonator laser configuration

5.7.2 Integrated Electro-optic Device in Ta_2O_5

Chapter 4 provided a foundation of using thermally-poled Ta_2O_5 as a material for integrated electro-optic applications, such as modulators and switches, compatible for integration with a silicon platform. Ta_2O_5 has potential to achieve high $\chi^{(2)}$, with its high $\chi^{(3)}$. Further optimisation of the material to improve the stability of the induced second-order nonlinearity is required. The incorporation of other cations may help optimise the network and improve the stability of the second-order nonlinearity induced. To understand the relaxation $\chi^{(2)}$, investigation of another similar material, niobium pentoxide (Nb_2O_5), has started. Nb_2O_5 is similar to Ta_2O_5 and has been widely use as optical coatings and for realising waveguides. Inducing second-order nonlinearity in borophosphate Nb_2O_5 thin films was previously demonstrated by Dussauze et al. [86], achieving a high $\chi^{(2)}$ of ~3 pm/V. Preliminary studies so far have been on optimisation of Na:Nb_2O_5 and Nb_2O_5 films.

The work presented so far were fabricated on Borofloat 33 substrate as initial tests. To demonstrate the potential of Ta_2O_5 as a material for CMOS integration with a silicon platform, investigation of inducing second-order nonlinearity on Ta_2O_5 samples on an oxidised Si wafers would be of interest. With induced nonlinearity in Ta_2O_5 thin films, and even better with optimised thin films, realisation of electro-optic functionality in planar lightwave circuits can be demonstrated.

References

[1] D. Thomson, A. Zilkie, J. E. Bowers, T. Komljenovic, G. T. Reed, L. Vivien, D. Marris-Morini, E. Cassan, L. Virot and J. M. H. J. M. Fédéli, "Roadmap on Silicon Photonics," *J. Optics*, vol. 18, no. 7, p. 073003, 2016.

[2] J. D. Bradley and E. S. Hosseini, "Monolithic Erbium- and Ytterbium-doped Microring Lasers on Silicon Chips," *Optics Express*, vol. 22, no. 10, p. 12226, 2014.

[3] F.-X. Jian and S. K. Kurinec, "Tantalum Oxide Thin Films for Microelectronic Applications," in *University/Government/Industry Microelectronics Symposium, 1995., Proceedings of the Eleventh Biennial* , Austin, TX, 1995.

[4] D. J. Moss, R. Morandotti, A. L. Gaeta and M. Lipson, "New CMOS-Compatible Platforms Based on Silicon Nitride and Hydex for Nonlinear Optics," *Nat. Photonics*, vol. 7, no. 8, p. 597, 2013.

[5] C. Y. Tai, J. S. Wilkinson, N. M. Perney, M. C. Netti, F. Cattaneo, C. E. Finlayson and J. J. Baumberg, "Determination of Nonlinear Refractive Index in a Ta2O5 Rib Waveguide using Self-phase Modulation," *Optics Express*, vol. 12, no. 21, pp. 5110-5116, 2004.

[6] K. S. Kim, W. A. Reed, K. W. Quoi and R. H. Stolen, "Measurement of the Nonlinear Index of Silica-core and Dispersion-shifted Fibers," *Optics Lett.*, vol. 19, no. 4, pp. 254-259, 1994.

[7] M. C. Tien, J. F. Bauters, M. J. Heck, D. J. Blumenthal and J. E. Bowers, "Ultra-low Loss Si_3N_4 Waveguides with Low Nonlinearity and High Power Handling Capability," *Optics Express*, vol. 18, no. 23, pp. 23562-23568, 2010.

[8] A. Aghajani, G. S. Murugan, N. P. Sessions, V. Apostolopoulos and J. S. Wilkinson, "Waveguide Lasers in Ytterbium-doped Tantalum Pentoxide on Silicon," *Optics Letters*, vol. 40, no. 11, pp. 2549-2552, 2015 .

[9] A. Z. Subramanian, C. J. Oton, D. P. Shepherd and J. S. Wilkinson, "Erbium-Doped Waveguide Laser in Tantalum Pentoxide," *IEEE Photonics Technology Letters*, vol. 22, no. 21, pp. 1571-1573, 2010.

[10] B. Unal, M. C. Netti, M. A. Hassan, P. J. Ayliffe, M. D. B. Charlton, F. Lahoz, N. Perney, D. P. Shepherd, C.-Y. Tai, J. S. Wilkinson and G. J. Parker, "Neodymium-doped Tantalum Pentoxide Waveguide Lasers," *IEEE J. Quantum Electron.*, vol. 41, no. 12, pp. 1565-1573, 2005.

[11] E. H. Bernhardi, H. A. van Wolferen, K. Wörhoff, R. M. De Ridder and M. Pollnau, "Highly Efficient, Low-threshold Monolithic Distributed-Bragg-reflector Channel Waveguide Laser in Al_2O_3:Yb^{3+}," *Optics Lett.*, vol. 36, no. 5, pp. 603-605, 2011.

[12] J. D. B. Bradley, L. Agazzi, D. Geskus, F. Ay, K. Wörhoff and M. Pollnau, "Gain Bandwidth of 80 nm and 2 dB/cm Peak Gain in Al_2O_3:Er^{3+} Optical Amplifiers on Silicon," *Journal of the Optical Society of America B*, vol. 27, no. 2, pp. 187-196, 2010.

[13] N. Li, P. Purnawirman, Z. Su, E. S. Magden, P. T. Callahan, K. Shtyrkova, M. Xin, A. Ruocco, C. Baiocco, E. P. Ippen and F. X. Kärtner, "High-power

Thulium Lasers on a Silicon Photonics Platform," *Optics Lett.*, vol. 42, no. 6, pp. 1181-1184, 2017.

[14] J. D. T. Kruschwitz and W. T. Pawlewicz, "Optical and Durability Properties of Infrared Transmitting Thin Films," *Appl. Optics*, vol. 36, no. 10, p. 2157, 1997.

[15] M. Belt, M. L. Davenport, J. E. Bowers and D. Blumenthal, "Ultra-low-loss Ta_2O_5-core/SiO_2-clad Planar Waveguides on Si Substrates," *Optica*, vol. 4, no. 5, pp. 532-536, 2017.

[16] Z. Todorova, N. Donkov, Z. Ristić, N. Bundaleski, S. Petrović and M. Petkov, "Electrical and Optical Characteristics of Ta_2O_5 Thin Films Deposited by Electron-Beam Vapor Deposition," *Plasma Processes and Polymers*, vol. 3, no. 2, pp. 174-178, 2006.

[17] J. Sundqvist, H. Högberg and A. Hårsta, "Atomic Layer Deposition of Ta_2O_5 Using the TaI_5 and O_2 Precursor Combination," *Chemical Vapor Deposition*, vol. 9, no. 5, pp. 245-248, 2003.

[18] M. S. Farhan, E. Zalnezhad and A. R. Bushroa, "Properties of Ta_2O_5 Thin Films Prepared by Ion-assisted Deposition," *Materials Research Bulletin*, vol. 48, no. 10, pp. 4206-4209, 2013.

[19] M. Acosta, I. Riech and E. Martín-Tovar, "Effects of the Argon Pressure on the Optical Band Gap of Zinc Oxide Thin Films Grown by Nonreactive RF Sputtering," *Advances in Condensed Matter Physics*, 2013.

[20] A. Z. Subramanian, C. J. Oton, J. S. Wilkinson and R. Greef, "Waveguiding and Photoluminescence in Er^{3+}-doped Ta_2O_5 Planar Waveguides," *Journal of Luminescence*, vol. 129, no. 8, pp. 812-816, 2009.

[21] S.-J. J. Wu, B. Houng and B.-S. Huang, "Effect of Growth and Annealing Temperatures on Crystallization of Tantalum Pentoxide Thin Film Prepared by RF Magnetron Sputtering Method," *J. of Alloys and Compounds*, vol. 475, no. 1-2, pp. 488-493, 2009.

[22] J.-P. Masse, H. Szymanowski, O. Zabeida, A. Amassian, J. E. Klemberg-Sapieha and L. Martinu, "Stability and Effect of Annealing on the Optical Properties of Plasma-deposited Ta_2O_5 and Nb_2O_5 Films," *Thin Solid Films*, vol. 515, no. 4, pp. 1674-1682, 2006.

[23] M. S. Ilango, M. D. Charlton and V. CC, "Etch Process Development of Tantalum Pentoxide (Ta_2O_5) using Photoresist (S1813)," *Nanoscience and Nanotechnology: An International Journal*, vol. 3, no. 2, pp. 36-40, 2013.

[24] S. Seki, B. Tsujiyama and T. Unagami, "Reactive Ion Etching of Tantalum Pentoxide," *J. Electrochem. Soc.*, vol. 130, no. 12, 1983.

[25] S. Franssila, "Etching," in *Introduction to Microfabrication*, John Wiley & Sons Ltd, 2004, pp. 125-127.

[26] S. J. Pearce, M. D. B. Charlton, G. J. Parker and J. S. Wilkinson, "Properties of Rare Earth Doped Thin Film Dielectric Layers for Upconversion Laser Waveguides," in *Solid State Lasers XX: Technology and Devices*, 2011.

[27] L.-C. Kuo, "Optical Waveguides and Microrings Fabricated using Ta_2O_5 Thin Films Grown by RF Magnetic Sputtering on Quartz Substrates," M.S. thesis, Dept. Photonics, National Sun Yat-sen University, Kaohsiung, Taiwan, 2015.

[28] J. D. Bradley, E. S. Hosseini, Purnawirman, Z. Su, T. N. Adam, G. Leake, D. Coolbaugh and M. R. Watts, "Monolithic Erbium- and Ytterbium-doped

Microring Lasers on Silicon Chips," *Optics Express,* vol. 22, no. 10, pp. 12226-12237, 2014.

[29] M. Belt and D. J. Blumenthal, "Erbium-doped Waveguide DBR and DFB Laser Arrays Integrated Within an Ultra-low-loss Si_3N_4 Platform," *Optics Express,* vol. 22, no. 9, pp. 10655-10660, 2014.

[30] A. Aghajani, G. S. Murugan, N. P. Sessions, V. Apostolopoulos and J. S. Wilkinson, "Waveguide Lasers in Ytterbium-doped Tantalum Pentoxide on Silicon," *Optics Letters,* vol. 40, no. 11, pp. 2549-2552, 2015 .

[31] A. Z. Subramanian, C. J. Oton, D. P. Shepherd and J. S. Wilkinson, "Erbium-Doped Waveguide Laser in Tantalum Pentoxide," *IEEE Photonics Technology Letters,* vol. 22, no. 21, pp. 1571-1573, 2010.

[32] E. H. Bernhardi, H. A. van Wolferen, K. Wörhoff, R. M. De Ridder and M. Pollnau, "Highly Efficient, Low-threshold Monolithic Distributed-Bragg-reflector Channel Waveguide Laser in Al_2O_3:Yb^{3+}," *Optics Lett.,* vol. 36, no. 5, pp. 603-605, 2011.

[33] A. D. Bristow, N. Rotenberg and H. M. van Driel, "Two-photon Absorption and Kerr Coefficients of Silicon for 850-2200 nm," *Appl. Physics Lett.,* vol. 90, no. 19, p. 191104, 20017.

[34] N. Kavanagh, M. U. Sadiq, K. Shortiss, H. Zhang, K. Thomas, A. M. Gocalińska, Y. Zhao, E. Pelucchi, P. A. O'Brien, B. M. Corbett and F. C. G. Gunning, "Exploring a new Transmission Window for Telecommunications in the 2 μm Waveband," in *2016 18th International Conference on Transparent Optical Networks (ICTON),* Trento, Italy, 2016.

[35] D. J. Richardson, "New Optical Fibres for High-capacity Optical Communications," *Philosophical Transactions of the Royal Society A: Mathematical, Physical and Engineering Sciences,* vol. 374, no. 2062, p. 20140441, 2016.

[36] A. Sincore, J. D. Bradford, J. Cook, L. Shah and M. C. Richardson, "High Average Power Thulium-Doped Silica Fiber Lasers: Review of Systems and Concepts," *J. Sel. Topics. Quantum Electron.,* vol. 24, no. 3, pp. 1-8, 2018.

[37] E. Russell, N. Kavanagh, K. Shortiss and F. C. G. Gunning, "Development of Thulium-doped Fibre Amplifiers for the 2μm Waveband," in *Fiber Lasers and Glass Photonics: Materials through Applications,* Strasbourg, France, 2018.

[38] Z. Su, N. Li, E. S. Magden, M. Byrd, T. N. Adam, G. Leake, D. Coolbaugh, J. D. Bradley and M. R. Watts, "Ultra-compact and Low-threshold Thulium Microcavity Laser Monolithically Integrated on Silicon," *Optics Lett.,* vol. 41, no. 24, pp. 5708-5711, 2016.

[39] B. Unal, M. C. Netti, M. A. Hassan, P. J. Ayliffe, M. D. B. Charlton, F. Lahoz, N. Perney, D. P. Shepherd, C.-Y. Tai, J. S. Wilkinson and G. J. Parker, "Neodymium-doped Tantalum Pentoxide Waveguide Lasers," *IEEE J. Quantum Electron.,* vol. 41, no. 12, pp. 1565-1573, 2005.

[40] P. Honzatko, A. Dhar, I. Kasik, O. Podrazky, V. Matejec, P. Peterka and B. Dussardier, "Preparation and Characterisation of Highly Thulium- and Alumina-doped Optical Fibers for Single-frequency Fiber Lasers," in *Photonics, Devices, and Systems V,* Prague, Czech Republic, 2011.

[41] J. K. Jones, "Diffusively Doped Thulium- and Ytterbium- Lithium Niobate Waveguide Lasers," Ph.D. Dissertation, Department of Physics, University of Southampton, Southampton, 1995.

[42] Y.-W. Lee, H.-Y. Ling, Y.-H. Lin and S. Jiang, "Heavily Tm^{3+}-doped Silicate Fiber with High Gain Per Unit Length," *Optical Materials Express,* vol. 5, no. 3, pp. 549-557, 2015.

[43] T. Yamamoto, Y. Miyajima and T. Komukai, "1.9 μm Tm-doped Silica Fibre Laser Pumped at 1.57 μm," *Electronics Letters,* vol. 30, no. 3, pp. 220-221, 1994.

[44] X. Wang, P. Zhou, H. Zhang, X. Wang, H. Xiao and Z. Liu, "100 W-level Tm-doped Fiber Laser Pumped by 1173 nm Raman Fiber Lasers," *Optics Lett.,* vol. 39, no. 15, pp. 4329-4332, 2014.

[45] M. George, R. Ricken, V. Quiring and W. Sohler, "In-band Pumped Ti:Tm:$LiNbO_3$ Waveguide Amplifier and Low Threshold Laser," *Laser & Photonics Reviews,* vol. 7, no. 1, pp. 122-131, 2013.

[46] S. D. Jackson and S. Mossman, "Efficiency Dependence on the Tm^{3+} and Al^{3+} Concentrations for Tm^{3+}-doped Silica Double-clad Fiber Lasers," *Appl. Optics,* vol. 42, no. 15, pp. 2702-2707, 2003.

[47] J. Ganem and S. R. Bowman, "Use of Thulium-sensitized Rare Earth-doped Low Phonon Energy Crystalline Hosts for IR Sources," *Nanoscale Research Lett.,* vol. 8, no. 1, p. 455, 2013.

[48] J. J. Penninkhof, "Erbium and Thulium Doped Planar Amplifier Materials," M. S. Thesis, Utrecht University, Utreht, 2002.

[49] E. S. Magden, P. Callahan, N. Li, J. D. Bradley, N. Singh, A. Ruocco, L. A. Kolodziejski, E. P. Ippen and M. Watts, "Frequency Domain Spectroscopy in Rare-Earth-Doped Gain Media," *IEEE Journal of Selected Topics in Quantum Electronics,* vol. 24, no. 5, pp. 1-10, 2018.

[50] P. Loiko and M. Pollnau, "Stochastic Model of Energy-transfer Processes among Rare-earth Ions. Example of Al_2O_3: Tm^{3+}.," *The Journal of Physical Chemistry C,* vol. 120, no. 46, pp. 26480-26489, 2016.

[51] K. Miura, T. Osawa, Y. Yokota, T. Suzuki and O. Hanaizumi, "Fabrication of Tm-doped Ta_2O_5 Thin Films using a Co-sputtering Method," *Results in Physics,* vol. 4, pp. 148-149, 2014.

[52] Y. Nomura and T. Fuji, "Efficient Chirped-pulse Amplification Based on Thulium-doped ZBLAN Fibers," *Appl. Physics Exp.,* vol. 10, no. 1, p. 012703, 2016.

[53] L. Dong and B. Samson, Fiber Lasers: Basics, Technology, and Applications, Boca Raton, FL: CRC Press, 2016.

[54] K. Miura, T. Osawa, Y. Yokota, T. Suzuki and O. Hanaizumi, "Fabrication of Tm-doped Ta_2O_5 Thin Films using a Co-sputtering Method," *Results in Physics,* vol. 4, pp. 148-149, 2014.

[55] K. Miura, T. Suzuki and O. Hanaizumi, "Observation of Violet-Light Emission Band for Thulium-Doped Tantalum-Oxide Films Produced by Co-Sputtering," *Materials Sciences and Applications,* vol. 6, pp. 656-660, 2015.

[56] M. Macatrao, M. Peres, C. Rubinger, M. Soares, L. Costa, F. Costa, T. Monteiro, N. Franco, E. Alves, B. Saggioro, M. Andreeta and A. Hernandes,

"Structural and Optical Properties on Thulium-doped LHPG-grown Ta_2O_5 Fibres," *Microelectronics Journal,* vol. 40, pp. 309-312, 2009.

[57] M. Hughes, D. W. Hewak and R. J. Curry, "Concentration Dependence of the Fluorescence Decay Profile in Transition Metal Doped Chalcogenide Glass," in *Optical Components and Materials IV*, San Jose, CA, 2007.

[58] V. Nikas, S. Gallis, M. Huang and A. E. Kaloyeros, "Thermal Annealing Effects on Photoluminescence Properties of Carbon-doped Silicon-rich Oxide Thin Films Implanted with Erbium," *Journal of Applied Physics,* vol. 109, no. 9, p. 093521, 2011.

[59] Y.-W. Lee, H.-Y. Ling, Y.-H. Lin and S. Jiang, "Heavily Tm^{3+}-doped Silicate Fiber with High Gain per Unit Length," *Optical Materials Express,* vol. 5, no. 3, pp. 549-557, 2015.

[60] M. Murray, T. Toney Fernandez, B. Richards, G. Jose and A. Jha, "Tm^{3+} doped Silicon Thin Film and Waveguides for Mid-infrared Sources," *Applied Physics Letters,* vol. 101, no. 14, p. 141107, 2012.

[61] S. D. Agger and J. H. Povlsen, "Emission and Absorption Cross Section of Thulium Doped Silica Fibers," *Optics Express,* vol. 14, no. 1, pp. 50-57, 2006.

[62] M. J. Digonnet, Rare-earth-doped Fiber Lasers and Amplifiers, 2nd ed., New York, USA: Marcel Dekker, 2001.

[63] D. A. Simpson, *Spectroscopy of Thulium Doped Silica Glass,* PhD Thesis, School of Electrical Engineering, Victoria University, 2008.

[64] P. Loiko and M. Pollnau, "Stochastic Model of Energy-transfer Processes among Rare-earth Ions. Example of Al_2O_3: Tm^{3+}.," *The Journal of Physical Chemistry C,* vol. 120, no. 46, pp. 26480-26489, 2016.

[65] M. Macatrao, M. Peres, C. P. L. Rubinger, M. J. Soares, L. C. Costa, F. M. Costa, T. Monteiro, N. Franco, E. Alves, B. Z. Saggioro and M. R. Andreeta, "Structural and Optical Properties on Thulium-doped LHPG-grown Ta_2O_5 Fibres," *Microelectronics Journal,* vol. 40, no. 2, pp. 309-312, 2009.

[66] A. S. K. Tong, C. J. Mitchell, J. I. Mackenzie and J. S. Wilkinson, "Photoluminescence of Tm-doped Ta_2O_5 waveguides," in *Proceedings of Conference on Lasers and Electro-Optics Pacific Rim (CLEO-PR),* Singapore, 2017.

[67] J. D. J. Ingle and S. R. Crouch, Spectrochemical Analysis, New Jersey: Prentice Hall, 1988.

[68] D. E. McCumber, "Einstein Relations Connecting Broadband Emission and Absorption Spectra," *Physics Rev.,* vol. 136, no. 4A, p. A954, 1964.

[69] F. Fusari, A. A. Lagatsky, B. Richards, A. Jha, W. Sibbett and C. T. A. Brown, "Spectroscopic and Lasing Performance of Tm^{3+}-doped Bulk TZN and TZNG Tellurite Glasses Operating Around 1.9 μm," *Optics Express,* vol. 16, no. 23, pp. 19146-19151, 2008.

[70] P. Peterka, I. Kasik, A. Dhar, B. Dussardier and W. Blanc, "Theoretical Modeling of Fiber Laser at 810 nm Based on Thulium-doped Silica Fibers with Enhanced 3H4 Level Lifetime," *Optics Exp.,* vol. 19, no. 3, pp. 2773-2781, 2011.

[71] B. R. Johnson, D. J. Creeden and S. D. Setzler, "Extreme Temperature Operation of Thulium-doped Silica Fiber Lasers," *Fiber Lasers XIV: Technology and Systems,* vol. 10083, p. 100830J, 2017.

[72] R. A. Soref, J. Schmidtchen and K. Petermann, “Large Single-mode rib Waveguides in GeSi-Si and Si-on-SiO_2,” *IEEE J. Quantum Electron.,* vol. 27, no. 8, pp. 1971-1974, 1991.

[73] S. Fu, W. Shi, J. Lin, Q. Fang, Q. Sheng, H. Zhang, J. Wen and J. Yao, “2μm Single Frequency Fiber Laser Based on Thulium-doped Silica Fiber,” in *Fiber Lasers XIII: Technology, Systems, and Applications*, San Francisco, CA, USA, 2016.

[74] M. J. Digonnet and C. J. Gaeta, “Theoretical Analysis of Optical Fiber Laser Amplifiers and Oscillators,” *Appl. Optics,* vol. 24, no. 3, pp. 333-342, 1985.

[75] N. Li, Purnawirman, Z. Su, E. Salih Magden, P. T. Callahan, K. Shtyrkova, M. Xin, A. Ruocco, C. Baiocco, E. P. Ippen, F. X. Kärtner, J. D. B. Bradley, D. Vermeulen and M. R. Watts, “High-power Thulium Lasers on a Silicon Photonics Platform,” *Optics Letters*, vol. 42, no. 6, pp. 1181-1184, 2017.

[76] P. Hua, “Integrated Optical Fluorescence Multi-Sensor System,” Ph.D. Thesis, Optoelectronics Research Centre, University of Southampton, Southampton, 2009.

[77] K. Kawano, O. Mitomi and M. Saruwatari, “Combination Lens Method for Coupling a Laser Diode to a Single-mode Fiber,” *Appl. Optics,* vol. 24, no. 7, pp. 984-989, 1985.

[78] E. Hecht, Optics 4th Ed., San Francisco, CA: Addison-Wesley, 2001.

[79] R. A. Myers, N. Mukherjee and S. R. J. Brueck, “Large Second-order Nonlinearity in Poled Fused Silica,” *Optics Lett.,* vol. 16, no. 22, pp. 1732-1734, 1991.

[80] K. Worhoff, J. D. Bradley, F. Ay, D. Geskus, T. P. Blauwendraat and M. Pollnau, “Reliable low-cost fabrication of low-loss Al_2O_3:Er^{3+} waveguides with 5.4-dB optical gain,” *IEEE J. Quantum Electron.,* vol. 45, no. 5, p. 454, 2009.

[81] C. Lacava, A. Aghajani, P. Hua, D. J. Richardson, P. Petropoulos and J. S. Wilkinson, “Nonlinear Optical Properties of Ytterbium-doped Tantalum Pentoxide Rib Waveguides on Silicon at Telecom Wavelengths,” in *Optical Fiber Communications Conference and Exhibition (OFC),* Anaheim, CA, USA, 2016.

[82] C. L. Wu, J. Y. Huang, D. H. Ou, T. W. Liao, Y. J. Chiu, M. H. Shih, Y. Y. Lin, A. K. Chu and C. Lee, “Efficient Wavelength Conversion with Low Operation Power in a Ta_2O_5-based Micro-ring Resonator,” *Optics Letters,* vol. 42, no. 23, pp. 4804-4807, 2017.

[83] M. Belt, M. L. Davenport, J. E. Bowers and D. J. Blumenthal, “Ultra-low-loss Ta_2O_5-core/SiO_2-clad Planar Waveguides on Si Substrates,” *Optica,* vol. 4, no. 5, pp. 532-536, 2017.

[84] K. Koskinen, R. Czaplicki, A. Slablab, T. Ning, A. Hermans, B. Kuyken, V. Mittal, G. S. Murugan, T. Niemi, R. Baets and M. Kauranen, “Enhancement of Bulk Second-harmonic Generation from Silicon Nitride Films by Material Composition,” *Optics Letters,* vol. 42, no. 23, pp. 5030-5033, 2017.

[85] E. Atanassova and A. Paskaleva, “Challenges of Ta_2O_5 as High-k Dielectric for Nanoscale DRAMs,” in *25th International Conference on Microelectronics*, Belgrade, Serbia, 2006.

[86] M. Dussauze, A. Malakho, E. Fargin, J. P. Manaud, V. Rodriguez, F. Adamietz and B. Lazoryak, "Large Second Order Optical Nonlinearity in Thermally Poled Amorphous Niobium Borophosphate Films," *J. Appl. Physics,* vol. 100, no. 1, p. 013108, 2006.

[87] A. S. K. Tong, F. Bondu, S. G. Murugan, J. S. Wilkinson and M. Dussauze, "Effect of Sodium Addition and Thermal Annealing on Second-order Optical Nonlinearity in Thermally Poled Amorphous Ta_2O_5 Thin Films," *J. of Appl. Physics,* vol. 125, no. 1, p. 015104, 2019.

[88] S. Fleming and H. An, "Progress in Creating Second-order Optical Nonlinearity in Silicate Glasses and Waveguides through Thermal Poling," *Frontiers of Optoelectronics in China,* vol. 3, no. 1, pp. 84-91, 2010.

[89] M. Cazzanelli, F. Bianco, E. Borga, G. Pucker, M. Ghulinyan, E. Degoli, E. Luppi, V. Véniard, S. Ossicini, D. Modotto and S. Wabnitz, "Second-harmonic Generation in Silicon Waveguides Strained by Silicon Nitride," *Nature Materials,* vol. 11, no. 2, p. 148–154, 2012.

[90] M. C. Larciprete, A. Belardini, M. G. Cappeddu, D. De Ceglia, M. Centini, E. Fazio, C. Sibilia, M. J. Bloemer and M. Scalora, "Second-harmonic Generation from Metallodielectric Multilayer Photonic-band-gap Structures," *Physical Rev. A,* vol. 77, no. 1, p. 013809, 2008.

[91] M. Zdanowicz, J. Harra, J. M. Mäkelä, E. Heinonen, T. Ning, M. Kauranen and G. Genty, "Second-harmonic Response of Multilayer Nanocomposites of Silver-decorated Nanoparticles and Silica," *Scientific Reports,* vol. 4, p. 5745, 2014.

[92] M. Dussauze, E. Fargin, M. Lahaye, V. Rodriguez and F. Adamietz, "Large second-Harmonic Generation of Thermally Poled Sodium Borophosphate Glasses," *Optics Express,* vol. 13, no. 11, p. 4064, 2005.

[93] B. Ferreira, E. Fargin, B. Guillaume, G. Le Flem, V. Rodriguez, M. Couzi, T. Buffeteau, L. Canioni, L. Sarger, G. Martinelli and Y. Quiquempois, "Second Harmonic Generation in Poled Tellurite Glass," *J. Non-crystalline Solids,* vol. 332, no. 1-3, p. 207, 2003.

[94] C. Lasbrugnas, P. Thomas, O. Masson, J. C. Champarnaud-Mesjard, E. Fargin, V. Rodriguez and M. Lahaye, "Second Harmonic Generation of Thermally Poled Tungsten Tellurite Glass," *Optical Materials,* vol. 31, no. 6, p. 775, 2009.

[95] G. Guimbretiere, M. Dussauze, V. Rodriguez and E. I. Kamitsos, "Correlation Between Second-order Optical Response and Structure in Thermally Poled Sodium Niobium-Germanate Glass," *Appl. Physics Lett.,* vol. 97, no. 17, p. 171103, 2010.

[96] M. Guignard, V. Nazabal, F. Smektala, J. L. Adam, O. Bohnke, C. Duverger, A. Moréac, H. Zeghlache, A. Kudlinski, G. Martinelli and Y. Quiquempois, "Chalcogenide Glasses Based on Germanium Disulfide for Second Harmonic Generation," *Adv. Functional Materials,* vol. 17, no. 16, p. 3284, 2007.

[97] R. Jing, Y. Guang, Z. Huidan, C. Guorong, K. Tanaka, K. Fujita, S. Murai and Y. Tsujiie, "Second-harmonic Generation in Thermally Poled Chalcohalide Glass," *Optics Lett.,* vol. 31, no. 23, p. 3492, 2006.

[98] H. Zeghlache, M. Guignard, A. Kudlinski, Y. Quiquempois, G. Martinelli, V. Nazabal and F. Smektala, "Stabilization of the Second-Order Susceptibility

Induced in a Sulfide Chalcogenide Glass by Thermal Poling," *J. Appl. Physics,* vol. 101, no. 8, p. 084905, 2007.

[99] M. Dussauze, X. Zheng, V. Rodriguez, E. Fargin, T. Cardinal and F. Smektala, "Photosensitivity and Second Harmonic Generation in Chalcogenide Arsenic Sulfide Poled Glasses," *Optical Materials Exp.,* vol. 2, no. 1, p. 45, 2012.

[100] A. Lepicard, F. Adamietz, V. Rodriguez, K. Richardson and M. Dussauze, "Demonstration of Dimensional Control and Stabilization of Second Harmonic Electro-Optical Response in Chalcogenide Glasses," *Optical Materials Exp.,* vol. 8, no. 6, p. 1613, 2018.

[101] D. Pureur, A. C. Liu, M. J. F. Digonnet and G. S. Kino, "Absolute Measurement of the Second-Order Nonlinearity Profile in Poled Silica," *Optics Lett.,* vol. 23, no. 8, p. 588, 1998.

[102] O. Sugihara, M. Nakanishi, H. Fujimura, C. Egami and N. Okamoto, "Thermally Poled Silicate Thin Films with Large Second-Harmonic Generation," *JOSA B,* vol. 15, no. 1, p. 421, 1998.

[103] Y. Ren, C. J. Marckmann, J. Arentoft and M. Kristensen, "Thermally Poled Channel Waveguides with Polarization-independent Electrooptic Effect," *IEEE Photonics Technol. Lett.,* vol. 14, no. 5, pp. 639-641, 2002.

[104] M. Abe, T. Kitagawa, K. Hattori, A. Himeno and Y. Ohmori, "Electro-optic Switch Constructed with a Poled Silica-Based Waveguide on a Si Substrate," *Electron. Lett.,* vol. 32, no. 10, p. 893, 1996.

[105] C. Xia and H. Sai-Ling, "An Electro-optic Modulator Based on GeO_2-doped Silica Ridge Waveguides with Thermal Poling," *Chinese Physics Lett.,* vol. 20, no. 7, p. 1081, 2003.

[106] S. Chao, H. Y. Chen, Y. H. Yang, Z. W. Wang, C. T. S. Shih and H. Niu, "Quasi-phase-matched Second-Harmonic Generation in Ge-Ion Implanted Fused Silica Channel Waveguide," *Optics Exp.,* vol. 13, no. 8, p. 7091, 2005.

[107] J. Fage-Pedersen, R. Jacobsen and M. Kristensen, "Planar Glass Devices for Efficient Periodic Poling," *Optics Exp.,* vol. 13, no. 21, p. 8514, 2005.

[108] J. Fage-Pedersen, R. Jacobsen and M. Kristensen, "Poled-glass Devices: Influence of Surfaces and Interfaces," *JOSA B,* vol. 24, no. 5, p. 1075, 2007.

[109] D. N. Nikogosyan, Nonlinear Optical Crystals: A Complete Survey, New York, NY: Springer, 2006.

[110] A. Rao, A. Patil, M. Malinowski, J. Chiles, S. Khan, A. Honardoost, S. Toroghi, G. F. Camacho-González, P. Rabiei and S. Fathpour, "Electro-optic and Second-Order Nonlinear Effects in Thin Film Lithium Niobate on Silicon," in *2017 IEEE Photonics Soc. Summer Summer Topical Meeting Series (SUM),* San Juan, Puerto Rico , 2017.

[111] P. Rabiei, J. Ma, J. Chiles, S. Khan and S. Fathpour, "Lithium Niobate Photonics on Silicon Substrates," in *IEEE Photonics Conference (IPC),* San Diego, CA, USA, 2014.

[112] P. Rabiei, J. Ma, J. Chiles, S. Khan and S. Fathpour, "Lithium Niobate Photonics on Silicon Substrates," in *IEEE Photonics Conference (IPC),* San Diego, CA, USA, 2014.

[113] R. A. Myers, N. Mukherjee and S. R. J. Brueck, "Large Second-order Nonlinearity in Poled Fused Silica," *Optics Letters,* vol. 16, no. 22, pp. 1732-1734, 1991.

[114] C. Corbari, L. C. Ajitdoss, I. C. S. Carvalho, O. Deparis, F. P. Mezzapesa, P. G. Kazansky and K. Sakaguchi, "The Problem of Achieving High Second-order Nonlinearities in Glasses: The Role of Electronic Conductivity in Poling of High Index Glasses," *Journal of Non-Crystalline Solids,* vol. 356, no. 50, pp. 2742-2749, 2010.

[115] L. R. Brennard, "Thermal Poling of Multioxide Silicate Glasses and Ion-Exchanged Waveguides," PhD dissertation, Optoelectronics Research Centre, University of Southampton, Southampton, 2002.

[116] P. Kazansky and P. S. J. Russel, "Thermally Poled Glass: Frozen-in Electric Field or Oriented Dipoles?," *Optics Communications,* vol. 110, no. 5-6, pp. 611-614, 1994.

[117] Schott Technical Glass Solutions GmbH, "Schott Borofloat 33," [Online]. Available: http://psec.uchicago.edu/glass/borofloat_33_e.pdf. [Accessed 9 June 2015].

[118] A. Lepicard, F. Bondu, M. Kang, L. Sisken, A. Yadav, F. Adamietz, V. Rodriguez, K. Richardson and M. Dussauze, "Long-lived Monolithic Micro-Optics for Multispectral GRIN Applications," *Scientific Reports,* vol. 8, no. 1, p. 7388, 2018.

[119] V. Rodriguez and C. Sourisseau, "General Maker-fringe Ellipsometric Analyses in Multilayer Nonlinear and Linear Anisotropic Optical Media," *JOSA B,* vol. 19, no. 11, p. 2650, 2002.

[120] J. C. Phillips, "Stretched Exponential Relaxation in Molecular and Electronic Glasses," *Rep. on Progress in Physics,* vol. 59, no. 9, p. 1133, 1996.

[121] Gamry Instruments, "Basics of Electrochemical Impedance Spectroscopy," Application Note, 2007.

[122] M. D. Ingram, J. E. Davidson, A. M. Coats, E. I. Kamitsos and J. A. Kapoutsis, "Origins of Anomalous Mixed-Alkali Effects in Ion-exchanged Glasses," *Glass Science and Technology,* vol. 73, no. 4, pp. 89-104, 2000.

[123] M. J. Duggan, T. Saito and T. Niwa, "Ionic Conductivity of Tantalum Oxide by RF Sputtering," *Solid State Ionics,* vol. 62, no. 1, pp. 15-20, 1993.

[124] G. Sethi, B. Bontempo, E. Furman, M. W. Horn, M. T. Lanagan, S. S. N. Bharadwaja and J. Li, "Impedance Analysis of Amorphous and Polycrystalline Tantalum Oxide Sputtered Films," *Journal of Materials Research,* vol. 26, no. 6, pp. 745-753, 2011.

[125] E. Barsoukov and J. R. Macdonald, Impedance Spectroscopy: Theory, Experiment, and Applications, Hoboken, NJ: John Wiley & Sons, 2018.

[126] MG Chemicals, "Silver Conductive Epoxy Adhesive Slow Cure / Extreme Conductivity 8330S Technical Data Sheet," 2016.

[127] M. Dussauze, T. Cremoux, F. Adamietz, V. Rodriguez, E. Fargin, G. Yang and T. Cardinal, "Thermal Poling of Optical Glasses: Mechanisms and Second-order Optical Properties," *Int. J. Appl. Glass Sci.,* vol. 3, no. 4, p. 309, 2012.

[128] Y. Quiquempois, N. Godbout and S. Lacroix, "Model of Charge Migration During Thermal Poling In Silica Glasses: Evidence of a Voltage Threshold for

the Onset of a Second-order Nonlinearity," *Physical Review A*, vol. 65, no. 4, p. 043816, 2002.

[129] M. Dussauze, E. I. Kamitsos, E. Fargin and V. Rodriguez, "Structural Rearrangements and Second-order Optical Response in the Space Charge Layer of Thermally Poled Sodium-Niobium Borophosphate Glasses," *The J. Physical Chemistry C*, vol. 111, no. 39, p. 14560, 2007.

[130] V. Macagno and J. W. Schultze, "The Growth And Properties of Thin Oxide Layers on Tantalum Electrodes," *J. Electroanalytical Chemistry and Interfacial Electrochemistry*, vol. 180, no. 1-2, p. 157, 1984.

[131] D. E. Carlson, "Ion Depletion of Glass at a Blocking Anode: I, Theory and Experimental Results for Alkali Silicate Glasses," *J. Amer. Ceramic Soc.*, vol. 57, no. 7, p. 291, 1974.

[132] D. E. Carlson, K. W. Hang and G. F. Stockdale, "Ion Depletion of Glass at a Blocking Anode: II, Properties of Ion-Depleted Glasses," *J. Amer. Ceramic Soc.*, vol. 57, no. 7, p. 295, 1974.

[133] M. Dussauze, V. Rodriguez, A. Lipovskii, M. Petrov, C. Smith, K. Richardson, T. Cardinal, E. Fargin and E. I. Kamitsos, "How does Thermal Poling Affect the Structure of Soda-lime Glass?," *The J. Physical Chemistry C*, vol. 114, no. 29, p. 12754, 2010.

[134] A. V. Redkov, V. G. Melehin and A. Lipovskii, "How does Thermal Poling Produce Interstitial Molecular Oxygen in Silicate Glasses?," *The J. Physical Chemistry C*, vol. 119, no. 30, p. 17298, 2015.

[135] A. Narazaki, K. Tanaka and K. Hirao, "Surface Structure and Second-order Nonlinear Optical Properties of Thermally Poled WO_3-TeO_2 Glasses Doped with Na+," *JOSA B*, vol. 19, no. 1, pp. 54-62, 2002.

[136] H. Zeghlache, M. Guignard, A. Kudlinski, Y. Quiquempois, G. Martinelli, V. Nazabal and F. Smektala, "Stabilization of the Second-order Susceptibility Induced in a Sulfide Chalcogenide Glass by Thermal Poling," *J. Appl. Physics*, vol. 101, no. 8, p. 084905, 2007.

[137] R. Petra, S. Z. Go, A. Tarazona, R. Cernansky, S. Reynolds, D. J. Thomson, A. Z. Khokhar, A. Politi, G. Z. Mashanovich, G. T. Reed and H. M. Chong, "HWCVD a-Si:H Interlayer Slope Waveguide Coupler for Multilayer Silicon Photonics Platform," in *2017 IEEE 14th International Conference on Group IV Photonics (GFP)*, Berlin, Germany, 2017.

[138] Y. Zhang, D. Kwong, X. Xu, A. Hosseini, S. Y. Yang, J. A. Rogers and R. T. Chen, "On-chip Intra- and Inter-layer Grating Couplers for Three-dimensional Integration of Silicon Photonics," *Appl. Phys. Lett.*, vol. 102, no. 21, p. 211109, 2013.

[139] J. F. Bauters, M. L. Davenport, M. J. Heck, J. K. Doylend, A. Chen, A. W. Fang and J. E. Bowers, "Silicon on Ultra-low-loss Waveguide Photonic Integration Platform," *Optics Exp.*, vol. 21, no. 1, pp. 544-555, 2013.

[140] M. Sodagar, R. Pourabolghasem, A. A. Eftekhar and A. Adibi, "High-efficiency and Wideband Interlayer Grating Couplers in Multilayer $Si/SiO_2/SiN$ Platform for 3D Integration of Optical Functionalities," *Optics Exp.*, vol. 22, no. 14, pp. 16767-16777, 2014.

[141] W. Sacher, Y. Huang, G. Q. Lo and J. K. Poon, “Multilayer Silicon Nitride-on-Silicon Integrated Photonic Platforms and Devices,” *J. Lightwave Techn.*, vol. 33, no. 4, pp. 901-910, 2015.

[142] G. Z. Masanovic, V. M. N. Passaro and G. T. Reed, “Coupling to Nanophotonic Waveguides using a Dual Grating-assisted Directional Coupler,” *IEEE Proc. Optoelectronics*, vol. 125, no. 1, pp. 41-48, 2005.

[143] D. Marcuse, “Directional Couplers made of Nonidentical Asymmetric Slabs. Part II: Grating-Assisted Couplers,” *J. Lightw. Technol.*, vol. 5, no. 2, pp. 268-273, 1987.

[144] R. M. Shubair and E. M. Alardi, “An Interactive Simulation Toolbox for Computer-Aided Learning of Wave Propagation in Dielectric and Optical Waveguides,” in *Symp. Antenna Technol. and Appl. Electromag.*, Winnipeg, Canada, 2000.

[145] Y. Fu, T. Ye, W. Tang and T. Chu, “Efficient Adiabatic Silicon-on-insulator Waveguide Taper,” *Photonics Research*, vol. 2, no. 3, pp. A41-A44, 2014.